Review article

A comprehensive review on recent progress in aluminum−air batteries

Yisi Liu [a,b], Qian Sun [a], Wenzhang Li [b], Keegan R. Adair [a], Jie Li [b,*], Xueliang Sun [a,*]

[a] *Department of Mechanical and Materials Engineering, University of Western Ontario, London, Ontario, N6A 5B9, Canada*
[b] *School of Chemistry and Chemical Engineering, Central South University, Changsha 410083, China*

Abstract

The aluminum−air battery is considered to be an attractive candidate as a power source for electric vehicles (EVs) because of its high theoretical energy density (8100 Wh kg^{-1}), which is significantly greater than that of the state-of-the-art lithium-ion batteries (LIBs). However, some technical and scientific problems preventing the large-scale development of Al−air batteries have not yet to be resolved. In this review, we present the fundamentals, challenges and the recent advances in Al−air battery technology from aluminum anode, air cathode and electro-catalysts to electrolytes and inhibitors. Firstly, the alloying of aluminum with transition metal elements is reviewed and shown to reduce the self-corrosion of Al and improve battery performance. Additionally for the cathode, extensive studies of electrocatalytic materials for oxygen reduction/evolution including Pt and Pt alloys, nonprecious metal catalysts, and carbonaceous materials at the air cathode are highlighted. Moreover, for the electrolyte, the application of aqueous and nonaqueous electrolytes in Al−air batteries are discussed. Meanwhile, the addition of inhibitors to the electrolyte to enhance electrochemical performance is also explored. Finally, the challenges and future research directions are proposed for the further development of Al−air batteries.

1. Introduction

Modern day society is currently in a transition phase from a fossil fuel based economy to the clean energy alternatives required to minimize environmental pollution. Therefore, several renewable energy sources are being explored such as solar, wind, and hydropower. It is also important to search for safe, reliable and efficient energy storage technologies with the capability to be used in large-scale applications. Among these devices, batteries are applied in portable electronic devices and electric vehicles (EVs) due to their relatively high energy density [1−3] and electronic efficiency. Furthermore, lithium-ion batteries (LIBs) have dominated the market due to their high gravimetric and volumetric capacity as well as good

energy efficiency [4]. The energy density of state-of-the-art LIBs is approximately 100~200 Wh kg^{-1}, which cannot fulfill the demand of high energy and power density EVs [5]. Tremendous research efforts have been devoted to the improvement of high energy LIBs [287,288], however, an alternative strategy is desired to develop novel energy storage and conversion systems with sufficient theoretical energy density required for future applications. Among these new energy storage systems, metal−air batteries have gained great interest due to their high energy density and capacity, low cost (depending on the metal anode), the negligible dependence of their capacity on operating load and temperature, and constant discharge voltage [6−11]. Up to now, several different types of metal−air batteries, such as lithium (Li)−air, sodium (Na)−air, potassium (K)−air, zinc (Zn)−air, magnesium (Mg)−air, and aluminum (Al)−air batteries have been extensively studied. Metal−air batteries exhibit high theoretical energy densities ranging between 2 ~ 10 folds higher than that of state-of-

the-art LIBs [12]. Table 1 summarizes the voltage, theoretical specific capacity and energy density of the typical metal—air batteries. Metal—air batteries are equipped with a metal anode and an air-breathing cathode through a suitable electrolyte. Due to the open battery configuration of metal—air batteries, the oxygen reagent can be directly received from the surrounding air instead of prior incorporation, thus contributing to their very high theoretical energy densities [9].

Among the metal—air batteries shown in Table 1, the Li—air battery shows the highest theoretical energy density (13000 Wh kg^{-1}), which is significantly greater than other rechargeable battery technologies [13,14]. Nonetheless, rechargeable Li—air batteries still have many challenges to overcome such as the blocking of porous carbon cathodes by discharge products, instability of lithium in humid environments [15], insufficient understanding of catalytic mechanism [16], low electrochemical efficiency owing to high charging overpotentials [17], and side product (such as lithium alkyl-carbonates and Li_2CO_3) formation during cycling [18]. These issues negatively affect the reversible charging and cycle life of Li—air batteries [19]. Additionally, nonaqueous electrolytes are generally used in Li—air batteries, which raise the cost and cause safety concerns related to the flammable organic solvents. For aqueous electrolyte metal—air batteries, there are also significant challenges. Aqueous Zn—air batteries suffer from the problems of zinc precipitation, zinc anode dendrite formation, non-uniform zinc dissolution, limited O_2 solubility in electrolytes, and higher charge overpotentials [20]. On the other hand, Mg—air and Al—air batteries are in their infancy and have gained much attention due to their many practical advantages, such as high energy density and theoretical voltage, safety, and abundance of raw materials. However, these battery chemistries are facing a series of problems such as the corrosion of Mg and Al metals, high self-discharge rate, sluggish discharge kinetics, lack of recharge-ability, and short shelf life [21]. Although it has been reported that some Al—air batteries with nonaqueous electrolytes, such as ionic liquid, can be rechargeable but may be prohibitively expensive [274]. Therefore, the critical research should be directed to overcoming the large amount of scientific and technical challenges for metal—air batteries before these promising energy storage devices are put into effect.

Among the previously discussed metal—air batteries, Al—air batteries hold great promise for future large-scale energy applications due to their lowest cost and high theoretical specific capacity of 2.98 Ah g^{-1}, which is the second highest only to that of lithium (3.86 Ah g^{-1}) and much higher than

those of magnesium (2.20 Ah g^{-1}) and zinc (0.82 Ah g^{-1}) [4,22,23]. Additionally, aluminum is an inexpensive, abundant and environmental friendly metal with high recyclability [24]. The Al—air battery has a high theoretical voltage (2.7 V) and energy density (8.1 kWh kg^{-1}), far surpassing that of state-of-the-art LIBs [24,25]. Fig. 1 schematically illustrates the basic structure of a primary Al—air battery, which is composed of an aluminum anode, air cathode, and a suitable electrolyte, typically consisting of sodium hydroxide (NaOH), potassium hydroxide (KOH) or sodium chloride (NaCl) solutions [26]. The electrochemical reactions at the electrodes can be signified as follows [23]:
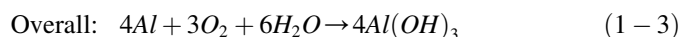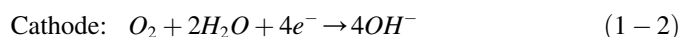
$$\text{Anode:} \quad Al \rightarrow Al^{3+} + 3e^- \qquad (1-1)$$

$$\text{Cathode:} \quad O_2 + 2H_2O + 4e^- \rightarrow 4OH^- \qquad (1-2)$$

$$\text{Overall:} \quad 4Al + 3O_2 + 6H_2O \rightarrow 4Al(OH)_3 \qquad (1-3)$$

Fig. 2 illustrates the history of Al—air batteries spanning over fifty years. The use of the aluminum metal anode was first proposed by Zaromb in 1962 [27,28] in an aluminum/oxygen system characterized by a high energy density system. In the following years, researchers had investigated a variety of applications for Al—air energy storage systems [29–37], such as power sources for electric vehicles (EVs) [A, C], military communications [B], unmanned underwater vehicle (UUVs) [E], and unmanned aerial vehicle (UAVs) [D, H]. Notably, in 2016, an Al—air battery weighing 100 kg was fabricated and shown to be capable of extending the range of an electric vehicle to over 3000 km. Many research groups have been dedicated to enhancing the capacity and lifetime of Al—air battery systems however there are still many hurdles to overcome.

Recently, Al—air batteries have attracted considerable attention and are under rapid development. In this review, we focus on the recent progress and technical issues with regard to Al—air battery components, including the anode, air

Table 1
Parameters of various metal—air batteries.

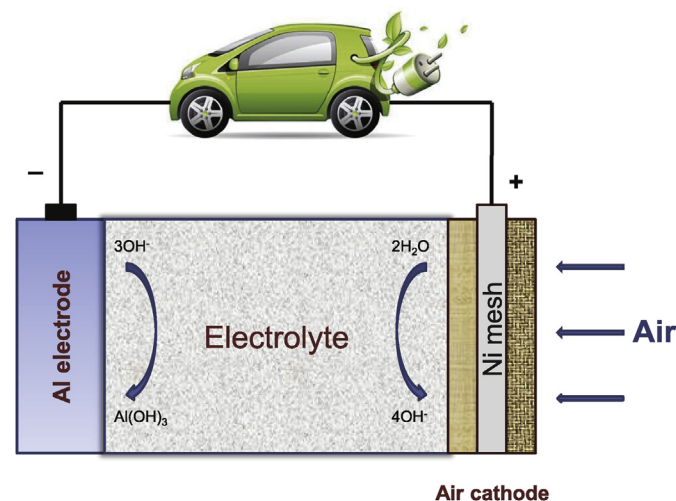| Batteries	Theoretical Voltage (V)	Theoretical specific capacity (Ah Kg^{-1})	Theoretical energy density (kWh kg^{-1})	Practical operating voltage (V)
Li—air	3.4	1170	13.0	2.4
Zn—air	1.6	658	1.3	1.0—1.2
Mg—air	3.1	920	6.8	1.2—1.4
Na—air	2.3	687	1.6	2.3
Al—air	2.7	1030	8.1	1.2—1.6

Fig. 1. Illustration of the structure of an Al—air battery using a 3-layer air electrode.
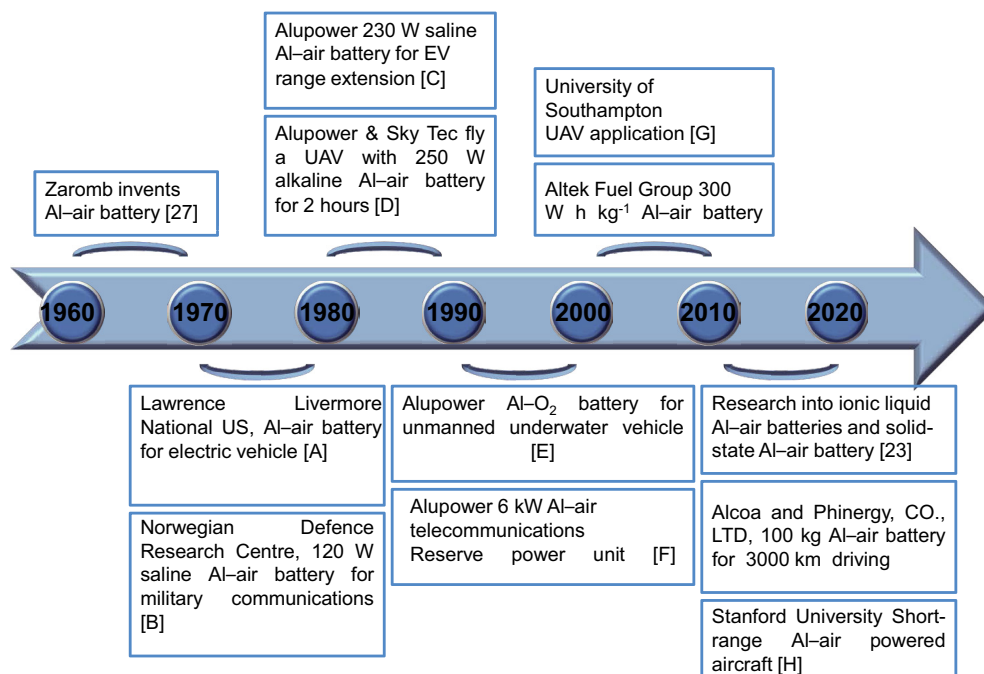
Fig. 2. Timeline of the development of Al−air batteries. EV is electric vehicle; UAV is unmanned aerial vehicle.

[A] J.F. Cooper, R.V. Homsey, J.H. Landrum, in: 15th Intersociety Energy Conversion Engineering Conference, vol. 2, 1980, p. 1487.

[B] T. Valand, O. Mollesad, G. Nilsson, in: Proceedings of the 12th International Power Sources Symposium, Power Sources, vol. 8, 1980, p. 523.

[C] C.D.S. Tuck, Modern Battery Technology, Ellis Horwood, 1991.

[D] K. Cameron, V. Kowalenko, Portable Unmanned Aircraft System Concept Investigation, Defence Science and Technology Organisation Aeronautical and Maritime Research Laboratory, Australia, 1995, DSTO-TR-0210.

[E] B.M.L. Rao, G.M. Scamans, in: Proc. 10th International Seminar on Primary and Secondary Battery Technology Applications, Deerfied Beach, Florida, 1993.

[F] G.M. Scamans, S.P. Lapp, S.M. Warner, D. Holmes, in: Telecommunications Energy Conference, INTELEC '92, 14th International, Washington, DC, USA, 1992, pp. 413−417.

[G] A.D. Kay, Novel Aluminium Air Batteries for Ultralight Micro−aircraft Master of Philosophy, University of Southampton, 2005.

[H] J. M. Vegh and J. J. Alonso, "Design and Optimization of Short-Range Aluminum−air Powered Aircraft", 54th AIAA Aerospace Sciences Meeting, AIAA SciTech Forum, Stanford University, 2016.
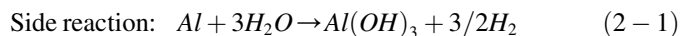
cathode and electrolyte, exploring each of these components strengths and challenges. We aim to provide readers with a fundamental understanding and update on this rapidly developing area.

2. Anode materials

2.1. Pure aluminum

Naturally, pure aluminum has been chosen as an anodic material for Al−air batteries in virtue of its excellent electrochemical properties. Thermodynamically, a pure aluminum anode exhibits a potential of −1.66 V (*vs.* Hg/HgO) in saline and −2.35 V (*vs.* Hg/HgO) in aqueous solution. However, the practical open-circuit potential of the aluminum electrode is significantly higher, which is attributed to the competitions between the considerable electrode processes that occur on the Al surface including [32,33]: (i) the formation and/or dissolution of an initial Al_2O_3 and subsequent $Al(OH)_3$ layer, (ii) a three-electron charge transfer process producing Al^{3+} species, (iii) the formation of corrosion products, $Al(OH)_4^-$ and $Al(OH)_3$, and (iv) a parasitic corrosion reaction on the aluminum surface releases hydrogen [34]. The parasitic

chemical reaction (iv) that takes place between aluminum and water on the anode may be described as:

Side reaction: $\quad Al + 3H_2O \rightarrow Al(OH)_3 + 3/2H_2 \qquad (2-1)$

This side reaction causes corrosion and passivation of the aluminum surface, ultimately leading to the failure of Al−air batteries. A major problem with Al−air batteries is the thermodynamically favorable protective oxide film that forms spontaneously on the aluminum surface when exposed to air and aqueous solutions. This surface passivation leads to a positive shift of the corrosion potential of the aluminum electrode and a considerable slow-down of aluminum activation [35,36].

The self-corrosion is detrimental to the capacity of Al−air batteries and can reduce the discharge efficiency. Thus, many studies have focused on reducing the rates of corrosion and hydrogen evolution. Recently, the battery performance of 2N5 commercial grade Al with 99.5% purity has been studied in 4 M NaOH electrolyte [37]. The performance of 2N5 Al in Al−air battery was found to be inferior to that of 4 N high pure (99.99%) Al due to the complex impurity layer reducing the average discharge voltage [37]. Lu et al. [38] investigated the electrochemical properties and battery performance of

polycrystalline Al, Al (001), (110) and (111) single crystals. The study revealed that Al (001) single crystals displayed lower corrosion rate and higher capacity density due to the low surface energy. However, high rate of corrosion and parasitic hydrogen evolution on the surface of the pure aluminum make it infeasible for application of Al–air batteries as energy sources.

2.2. Aluminum alloys

As pure aluminum is unstable when used as an anode for Al–air batteries, the most common method to prolonging the battery operation time and decreasing the corrosion rate is through the use of Al alloys. A considerable number of alloying elements such as Ga, Tl, In, Sn, Zn, Bi, Mn and Mg have been adopted. The outstanding performance of Al alloys in Al–air batteries can be attributed to the comprehensive effect of each individual alloying component. At present, the most commonly used anode materials in Al–air batteries are Al–Zn, Al–In, Al–Ga and Al–Sn [39–46] alloys. Zinc (Zn) is well known to diminish hydrogen evolution on Al anodes by enhancing the HER potential and thus relieving the anode degradation [47]. Indium (In) is responsible for a positive shift of the anode potential and an increase of the hydrogen evolution overpotential [48]. In addition, gallium (Ga) has been proven to limit the oxide film passivation in chloride solutions by activating the surface sites of aluminum [49]. Furthermore, tin (Sn) can increase the dissolution rate of Al in aqueous solutions and reduce the corrosion rate [49]. The corrosion behavior and performance of Al–0.5Mg–0.1Sn–0.02In–0.1Si and Al–0.5Mg–0.1Sn–0.02Ga–0.1Si alloys in Al–air batteries were investigated in 2 M NaCl and 4 M NaOH [50]. The results indicate that the Al–0.5Mg–0.1Sn–0.02Ga–0.1Si alloy exhibits a better electrochemical performance in the 2 M NaCl solution, while the Al–0.5Mg–0.1Sn–0.02In–0.1Si alloy shows a better electrochemical performance in the 4 M NaOH solution, which is due to the addition of Ga which can reduce the self-corrosion rate of Al–0.5Mg–0.1Sn–0.02Ga–0.1Si alloy in the NaCl solution and the addition of In can remove the passive film on the Al–0.5Mg–0.1Sn–0.02In–0.1Si alloy by the alkali. The addition of Si as an alloying component to Al–0.5Mg–0.1Sn decreases the self-corrosion rate and increases the anode utilization [50]. Boughrara et al. [51] studied the corrosion behavior of Al, Al–Zn and Al–Zn–Sn in 3 wt.% NaCl solution. The improved activity of Al–Zn and Al–Zn–Sn can be attributed to an inductive behavior of the intermediates leading to intergranular corrosion. Furthermore, the corrosion rate and discharge activity of Mg–6%Al–3%Zn and Mg–6%Al–3%Zn–(1%, 1.5%, 2%)In alloys were also investigated [52]. The Mg–6%Al–3%Zn–1.5%In alloy exhibits the highest corrosion rate but undesirable discharge activity, and the Mg–6%Al–3%Zn–1.0%In alloy has a relatively low corrosion rate but the highest discharge activity, indicating the barrier effect caused by the β-$Mg_{17}Al_{12}$ phase can be influenced under the conditions of anodic polarization. The results demonstrated that the Mg–6%Al–3%Zn–1.0%In alloy would be a promising anode material for both cath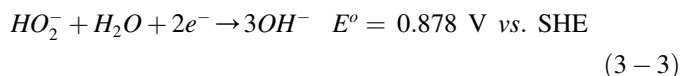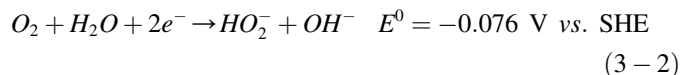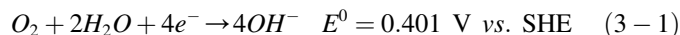odic protection and power source applications. In addition, the performance of Al–air batteries using pure Al and Al-0.5 wt.%In as anodes in 4 M NaOH solution was studied [48]. The Al–In alloy exhibited a lower self-corrosion rate and higher anodic efficiency than pure Al. These types of sacrificial anodes based on aluminum alloys are preferred in Al–air batteries due to the alloying elements ability to remove the passivating layer on the aluminum surface.

3. The air cathode

The air cathode is one of the essential components of an Al–air battery, which is generally composed of a gas diffusion layer, current collector, and catalytic active layer. The gas diffusion layer is composed of a carbon material and a hydrophobic binder such as polytetrafluoroethylene (PTFE), making the diffusion layer permeable only to air and preventing the permeation of water [53]. Current collectors are typically made of a Ni metal mesh which can be connected to the external circuit and enhance the electron transfer processes [54]. The catalytic active layer consists of an electrocatalyst, carbon material, and binder, and is the location where the oxygen reduction reaction (ORR) takes place [55]. With regards to the air electrode, the sluggish efficiency of the oxygen reduction reaction is the critical barrier for the application of workable Al–air batteries. Additionally, there are other problems leading to the inefficiency of the air electrode. Table 2 exhibits the related problems of air electrodes and the solutions to each aspect. More discussions will be presented in the following parts of this review.

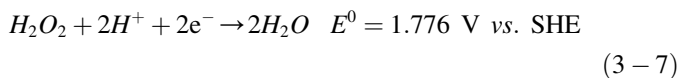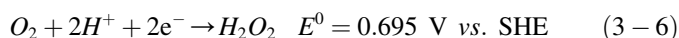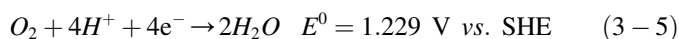### 3.1. Oxygen reduction reaction at the cathode

The oxygen reduction reaction (ORR) is the central cathodic reaction in the Al–air system. Generally, there are two typical pathways for the reduction of molecular oxygen in alkaline medium: the direct four-electron pathway and the successive two-electron pathway [62]. A direct four-electron pathway (equations (3-1)) is the preferred route. Alternatively the successive two-electron pathway first involves the production of peroxide HO_2^- and subsequently experiences a two-electron reduction of peroxide HO_2^- to OH^- or disproportionation expressed by equations (3-2), (3-3) and (3-4). If reactions (3-2) and (3-3) are extremely rapid, the ORR occurs directly through the four-electron transfer pathway.

$$O_2 + 2H_2O + 4e^- \rightarrow 4OH^- \quad E^0 = 0.401 \text{ V } vs. \text{ SHE} \quad (3-1)$$

$$O_2 + H_2O + 2e^- \rightarrow HO_2^- + OH^- \quad E^0 = -0.076 \text{ V } vs. \text{ SHE} \quad (3-2)$$

$$HO_2^- + H_2O + 2e^- \rightarrow 3OH^- \quad E^o = 0.878 \text{ V } vs. \text{ SHE} \quad (3-3)$$

$$2HO_2^- \rightarrow 2OH^- + O_2 \quad (3-4)$$

In acidic solution, the four-electron (Equation 3-5) and two-electron (Equation 3-6, 3-7, and 3-8) pathways are:

Table 2
Overview of air electrode related problems and solutions.

Related problems	Cause	Effect	Proposed solutions
Sluggish oxygen reactions	High overpotential required for driving oxygen reduction reaction (ORR) and oxygen evolution reaction (OER) [54]	Limited energy/power density and energy efficiency	Explore efficient, durable electrocatalysts [21,55−57]
Air electrode flooding	Electrolyte penetration into the pores of the air cathode	Reduced oxygen accessibility	Treat carbon electrode with wax [58]; Proper optimization of the gas diffusion layer (GDL) [59]
Carbonate precipitation	Atmospheric CO_2 reacts with alkaline electrolyte, producing carbonate precipitates [60]	Decreased electrolyte conductivity and air cathode activity	Supply pure O_2 to reduce CO_2 concentration [61]
Electrolyte drying out	Water evaporation to open air	Reduced battery life	Proper optimization of the gas diffusion layer (GDL) [59]

$$O_2 + 4H^+ + 4e^- \rightarrow 2H_2O \quad E^0 = 1.229 \text{ V } vs. \text{ SHE} \quad (3-5)$$

$$O_2 + 2H^+ + 2e^- \rightarrow H_2O_2 \quad E^0 = 0.695 \text{ V } vs. \text{ SHE} \quad (3-6)$$

$$H_2O_2 + 2H^+ + 2e^- \rightarrow 2H_2O \quad E^0 = 1.776 \text{ V } vs. \text{ SHE} \quad (3-7)$$

$$2H_2O_2 \rightarrow 2H_2O + O_2 \quad (3-8)$$

3.2. Catalysts

The electrocatalyst in the air electrode plays an important role in determining the electrode performance and maximization of energy density. However, the reaction kinetics of the ORR is often sluggish, and occurs with a large overpotential [63]. Thus, one of the key opportunities to improving the ORR efficiency and reduce the overpotential is to explore suitable electrocatalysts. A diverse selection of electrocatalytic materials have been utilized as cathode catalysts, including precious metals and alloys, transition metal oxides/chalcogenides, metal macrocyclic compounds and carbonaceous materials [64]. In spite of the previous general reviews on the ORR electrocatalysts [65−74], the following part of this review will focus on the lately reported progresses of electrocatalysts related to Al−air batteries.

3.2.1. Noble metals and alloys (Pt-based catalysts)

The most commonly used noble metal catalysts include platinum (Pt), palladium (Pd), gold (Au) and silver (Ag) [22]. The unoccupied *d*-orbital of these noble metals are in a vacant state, allowing them to easily adsorb reactant molecules and act as a catalytic centre. The catalytic activity of noble metals is greatly influenced by their surface atomic configuration and electron level state. Thus, the most common method of improving the performance of noble metal catalysts is to engineer their atomic configuration. Pt has been intensively studied for several decades and has kept sustainable interest because of its superior electrocatalytic activity. A large amount of studies indicated that the catalytic activity is not only affected by the particle size, but also by the indices of crystallographic facets [75]. The order in ORR catalytic activity of different crystallographic facets is: Pt{100} < Pt{110} < Pt{111} [76,77], which is determined by the binding strength between platinum atoms and absorbed species. In addition, many efforts have been made to prove that controlling the facet distribution can regulate the morphology of Pt nanocrystals [78,79]. There was an intrinsic triangle that coordinated the crystal surface index and the shape of metal nanocrystals (NCs) (Fig. 3) [80]. Three vertices represent the coordinates of polyhedral nanocrystals bounded by basal facets, *i.e.* cube covered by {100}, octahedron by {111}, and rhombic dodecahedron by {110}. It was determined that the sharp end of the Pt nanorods was enclosed by ten {410} facets, the obtuse end by {320}, {210} or {730} facets, and the middle part mainly by the zigzag-arranged {520} facets. In addition, the nanocrystals bounded by high-index facets display high catalytic activity and stability [80]. Sun and coworkers [81] found that the ORR catalytic activity was determined by the adsorption rates of sulfates on Pt{100} and Pt{111} facets in a H_2SO_4 medium, indicating controlling nanocrystal shapes can reduce the binding strength between Pt atoms and the adsorbed species.

However, limited resources and the high cost of Pt make it necessary to reduce the Pt loading of Pt-based catalysts. High-surface-area catalytic support materials (e.g., carbon) with platinum nanoparticles are the state-of-the-art ORR electrocatalysts [82]. The most feasible strategy in Pt utilization is to not only optimize the catalytic performance but also lower the cost by alloying Pt with other appropriate precious or transition metals. Surprisingly, the catalytic activity of Pt-metal alloys (PtM) is much higher than that of Pt-only nanoparticles, which can be ascribed to the compressive strain and electronic ligand effects [83]. Small-size transition metal atoms are incorporated into the Pt lattice structure, resulting in a decreased Pt lattice parameter. In addition, Pt *d*-orbital filling is changed by the charge transfer from the transition metal to Pt due to the difference between their electronegativities in PtM alloy systems [83]. The intrinsic electrocatalytic activity of PtM alloys depends on their composition, particle size, and
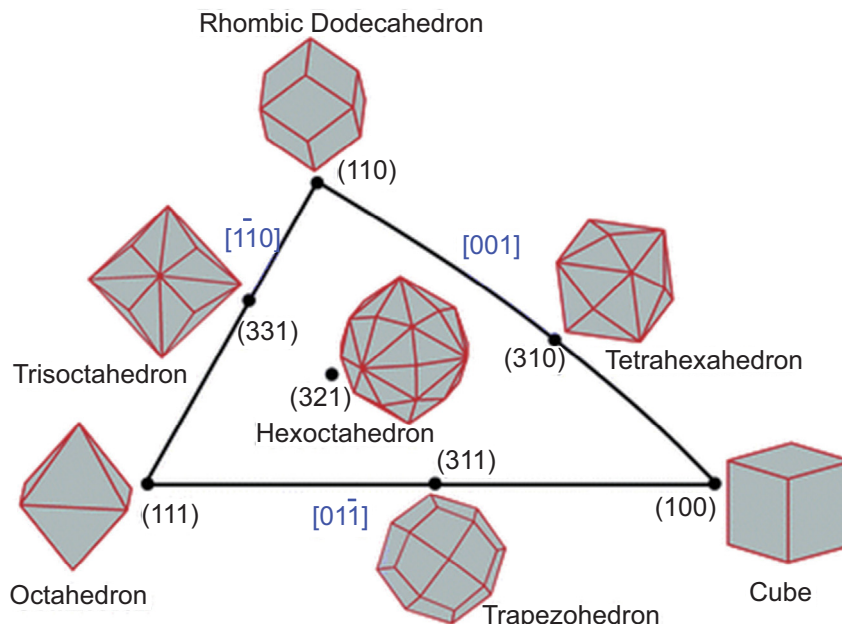
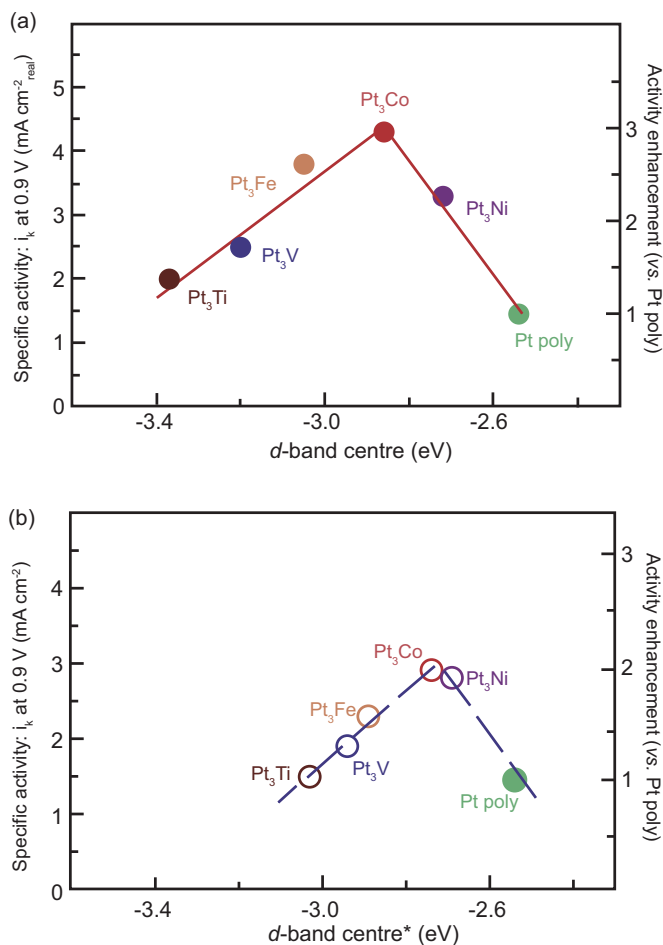Fig. 3. The relation between shape and planes of polyhedral nanocrystals [80].

Fig. 4. **Relationships between the catalytic properties and electronic structure of Pt$_3$M alloys.** Relationships between experimentally measured specific activity for the ORR on Pt$_3$M surfaces in 0.1 M HClO$_4$ at 333 K versus the d-band centre position for the Pt-skin (a) and Pt-skeleton (b) surfaces. (b) shows the d-band centre values* established in UHV, which may deviate in the electrochemical environment due to dissolution of non-Pt atoms [85].

structure [84]. Thus, there has been a focus on using composition, size, and structure-controlled alloy nanocrystals to optimize their ORR catalytic activity. The relationship between the surface electronic structure (the d-band centre) and electrocatalytic trends for ORR of Pt$_3$M (M = Ni, Co, Fe, Ti, V) surfaces has previously been established [85] (Fig. 4). The electrocatalytic trends can be explained by a balance between adsorption energies of reactive intermediates and surface coverage by spectator (blocking) species, providing a fundamental basis for the catalytic enhancement of cathode catalysts. Xia's group [86] reported a comprehensive study on ORR activities of nanosized Pt−Ni octahedral catalysts with a series of controlled sizes and compositions (Fig. 5). The 9 nm Pt−Ni octahedral shows the highest specific activity for the ORR, and exhibits a volcano type plot with different Pt/Ni atomic ratios. The results of the study provide useful guidance for the design of superior nanosized Pt−Ni electrocatalysts. Yang's group reported Pt alloy (PtM, M = Co, Fe, Ni, Pd) nanocrystals with cubic and octahedral morphologies synthesized using CO as the reducing agent [87]. Octahedral Pt$_3$Ni nanoparticles have better ORR activity compared to cubic Pt$_3$Ni nanoparticles, indicating that the catalytic performance can be controlled by both shape and composition [87]. The Pt-M (M = Au, Ni, Pd) icosahedral nanocrystals were synthesized based on the gas reducing agent in liquid solution (GRAILS) method. The specific activity of icosahedral Pt$_3$Ni catalysts is about 50% higher than that of the octahedral Pt$_3$Ni catalysts, even though their shapes are stabilized by {111} facets [88]. Greeley et al. investigated a set of ORR electrocatalysts consisting of Pd or Pt alloyed with early transition metals. The experimental and DFT calculations demonstrated the volcano relationship of a set of PtM electrocatalysts (Fig. 6a) [89]. The results indicate that the activity of polycrystalline Pt$_3$Sc and Pt$_3$Y alloys is improved compared with
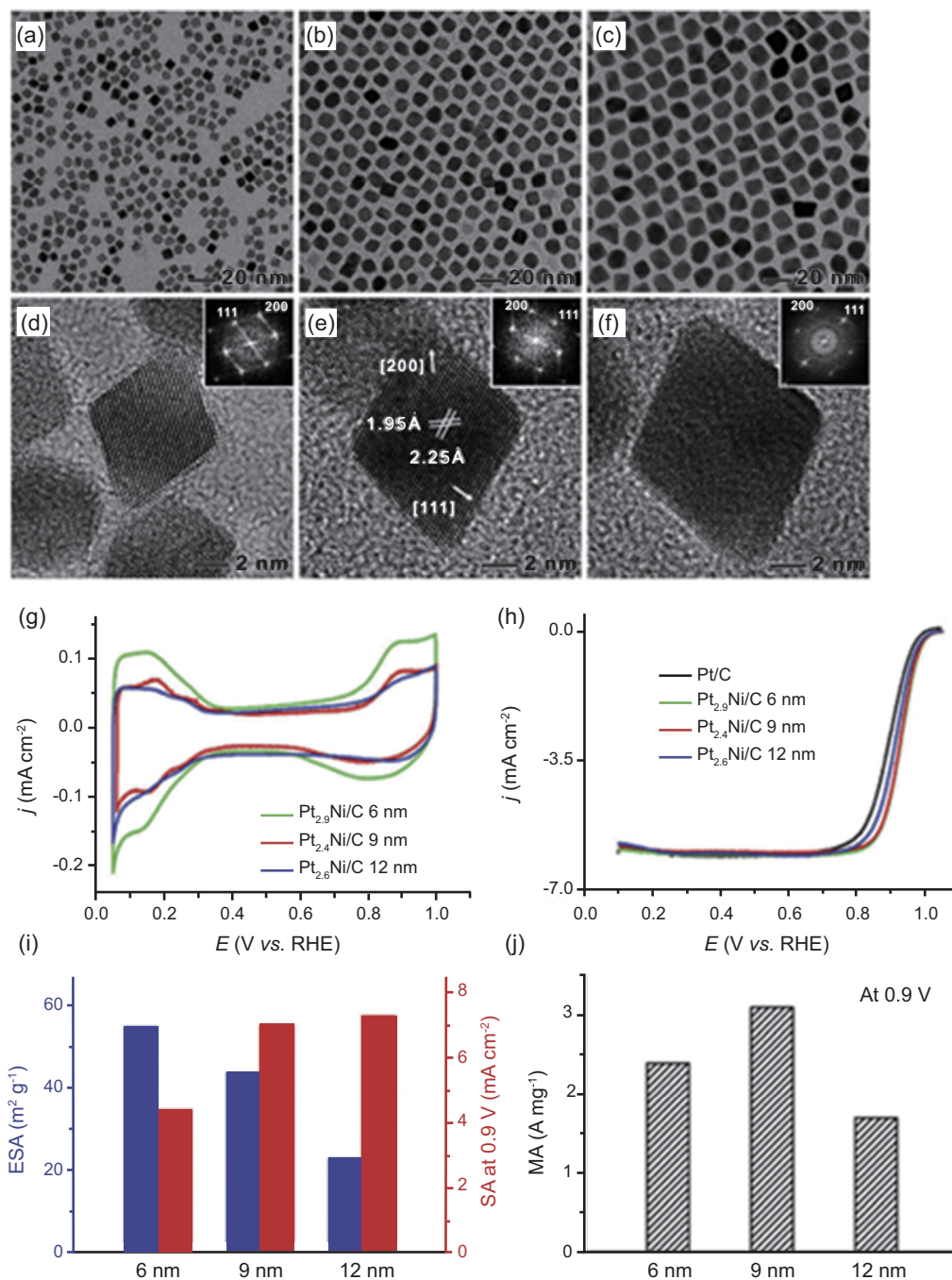
Fig. 5. (a—c) TEM and (d—f) HRTEM images of Pt—Ni octahedra with three different edge lengths: (a, d) 6, (b, e) 9, and (c, f) 12 nm. The Pt/Ni atomic ratio, obtained after treatment with HAc for 30 min, was around 2.4. The insets in (d—f) show the corresponding FT patterns derived from the fringes of individual Pt—Ni octahedra. (g) CVs of the octahedral Pt—Ni/C catalysts with different sizes (after treatment with HAc for 30 min) in N_2-saturated 0.1 M $HClO_4$ solutions. Scanning rate = 100 mV s^{-1}. (h) Comparison of positive-going ORR polarization curves of the octahedral Pt—Ni/C catalysts and commercial Pt/C in O_2-saturated 0.1 M $HClO_4$ solutions. (i) Comparison of ESAs and specific activities of Pt—Ni/C catalysts with edge lengths of 6, 9, and 12 nm. (j) Comparison of Pt mass activity of the corresponding Pt—Ni/C catalysts at 0.9 V [86].

pure Pt by a ~60 mV positive shift of half-wave potential and a 6~10 higher kinetic current density (Fig. 6b) [89].

In spite of their great initial activity, PtM alloys show poor durability in long term ORR processes. Owing to the dissolution and oxidation of the transition metal components M in acidic environments, the ORR catalytic activity is significantly reduced. Therefore, a novel core-shell structural catalyst was introduced to prevent the dissolution of transition metals from the catalyst surface [90—92]. The core-shell alloy design greatly reduces the amount of Pt catalyst, and efficiently promotes the occurrence of electrocatalytic reactions due to more Pt concentrating on the surface shell layer. Recently,
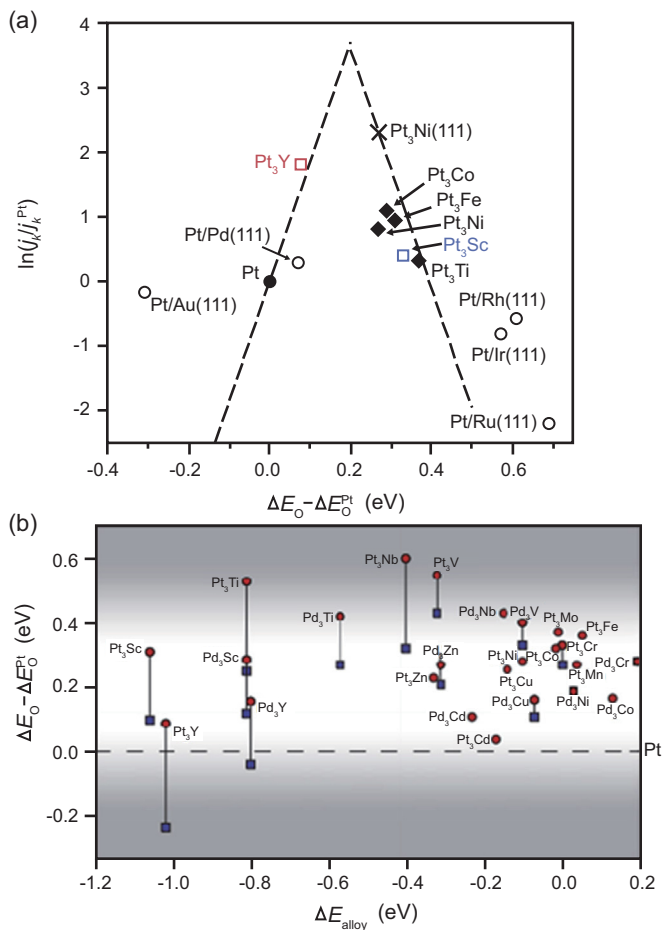
(a)

(b)

Fig. 6. Pt-alloys for electrocatalysis of the ORR: (a) Volcano plots of the oxygen reduction kinetic current density (j_k) as a function of the calculated oxygen adsorption energy (DE_O); (b) Computational results showing the relationship between the oxygen binding energy on Pt/Pd skin surfaces and alloying energy. Data are shown relative to Pt while circles and squares in (b) represent 50 and 25% of the alloying element in the second layer [89].

attempts have been made to fabricate novel Pt-based core-shell nanomaterials as highly efficient catalysts [93−95] to maximize the exposed catalytical active sites. The core-shell structure is designed to bring catalysts both high activity and stability for metal−air systems by tuning the electronic structure and lattice parameters of Pt shell layers.

For Pt-based alloy systems, it is necessary to develop novel synthetic approaches for PtM nanocatalysts with controllable composition, shape, and size. Despite extensive research in exploring non-Pt electrocatalysts due to the high cost of Pt, Pt-based electrocatalysts are still the most promising nanomaterials with superior catalytic performance in metal−air batteries.

3.2.2. Nonprecious metal catalysts

Although Pt has been regarded as the best ORR catalyst, the commercial market of Al−air batteries may still be hampered by the limited resources, high cost and unsatisfactory durability of the conventional Pt-based catalysts. Thus, searching for available alternatives to substitute Pt by efficient nonprecious metal catalysts has obtained intensive interest. Non-precious catalysts such as transition metal oxides [96,97], spinel-type metal oxides [98,99], perovskite [100,101], metal−N complexes on carbon matrixes [63,102], and carbonaceous materials for ORR catalysis in metal−air batteries are discussed in the following sections.

3.2.2.1. Transition metal oxides.
Transition metal oxides have prominent advantages such as high abundance, low cost, and environmental friendliness. Early transition metals elements (e.g., Mn, Fe, Co and Ni) located in VII and VIII group have multiple valences, resulting in a variety of oxides. For instance, manganese can exist in different valence states of Mn(II), Mn(III) and Mn(IV), corresponding to abundant and ubiquitous manganese oxides including MnO, Mn_3O_4, Mn_5O_8, Mn_2O_3,
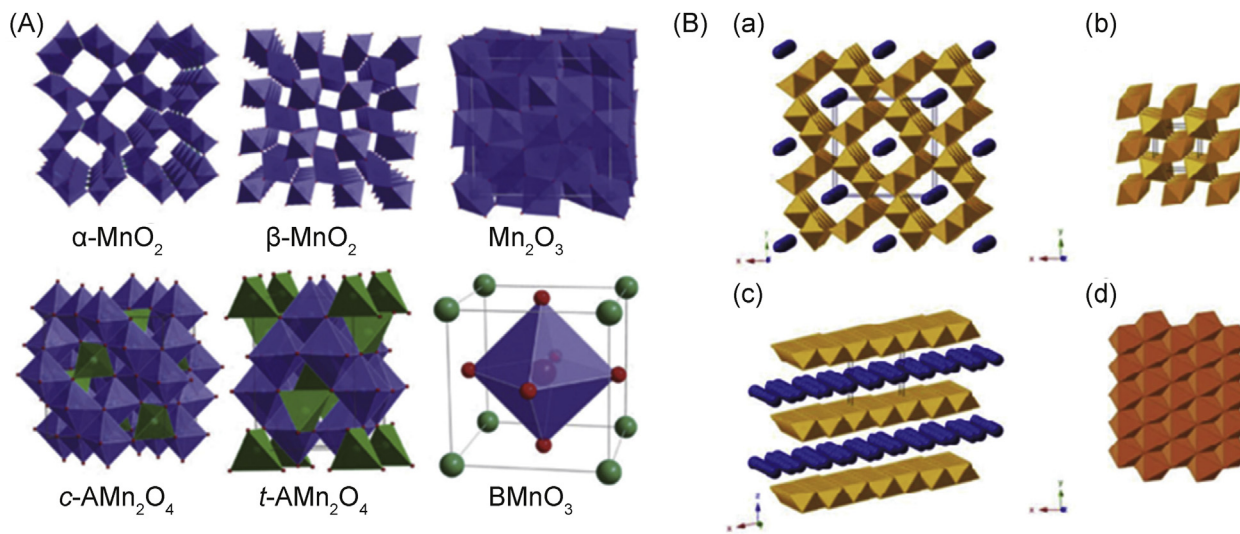

Fig. 7. (A) Presentations of the structures of some binary and ternary manganese oxides. *c*- and *t*-AMn$_2$O$_4$ denote cubic and tetragonal Mn-based spinels, respectively, with the A-site cations being tetragonally coordinated with oxygen. BMnO$_3$ represents the Mn-based perovskite with the B-site ions being marked in green. Metal cations in A, B and Mn sites can be substituted by other metal ions [113]. (B) Structures of manganese oxide reported here in this study (a) α-MnO$_2$ (2 × 2 tunnel), (b) β-MnO$_2$ (1 × 1 tunnel, pyrolusite), (c) δ-MnO$_2$ (layered, birnessite) and (d) amorphous manganese oxides (AMO) [114].

MnOOH and MnO_2 [103]. These manganese oxides have been proven to possess electrocatalytic activities towards ORR in alkaline condition [57,104–110]. One possible explanation is that the Mn–O–O complex clusters are the catalytically active centres of oxygen evolution in photosystem II in nature [111–113]. Even with the same elemental composition and valence state, manganese oxides may be characterized by different crystallographic structures (Fig. 7). The variable valences and abundant structures of transition metal oxides provide a large amount of opportunities for the development of nonprecious metal catalysts. For example, the catalytic activities of MnO_2 with different structure are demonstrated as α-MnO_2 > δ-MnO_2 > γ-MnO_2 > λ-MnO_2 > β-MnO_2, which can be attributed to an integrated effect of their intrinsic tunnel size and electrical conductivity [114]. MnO_2 with different morphologies such as MnO_2 hollow spheres [115], MnO_2 nanoflakes [116], MnO_2 nanorods [117], MnO_2 nanowires [118], etc. have been demonstrated to be available catalysts for ORR, which is attributed to the polymorphism and the highly exposed Mn^{3+} on the surface [119].

There are many studies on other transition metal oxide catalysts for ORR, such as cobalt oxides [120,121], nickel oxides [122], iron oxides [123], copper oxides [124], titanium oxides [125], cerium oxides [126,127], etc. Among these oxides, Co_3O_4 is considered to be a promising electroactive material owing to its low cost, environmentally friendliness, and high catalytic activity [121]. Many efforts have been devoted to control the Co_3O_4 structures with various morphologies [121,128–130]. Xiao and Yang et al. [131] investigated the effects of surface structures on ORR activity. The (110)-, (100)-, and (111)-exposed Co_3O_4 nanorods, nanocubes, and nano-octahedrons uniformly supported on graphene sheets were controlled synthesized. The catalytic activity was found to be dependent upon the surface structure of Co_3O_4 nanocrystals, increasing in the order of (111) > (100) > (110), and revealing that surface Co^{2+} ions have a strong influence on the ORR activity [132]. However, due to the low electrical conductivity of transition metal oxides, nanostructured carbon has often been used as a support to enhance the conductivity and catalytic performance. Zhu et al. [133] developed a novel Co_3O_4 nanosheets/graphene composite that was used as an ORR electrocatalyst exhibiting superior activity and stability to the state-of-the-art commercial Pt/C catalysts in alkaline medium. It is demonstrated that other nonprecious metal electrocatalysts, including Co_3O_4 nanoparticle/nitrogen-doped graphene and Co_3O_4 nanoparticle/carbon nanotube composites exhibit high catalytic activity. Density functional theory (DFT) calculations reveal that the superior stability of Co_3O_4 nanosheets-graphene composite can be ascribed to the strong interaction between the Co_3O_4 nanosheets and graphene. Besides Co_3O_4/nanocarbon hybrids, metallic Co has been incorporated together with Co_3O_4 and nanocarbon to improve the electrical conductivity of Co_3O_4. For instance, the Co/Co_3O_4/N/C composite [134], and core-shell Co@Co_3O_4/bamboo-like N-doped CNTs (BNCNTs) [135] have been prepared and studied. The ORR performances of various transition metal oxide/nanocarbon hybrids are listed in Table 3. It is rather difficult to understand the mechanisms of ORR and the intrinsic properties of transition metal oxides that regulate the catalytic activity due to the complex valence redox and variable crystallographic structures.

3.2.2.2. Spinel oxides. Spinel (AB_2O_4) is a cubic close-packed lattice arranged with oxide anions, where 1/8 of the tetrahedral sites are occupied by A atoms, and 1/2 of the octahedral sites are occupied by B atoms [137]. Spinel oxides are particularly popular as cathode electrocatalysts because of their multiple valence state, environmentally friendly, low cost, and high electrocatalytic activity. Cheng et al. [98] reported that the spinel $CoMn_2O_4$ nanocrystal can be used as an efficient bifunctional electrocatalyst for both ORR and OER under alkaline condition. In another paper, a Co_3O_4–$CoMn_2O_4$ nanocomposite was synthesized as a bifunctional electrocatalyst exhibited synergistic catalytic activity for ORR and OER [136]. Despite their good catalytic activity for ORR, the low electrical conductivity of spinel oxides is still a primary concern in utilizing them as electrocatalysts. To overcome this obstacle, nanocarbon supports such as active carbon, carbon nanotubes, graphene, etc. have been developed. In 2011, Dai's group [137] reported that Co_3O_4 nanoparticles dispersed on N-doped reduced mildly

Table 3
ORR performances of transition metal oxide/nanocarbon catalysts.

Catalysts	E_{onset} *vs.* RHE	$E_{1/2}$ *vs.* RHE	Tafel slope (mV dec^{-1})	Durability	Ref
Co_3O_4/N-rmGO	0.93	0.82	−42		[137]
Co_3O_4/N/C	0.92	0.79		92% retention of *j* under 0.47 V for 10 h	[139]
Co@Co_3O_4/NCNT	0.92	0.76	−83	78% retention of *j* under 0.47 V for 5.6 h	[157]
Mn_3O_4/NrGO	1.05	0.71		10 mV penalty of $E_{1/2}$ after 3000 cycles from 1.21 to 0.21 V	[158]
Mn_3O_4/N/C	0.91	Undefined		94% retention of *j* under 0.57 V for 4.2 h	[159]
MnO/3D-NrGO	0.83	Undefined		64.9% retention of *j* under 0.47 V for 5.6 h	[160]
Fe_3O_4/NrGO	0.86	Undefined			[161]
Fe_3O_4/N/C	0.92	0.76		90% retention of *j* under 0.56 V for 2.8 h	[150]
CoO@MnO_2/rGO	Undefined	0.76		87% retention of *j* under 0.66 V for 5 h	[162]
MnO_x-CeO_2/KB	0.94	0.81	94.4	80% retention of *j* under 0.70 V for 2.8 h	[163]
Porous Mn_2O_3	1.00	Undefined		80% retention of *j* under 0.70 V for 10 h	[294]
C_{PANI}/Mn_2O_3	0.97	0.78	73	91.1% retention of *j* under 0.80 V for 22.2 h	[295]

Table 4
ORR performances of spinel oxide/nanocarbon catalysts.

Catalysts	E_{onset} *vs*. RHE	$E_{1/2}$ *vs*. RHE	Tafel slope (mV dec^{-1})	Durability	Ref
$MnCo_2O_4$/N-rmGO	0.93	0.85		96% retention of *j* under 0.70 V for 5.6 h	[164]
$CoMn_2O_4$/C	0.90	0.67		96% retention of *j* under 0.46 V for 3.3 h	[154]
$MnCo_2O_4$/CNT	1.03	0.70		87% retention of *j* under 0.66 V for 90 h	[165]
$NiCo_2O_4$/rGO	0.87	Undefined			[145]
$NiCo_2O_4$/NrGO	0.88	0.64		87% retention of *j* under 0.71 V for 2 h	[144]
$CuCo_2O_4$/NrGO	0.89	0.78		85% retention of *j* under 0.71 V for 5.6 h	[146]
$CoMn_2O_4$/NGA	1.07	0.76		20 mV penalty of $E_{1/2}$ after 1000 cycles from 1.21 to 0.21 V	[166]
$CoFe_2O_4$/rGO	0.84	Undefined	67.0	91.3% retention of *j* under 0.80 V for 12 h	[147]
Co_3O_4/Co–N–C	Undefined	0.80	68.5	4.7% current decrease after 2000 cycles.	[289]
Co_3O_4/N-KB	Undefined	0.79	74.7		[290]
$NiCo_2O_4$/graphene foam		0.86	51	90% retention of *j* under 0.75 V for over 7000 s	[291]
$Ni_xCo_{1-x}Fe_2O_4$	0.81	0.61			[292]
Co_3O_4–$MnCo_2O_4$/NrGO	0.93	0.79	80.2	86.3% retention of *j* under 0.66 V for 8 h	[293]

oxidized graphene oxide (N-rmGO) exhibited superior catalytic activity for oxygen reduction and oxygen evolution in alkaline media to that of the commercial Pt/C catalyst. Afterwards, comprehensive studies about spinel/nanocarbon hybrids have been carried out, in which the spinel oxides include Co_3O_4 [138–140], $MnCo_2O_4$ [141,142], $NiCo_2O_4$ [143–145], $CuCo_2O_4$ [146], $CoFe_2O_4$ [147,148], Fe_3O_4 [149,150], $CoMn_2O_4$ [151,152], $ZnCo_2O_4$ [153], and various heterogeneous nanostructures based on these spinel oxides [154–156]. The ORR performances of various spinel/nanocarbon hybrids are listed in Table 4.

3.2.2.3. Perovskite oxides. Interestingly, perovskite oxides (ABO_3, where A is a rare earth and B is a transition metal) exhibit bifunctional electrocatalytic activity for both the ORR and OER. The work on perovskite oxides for ORR started in the 1970s, in which Matsumoto et al. investigated $LaNiO_3$ for electrocatalysis of oxygen reduction [21,167]. Recent studies have demonstrated that the ORR electrocatalytic activity of perovskite correlates primarily to σ*-orbital (e_g) occupation and posteriorly to the extent of transition metal–oxygen covalency, which serve as activity descriptors [167,168]. The oxygen reduction property of perovskite is complicated and depends on its intrinsic characteristics, electronic conductivity, and surface absorption behavior. Sunarso et al. [169] comparatively studied the intrinsic ORR activity of $LaTMO_3$ (TM = Ni, Co, Fe, Mn, and Cr) increasing in the order of $LaCoO_3$, $LaMnO_3$, $LaNiO_3$, $LaFeO_3$, and $LaCrO_3$. The yielding of HO_2^- was as low as 1.5%, suggesting a pseudo 4e$^-$ pathway. Takeguchi and co-workers [56] reported that Ruddlesden-Popper-type layered perovskite, RP-$LaSr_3Fe_3O_{10}$ (*n* = 3) as a reversible cathode catalyst for ORR and OER showed an equilibrium potential of 1.23 V with negligible overpotentials. The results of both ORR and OER testing showed that the activity of RP-$LaSr_3Fe_3O_{10}$ was much higher than that of RuO_2–IrO_2 and $LaMnO_3$/$LaNiO_3$. A negligible portion of energy is expected to be lost on the cathode by charging and discharging reactions. Reversible ORR and OER are achieved because of the easily removable oxygen present in RP-$LaSr_3Fe_3O_{10}$ (Fig. 8). Yuasa et al. [170] used a composite electrode consisting of $LaMnO_3$ and $LaNiO_3$ displayed

excellent bifunctional ORR/OER activity in alkaline solution. $LaNiO_3$ has high electrical conductivity and efficient OER activity while $LaMnO_3$ is highly active for the ORR. The combination of $LaNiO_3$ and $LaMnO_3$ presents an advantageous synergetic effect for the bifunctional ORR/OER electrocatalytic activity.

Because the perovskite has low electronic conductivity, carbon materials have been used as supports to further improve the electrocatalytic performance by establishing perovskite/carbon hybrids. The recent review of Shao's group [171] summarized the detailed perovskite/carbon composites as electrocatalysts for ORR. The prominent bifunctional electrocatalytic performance of perovskite/carbon composites exploits their prospective use in rechargeable metal–air batteries.

3.2.2.4. Metal–Nitrogen–Carbon (M–N–C). Currently, there are extensive efforts devoted to the development of metal–air batteries with different active sites. Among the various nonprecious metal catalysts, metal–nitrogen–carbon (M–N–C, M = V, Cr, Fe, Co, Ni) materials have been regarded as one of the most promising classes for ORR due to their high catalytic activity in both alkaline and acidic electrolytes. M–N–C catalysts can be produced by pyrolyzing carbon-supported nitrogen-rich metal complexes or a mixture of metal salts, nitrogen- and carbon-containing precursors [54,172]. Sun et al. [173] prepared a novel Fe–N–C composite by pyrolyzing a composite of carbon-supported Fe-doped graphitic carbon nitride (Fe-g-C_3N_4@C) at 750 °C. The composite exhibits superior ORR activity and durability in comparison to that of commercial 20 wt% Pt/C in acidic solution (Fig. 9). Xu and co-workers reported that the Fe–N/C catalyst synthesized from pyrolysis of a nitrogen-rich iron-coordinated polymer (Fe-bidppz) at 800 °C showed high ORR activity with better onset and half-wave potentials in alkaline and acidic solution and much greater durability, which was comparable to those of Pt/C catalyst [174]. The major active sites in the Fe–N/C catalyst were the Fe-N_x species, owing to the introduction of iron into the catalyst (Fig. 10). Dahn et al. investigated the oxygen reduction catalytic activity of sputtered M–C–N (M is V, Cr, Mn, Fe, Co, and Ni) films in both acid and alkaline mediums [175–177]. The ORR activity and
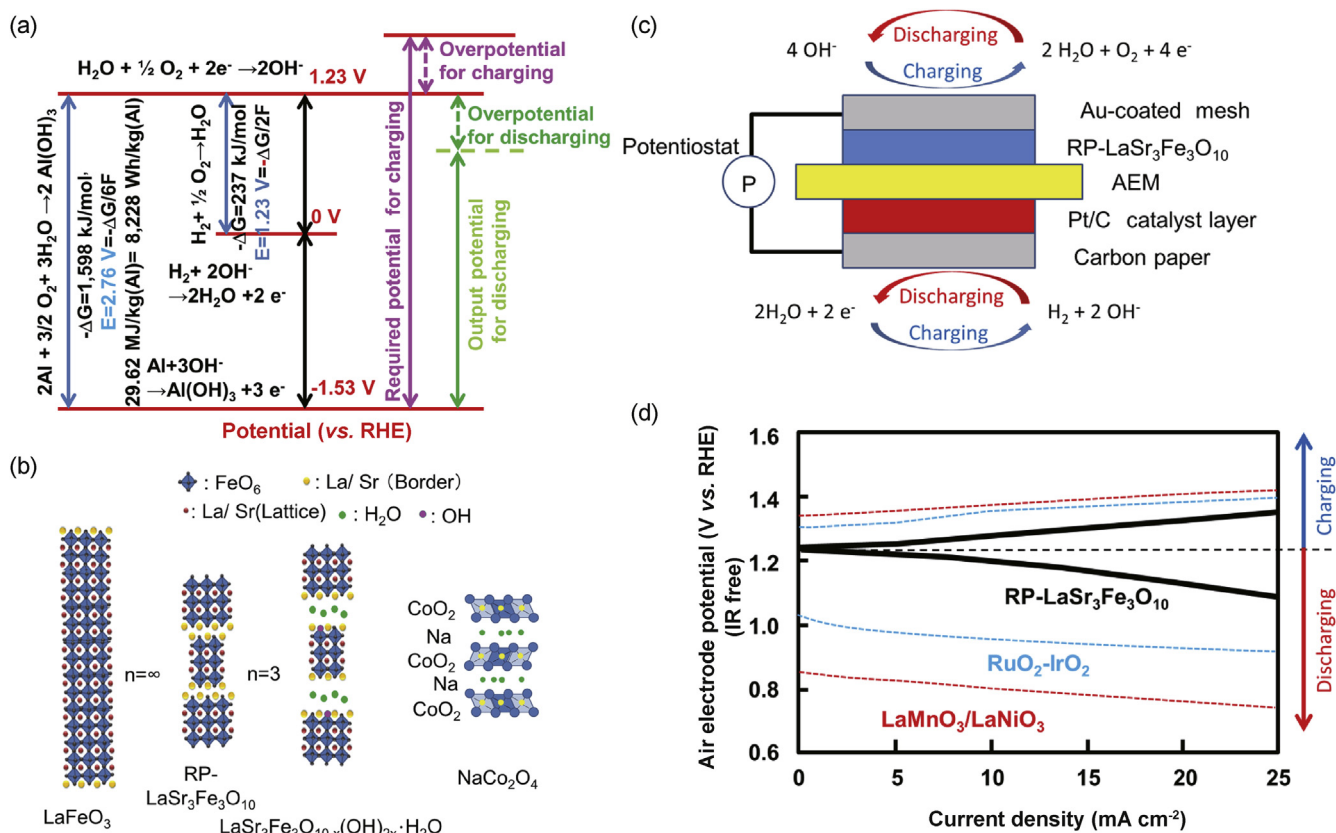
Fig. 8. (a) Energy diagram of rechargeable Al—air battery. (b) Structures of various transition metal oxides. (c) Schematic illustration of ORR and OER test unit with AEM. (d) Performance of ORR and OER of RP-LaSr$_3$Fe$_3$O$_{10}$. Terminal voltage (V) is almost equivalent to potential of the air electrode (V *vs.* RHE) [56].

durability of M—C—N catalysts are greatly affected by the M, N precursors, and pyrolysis temperatures. The optimum pyrolysis temperature is in the range of 700—900 °C [175]. In alkaline condition, the activities of the M—C—N (M is V, Cr, Mn, Fe, Co, and Ni) catalysts in order of Co > Ni > Mn > V > Cr, while in acid solution, the sequence is Fe > Co > Cr > Ni [175]. Generally, two mechanisms have been proposed to explain the oxygen reduction catalytic activity of M—N—C catalysts [176]. One involves the M—N moieties, and the other is the nitrogen dopants within the carbon matrix. Although the nature of the active sites in M—N—C catalysts is still under debate, the specific surface area and structure can greatly determine the accessibility of the active sites of the catalysts so that to affect the electrocatalytic performance. Wu and co-workers further demonstrated that M—N—C catalysts were rich in carbon nanostructures formed in-situ during catalyst synthesis, including carbon tubes, onion-like carbon, and platelets (multilayer graphene) (Fig. 11) [178—180]. The existence of transition metals was regards to be essential to catalyze the graphitization of nitrogen-carbon precursors. While CNTs and onion-like carbons appeared when ethylene diamine and Co were used for the high-temperature synthesis, the bamboo-like tubes formed from cyanamide and Fe precursors [178—180]. Although nitrogen species embedded within the in-situ-formed graphitized carbon nanostructures are likely critical to the active-site performance of the M—N—C catalysts, the detailed mechanism for active-

site formation and its bonding character/interaction with the carbon nanostructure still remain unknown.

3.2.3. Carbonaceous nanomaterials

Among the extensive research efforts dedicated to developing advanced ORR electrocatalysts, carbonaceous nanomaterials have been demonstrated as promising metal-free catalysts with satisfactory activity and durability towards ORR. On one hand, the carbonaceous catalysts have relatively wide stabilization potential windows and outstanding electronic conductivity. On the other hand, the attractiveness also depends on the structural diversity, including zero dimensional (0D) fullerene, one-dimensional (1D) carbon nanotubes, two-dimensional (2D) graphene and various three-dimensional (3D) nanostructured carbon materials. Carbon nanomaterials, including graphite, graphene, and carbon nanotube, etc. are usually utilized as catalysts or supports due to their high electronic conductivity, large specific surface area, environmental acceptability and corrosion resistance [152,158,181—186]. Very recently, Dai et al. [137] supplied an exhaustive review on nanocarbons materials (e.g., fullerenes, carbon nanotubes, graphene, carbon nitride, and 3D carbon architectures), and their recent development and challenges of metal-free catalysts based on intermolecular charge-spin-redistribution for ORR/OER/HER and fuel cell. To avoid duplicating the present reviews, this section of this review will mainly focus on reviewing the most recent progresses on
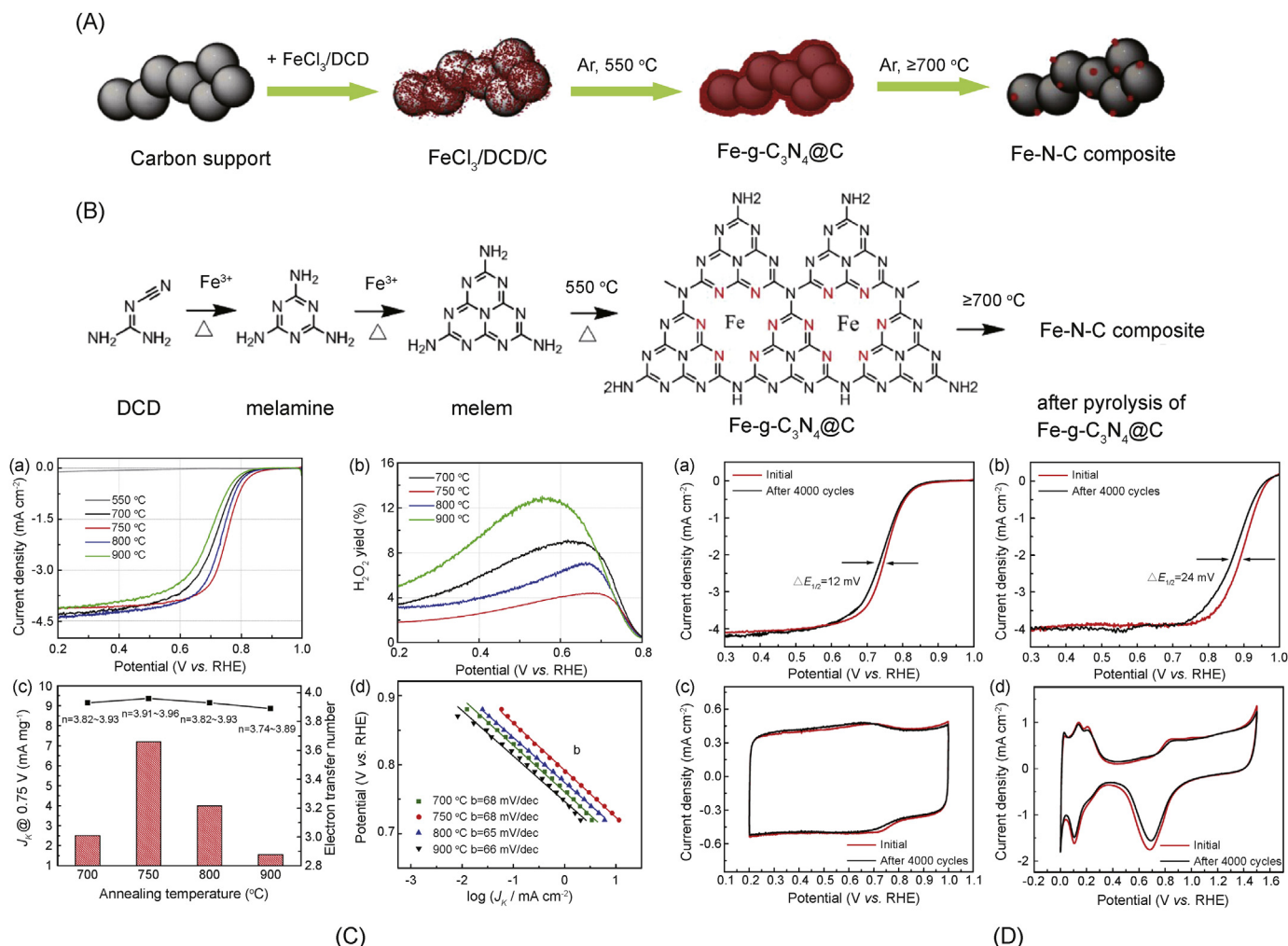
Fig. 9. (A) Schematic synthetic strategy and (B) proposed formation mechanism of the Fe−N−C composite after pyrolysis of Fe-g-C_3N_4@C. (C) (a) ORR activity of Fe-g-C_3N_4@C and pyrolyzed Fe−N−C composite. (b) H_2O_2 yield of the pyrolyzed Fe−N−C composite, in O_2-saturated 0.1 M $HClO_4$ at 900 rpm, with a scan rate of 10 mV s^{-1}. The Pt ring electrode was polarized at 1.2 V, and the catalyst loading is 0.6 mg cm^{-2}. (c) Electron transfer number at 0.4 V and the kinetic-limiting current density (J_K) at 0.75 V for the pyrolyzed Fe−N−C composite. (d) Tafel ORR plots for the pyrolyzed Fe−N−C composite. (D) ORR activity of (a) pyrolyzed 10% Fe−N−C (750 °C) composite and (b) Pt/C (20 μg Pt cm^{-2}). CV curves of (c) pyrolyzed 10% Fe−N−C (750 °C) composite and (d) Pt/C before and after the accelerated durability test (ADT) [173].

graphene-based and CNT-based nanocomposites, heteroatom-doped carbon nanostructures, three-dimensional (3D) carbon nanomaterials, and carbon quantum dots as electrocatalysts for ORR.

3.2.3.1. Carbon nanotubes- and graphene-based nano-composites. Graphene, the one-atom-thick planar sheets of sp^2-bonded carbon atoms that are densely packed in a honeycomb crystal lattice, is rapidly being explored as an alternative material for ORR catalyst supports. It has the following note-worthy advantages [183]: (1) The flexibility and immobilization of graphene nanosheets can provide a large space to accommodate the catalysts, and prevent their agglomeration; (2) The good superficial characteristics of graphene increase the solid−air contact efficiency, resulting in a large amount of oxygen adsorption on graphene; (3) The structure of graphene strengthens its electrical conductivity and the electron transfer rate on the surface of graphene; (4) The structural defects on

single layered graphene provide more active sites to stimulate the electrocatalytic activity. In recent years, significant improvements have been achieved in the extensive studies of low-Pt or non-noble metal nanomaterials dispersed on graphene with low-cost, excellent electrocatalytic activity, high stability and methanol tolerance [144,187−193]. Dai et al. [194] reported an advanced bifunctional N-doped graphene supported Co_9S_8 nanoparticles (Co_9S_8/graphene) as an electrocatalyst for ORR and OER prepared by simultaneously etching and N-doping with NH_3-plasma treatment. The hybrid shows excellent ORR and OER activity, which is close to that of the commercial Pt/C catalyst. The cobaltite oxide nanosheets/graphene (Co_3O_4/rGO) hybrid with a face centered cubic crystalline structure is prepared and developed as an effective cathode catalyst in high-performance Li−air batteries [195]. The excellent electrocatalytic performance of the Co_3O_4/rGO hybrid is attributed to the rapid electron transport kinetics and high electrocatalytic activity for ORR from the
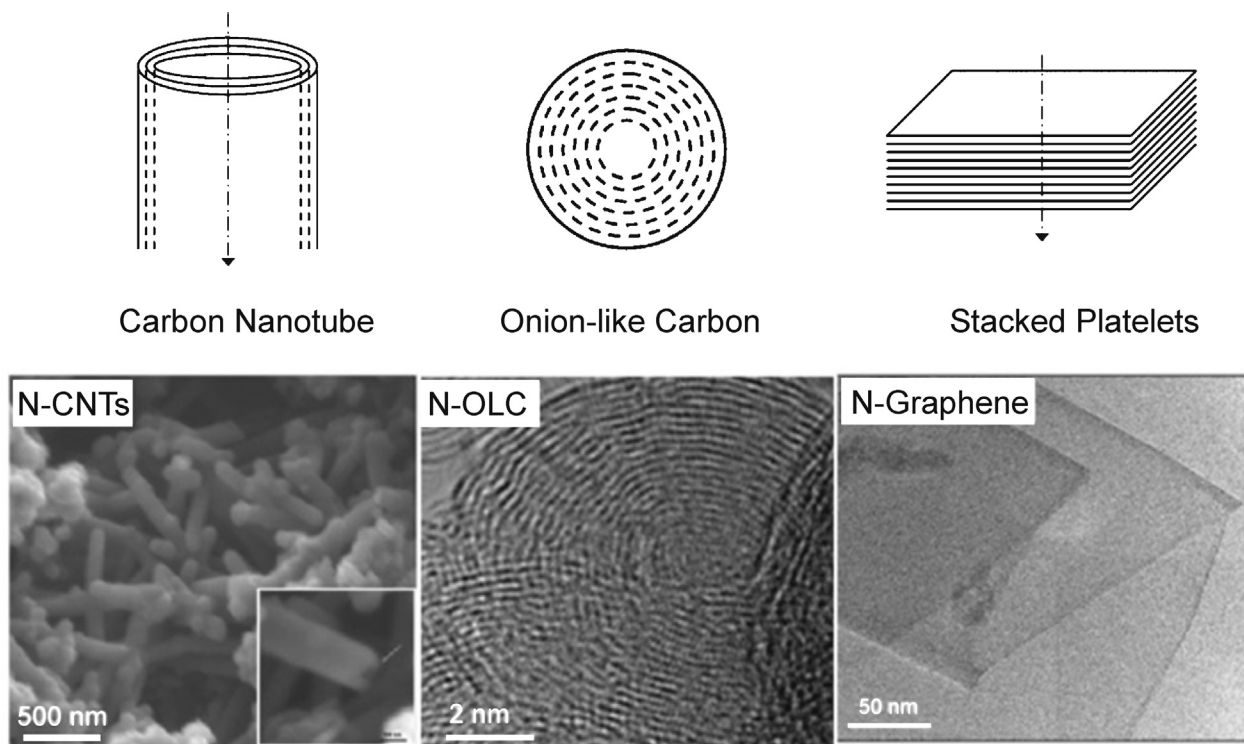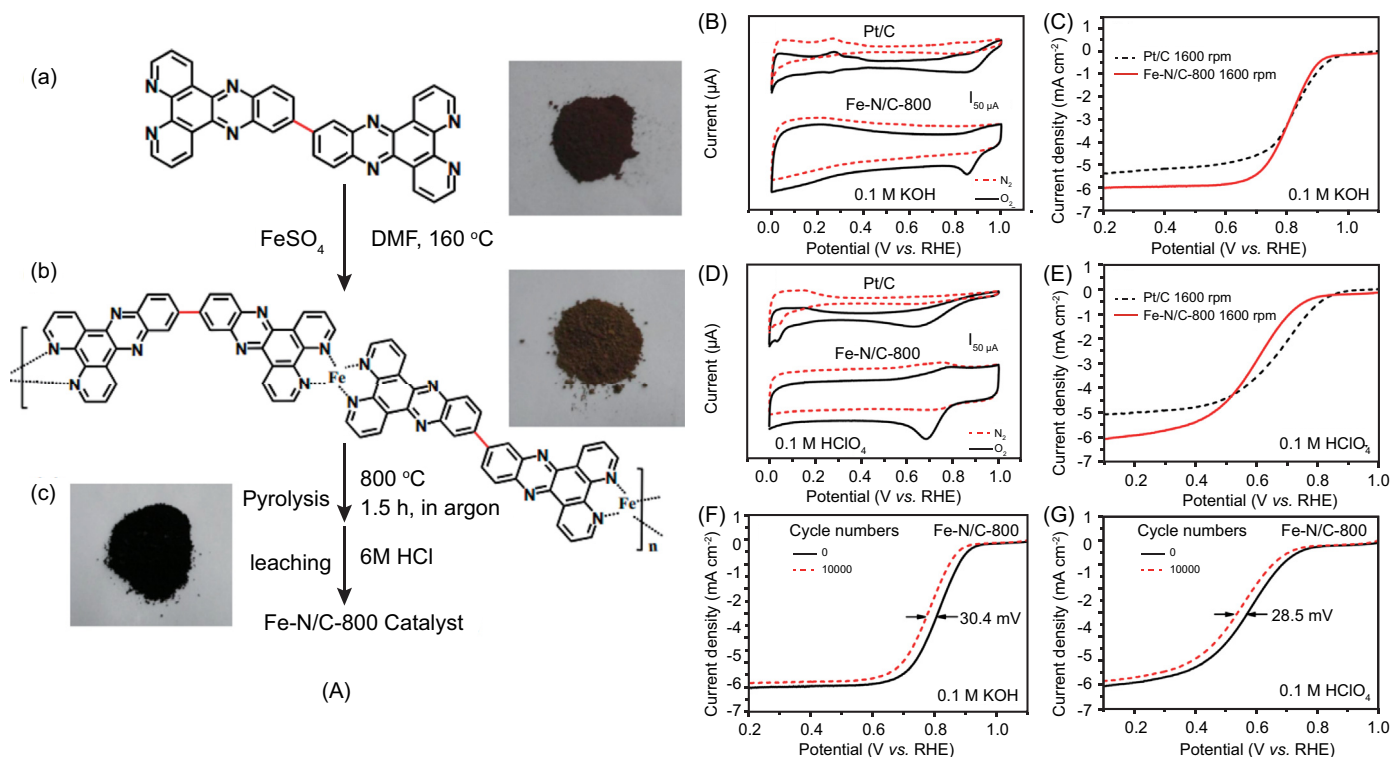
Fig. 10. (A) Schematic illustration of the synthetic process of the Fe−N/C-800 catalyst: (a) chemical structure and photograph of bidppz, (b) chemical structure and photograph of the corresponding Fe-bidppz precursor, (c) photograph of the obtained Fe−N/C-800 catalyst. (B) Cyclic voltammograms and (C) RDE voltammograms of Pt/C and Fe−N/C-800 in O$_2$-saturated 0.1 M KOH. (D) Cyclic voltammograms and (E) RDE voltammograms of Pt/C and Fe−N/C-800 in O$_2$-saturated 0.1 M HClO$_4$. Endurance test of the Fe−N/C-800 catalyst for 10 000 cycles in O$_2$-saturated 0.1 M KOH (F) and 0.1 M HClO$_4$ (G). For all tests, the catalyst loading is 0.1 mg cm^{-2} and the scan rate is 10 mV s^{-1} [174].

Fig. 11. Drawings and micrographs of in-situ nitrogen-doped carbon nanostructures in MNC catalysts: Carbon nanotubes in PANI-derived catalyst (left) [178]; onionlike carbon structure in HDA-derived catalyst (middle) [179]; and graphene formed in PANI-derived catalyst (right) [180].
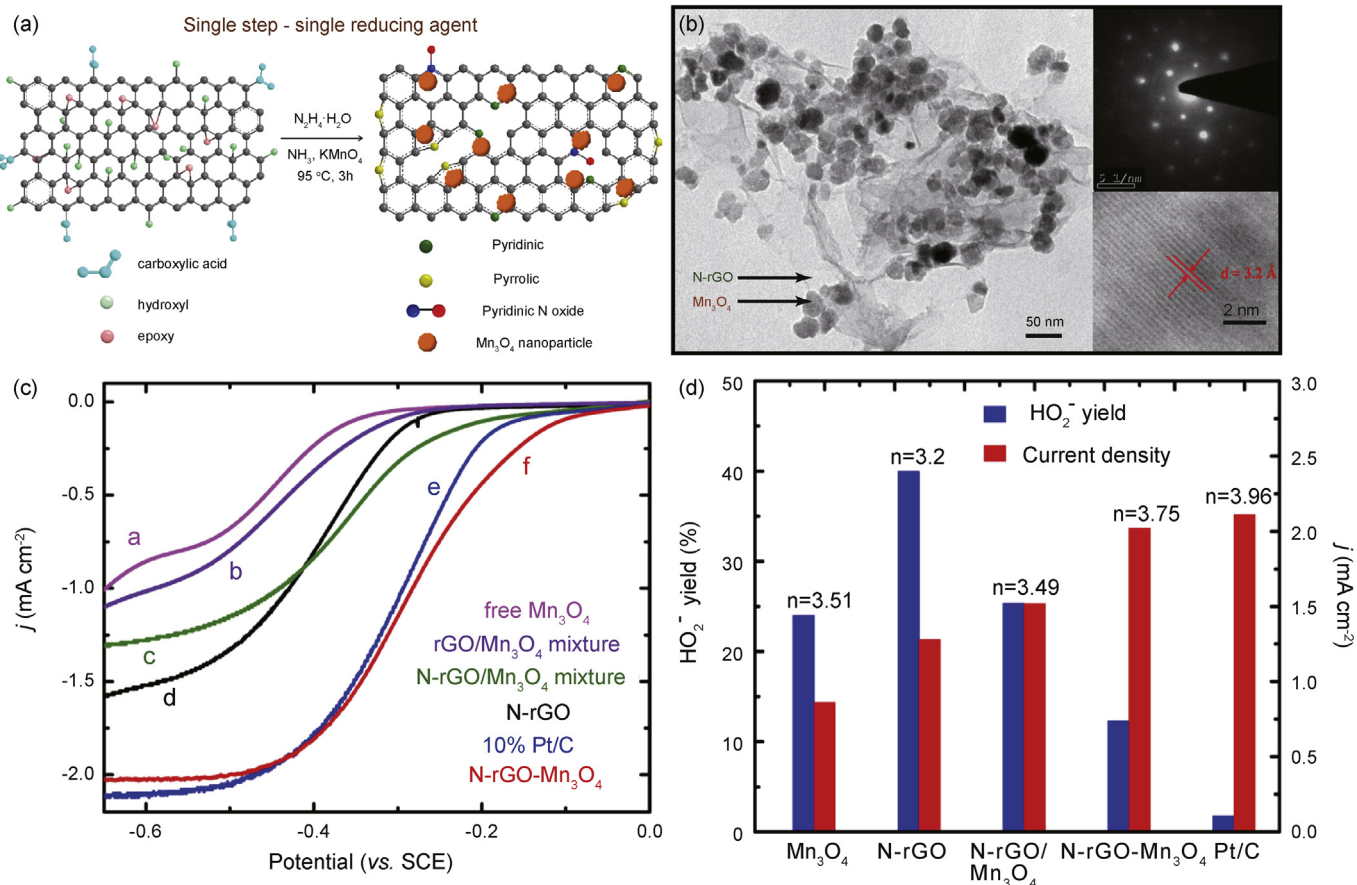
Fig. 12. (a) Scheme of one-pot synthesis of N-rGO-Mn$_3$O$_4$ hybrid material. (b) TEM images of the N-rGO-Mn$_3$O$_4$ hybrid material. (c) Polarization curves of the electrocatalytic performance of N-rGO-Mn$_3$O$_4$ and other synthesized catalysts towards ORR at 1600 rpm. (d) Plot illustrating the percentage of peroxide yield, current density and number of electrons transferred for all of the catalysts. Peroxide yield, current density and number of electrons were calculated using the ring/disk current at the potential of −0.6 V [158].

synergetic effects of cubic Co$_3$O$_4$ nanosheets and graphene. Bag et al. [158] successfully prepared the Mn$_3$O$_4$/N-rGO hybrid composed of nitrogen doped reduced graphene oxide (N-rGO) and Mn$_3$O$_4$ by the one-step in-situ reduction using hydrazine (Fig. 12), and the hybrid material exhibits high electrocatalytic activity towards ORR under alkaline condition and favors the four-electron pathway for ORR. The synergistic effect of N-rGO and Mn$_3$O$_4$ enhances the overall performance of the hybrid catalyst.

Due to their high tensile modulus, high specific surface area, mesoporous structure, and good electrical properties, CNTs can also be used as good catalyst supports [196−200] for applications in metal−air batteries. Wang et al. [201] reported highly active and stable Co-doped iron pyrite (FeS$_2$) electrocatalysts on carbon nanotubes (Fe$_{1-x}$Co$_x$S$_2$/CNT) hybrid for the hydrogen evolution reaction (HER). Owing to the appropriate Co doping ratio and intensive covalent coupling to the carbon nanotubes, the Fe$_{0.9}$Co$_{0.1}$S$_2$/CNT hybrid catalyst achieves the lowest overpotential of ~0.12 V at 20 mA cm^{-2}, a Tafel slope of ~46 mV dec^{-1}, and excellent stability over 40 h in acid condition. Density functional theory (DFT) calculations reveal that the sulfur in a Fe$_{0.9}$Co$_{0.1}$S$_2$ structure was responsible for the active sites of proton adsorption and reduction. A bifunctional Co$_3$O$_4$ nanocrystal on nitrogen-doped core-shell carbon nanotube−graphene nanoribbon (Co$_3$O$_4$/N-csCNT-GNR) composite catalyst with high OER and ORR efficiency has been reported, which exhibited strong synergistic coupling of Co$_3$O$_4$ on nanocarbon scaffolds by harnessing and combining the strengths of GR and MWCNTs (Fig. 13) [202]. It can be seen that the core-shell structure serves as an electron 'super-highway' for both OER and ORR whilst the intercalated csCNT−GNR acts as a backbone scaffold for Co$_3$O$_4$ NPs by providing abundant adsorption sites, mechanical strength, and electrical conductivity. Zhao et al. [203] designed spinel Mn−Co oxide nanoparticles partially embedded in nitrogen-doped carbon nanotubes and tested the catalytic ORR and OER performance, finding that it surpassed the activity of Pt/C, RuO$_2$, and IrO$_2$ and non-precious-metal bifunctional catalysts in metal−air batteries (Fig. 14). The nitrogen functionalized carbon groups in NCNTs act as active sites for ORR and OER. The enhanced catalytic activity is contributed to the synergetic effect from the nitrogen groups in the NCNTs and the spinel Mn−Co oxide particles.

3.2.3.2. Heteroatom-doped carbon nanostructures. Previous results have shown that pristine carbon materials have poor intrinsic ORR activity with a dominant two-electron pathway
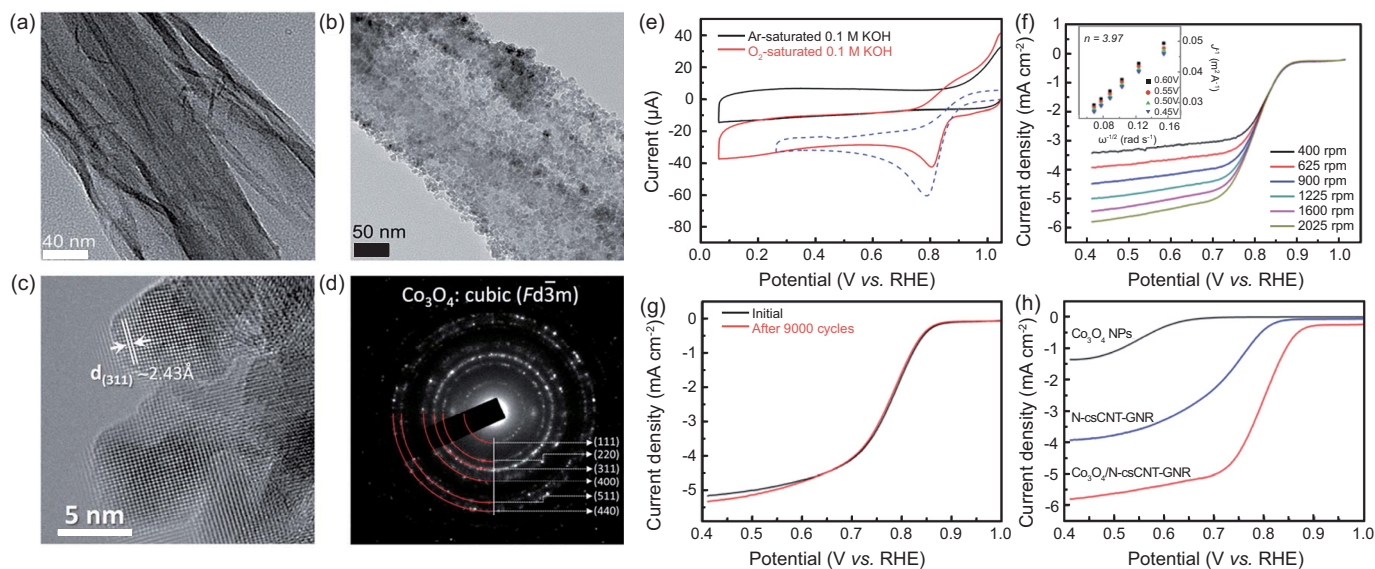
Fig. 13. (a) TEM image of csCNT—GNR prepared at 200 W for 4 min. (b) and (c) HRTEM images of Co₃O₄/N-csCNT—GNR under low and high magnifications. (d) Electron diffraction pattern of Co₃O₄/N-csCNT—GNR obtained with TEM. (e) Cyclic voltammograms obtained with a Co₃O₄/NcsCNT—GNR modified GC electrode in O₂ saturated and Ar saturated 0.1 M KOH solutions, respectively. The blue dashed line indicates the Pt/C modified GC electrode in O₂ saturated 0.1 M KOH solution. (f) RDE voltammograms of Co₃O₄/N-csCNT—GNR obtained at various rotation speeds in O₂ saturated 0.1 M KOH. Inset in (f) depicts the linear relationship in the Koutecky—Levich plot. (g) RDE voltammograms obtained with a Co₃O₄/N-csCNT—GNR modified GC electrode in O₂ saturated 0.1 M KOH solution at 1600 rpm before and after 9000 cycles of potential scan from 0.46 V to 0.96 V. (h) RDE voltammograms obtained with Co₃O₄ NPs, N-csCNT—GNR and Co₃O₄/N-csCNT—GNR modified GC electrodes in O₂ saturated 0.1 M KOH solution at 2025 rpm. All measurements were carried out at a scan rate of 5 mV s^{-1} [202].

[6,204,205]. Thus, chemical modification such as heteroatom doping by increasing the structural disorder or forming heteroatom functionalities becomes a valid method to enhance their ORR catalytic activity [183,185,206—211]. The most common doping elements include N, B, S, P, and F. Although the specific mechanisms are still under dispute, the introduction of heteroatoms is identified to create carbon active sites adjacent to the heteroatoms and facilitates the O—O bond breaking of oxygen molecules by regulating the binding energy of oxygen [212—214]. Paraknowitsch and Thomas gave
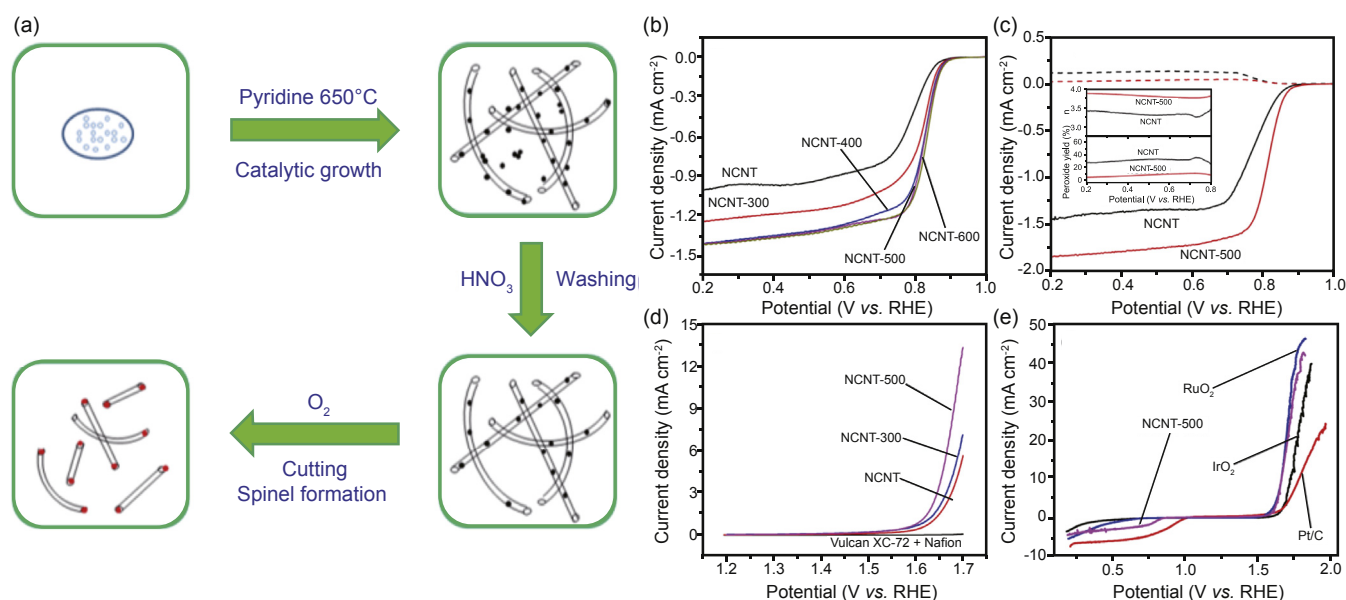

Fig. 14. (a) Synthesis of spinel Mn—Co oxide nanoparticles partially embedded in NCNTs. (1) catalytic growth of NCNTs using a Co—Mn—Al—Mg catalyst. (2) Removal of exposed catalyst nanoparticles with poor contact with carbon by washing in dilute HNO₃. (3) Formation of spinel oxide partially embedded in NCNTs by short exposure to air at elevated temperatures (oxidative cutting). (b) Linear sweep voltammograms at 100 rpm and 5 mV s^{-1}. (c) RRDE voltammograms at 400 rpm and 5 mV s^{-1}. Inset: peroxide yield and electron transfer number (n) at various potentials. (d) OER current densities of the blank experiment (glassy carbon modified with vulcan XC-72/nafion), NCNTs, NCNT-300, and NCNT-500 at 1 mV s^{-1}. (e) ORR and OER activities of NCNT-500, Pt/C, IrO₂, and RuO₂ at a scan rate of 5 mV s^{-1} [203].
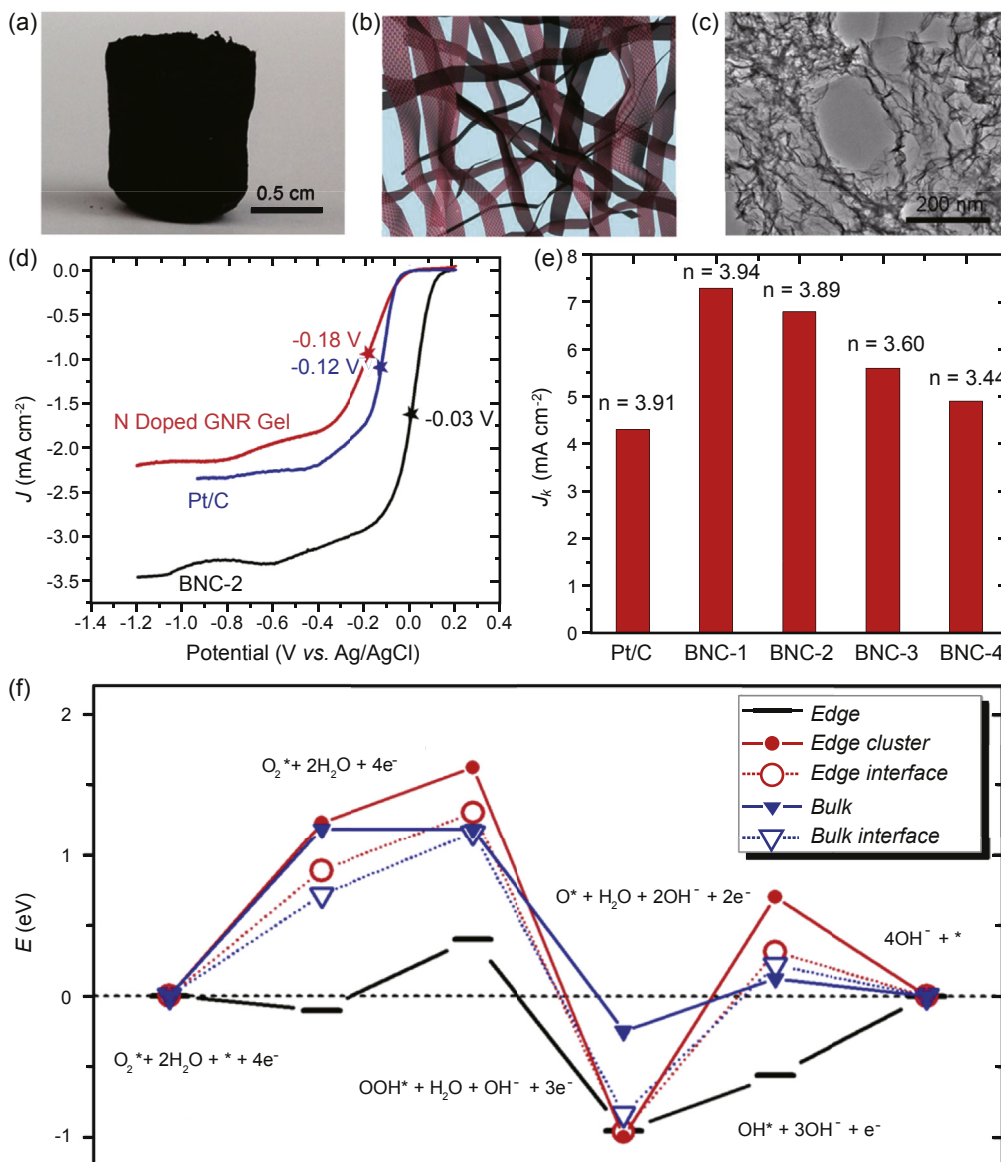
Fig. 15. (a) Photograph showing the morphology of BNC NR aerogels. (b) Schematic diagram of 3D BNC NR aerogels. (c) TEM image of the BNC NR aerogels showing its 3D porous structure. (d) Disk current densities of the RRDE versus potential derived from BNC-2, N-doped GNR aerogels, and commercial Pt/C catalyst. (e) Comparison of the ORR performances of different BNC NR aerogels and commercial Pt/C catalyst in kinetic current densities (J_K) and electron (f). Free energy diagram for ORR on different models for comparison under the conditions of pH = 13 and the maximum potential allowed by thermodynamics. The proposed associative mechanism involves the following steps: (1) $O_2 + 2H_2O + * + 4e^- \rightarrow O_2* + 2H_2O + 4e^-$; (2) $O_2* + 2H_2O + 4e^- \rightarrow OOH* + H_2O + OH^- + 3e^-$; (3) $OOH* + H_2O + OH^- + 3e^- \rightarrow O* + H_2O + 2OH^- + 2e^-$; (4) $O* + H_2O + 2OH^- + 2e^- \rightarrow OH* + 3OH^- + e^-$; (5) $OH* + 3OH^- + e^- \rightarrow 4OH^- + *$, where * denotes an active site on the catalyst surface [216].

an excellent review on the recent progress in the development of B-doped, P-doped, and S-doped carbons for fuel cell applications [215]. To avoid duplicating the above review, this section will only focus on reviewing the recent progress on co-doped carbons with heteroatoms for ORR in alkaline media. Tour and co-workers [216] reported that nanoribbons of boron- and nitrogen-substituted graphene can be used as efficient electrocatalysts for ORR (Fig. 15). The catalyst possesses the highest onset and half-wave potentials, and a four-electron transfer pathway with low hydrogen peroxide yield. First-principles calculations suggest that such excellent electrocatalytic properties originate from the abundant edges of

boron- and nitrogen-co-doped graphene nanoribbons, which significantly reduce the energy barriers of the rate-determining steps of ORR. Xia et al. [217] successfully synthesized homogeneously dispersed cobalt sulfide/N,S-co-doped porous carbon nanocomposites by a simple one-step method as high-performance electrocatalysts (Fig. 16). The nanocomposites, possess a unique core-shell structure, high porosity, and homogeneous dispersion of active components together with N and S-doping effects. It not only shows excellent electrocatalytic activity towards ORR with a high onset potential and four-electron pathway and OER with a small overpotential of 0.47 V for 10 mA cm^{-2} current density, but also exhibit
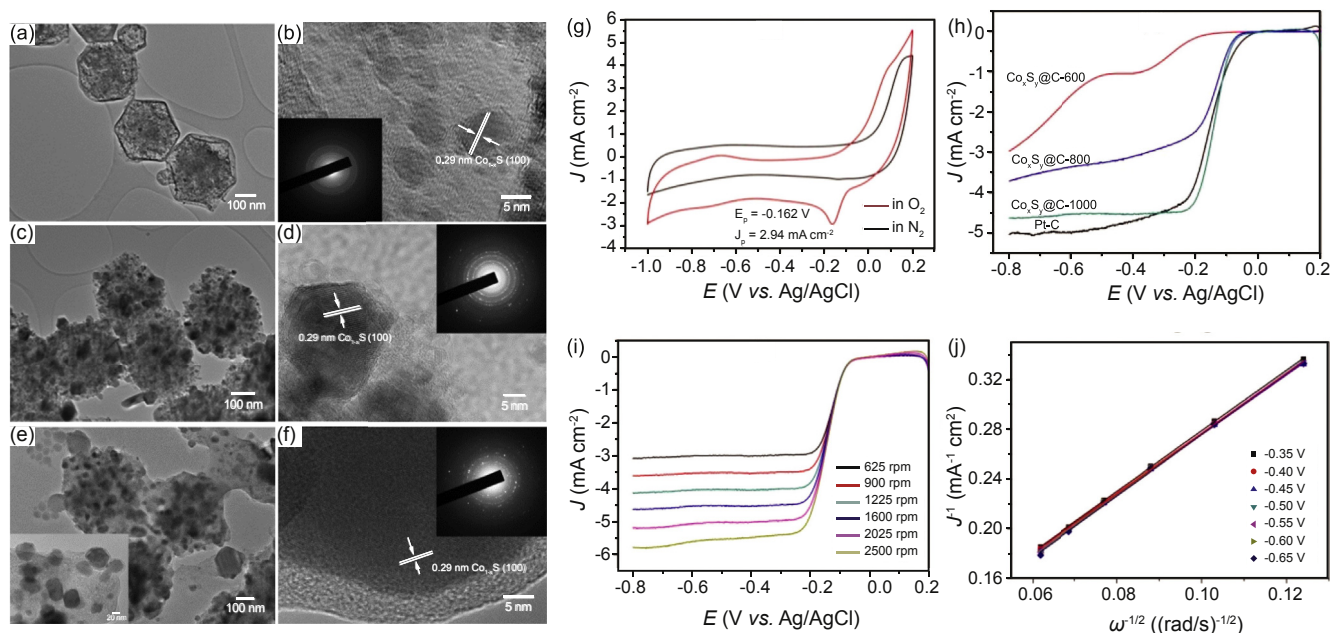
Fig. 16. TEM images of (a and b) Co_xS_y@C-600; (c and d) Co_xS_y@C-800 and (e and f) Co_xS_y@C-1000. The insets in (b), (d) and (f) are SAED patterns for the corresponding sample; (g) CV curves of the Co_xS_y@C-1000 composite in N_2- or O_2-saturated 0.1 M KOH. (h) ORR polarization curves of Co_xS_y@C-600, Co_xS_y@C-800, Co_xS_y@C-1000, and Pt/C at 1600 rpm. (i) ORR polarization curves of Co_xS_y@C-1000 at different rotating speeds. (j) K—L plots of Co_xS_y@C-1000 at different potentials [217].

superior stability (92%) to the commercial Pt/C catalyst (74%) in ORR and promising OER stability (80%). Dai et al. [218] developed a scalable approach to prepare N and P co-doped mesoporous carbon foams by pyrolyzing polyaniline aerogels obtained from a template-free polymerization of aniline in presence of phytic acid. The catalyst shows efficient catalytic activities for both ORR and OER, and good stability (600 cycles for 100 h of operation) in a three-electrode rechargeable battery. First-principles simulations reveal that the N and P co-doping and the highly porous network of the carbon foam are crucial to generating bifunctional activity towards both ORR and OER (Fig. 17). In another paper [219], a robust, highly efficient and an environmentally benign method was developed to introduce S to the GO-polydopamine (PDA) hybrids in PBS buffer to produce N,S-co-doped mesoporous carbon nanosheets, which exhibited much better performances than most of the other benchmarked bifunctional ORR and OER catalysts, which was attributed to their multiple doping, unique porous architecture and excellent charge-transfer ability. Due to the physicochemical versatility and structural tunability of PDA, this work provides a universal platform towards further development of heteroatom doped carbon materials as the highly efficient electrocatalysts for metal—air batteries (Fig. 18).

3.2.3.3. Three-dimensional (3D) carbon nanomaterials. For practical applications, 3D nanostructured cathode materials having a large specific surface area, good mechanical integrity and facilitated ion diffusion/charge transfer paths are highly desirable. M. Pumera et al. [220] showed that mechanically rigid 3D graphene deposited on nickel template can act as efficient catalyst for ORR. Huang and co-workers [221] developed novel

3D sulfur-nitrogen co-doped carbon foams with hierarchical pore structures. Such excellent catalytic activity and stability outperforming commercial Pt/C catalyst can be attributed to the synergistic effect and high electron transfer supplied by 3D continuous networks (Fig. 19). Li et al. [222] reported similar work on the nitrogen and phosphorus dual-doped porous carbon foams as efficient electrocatalysts for ORR in basic, neutral, and acidic media, which exhibit better catalytic activity and much higher stability than those of the commercial Pt/C catalyst. N,S co-doped porous carbon synthesized from ordered mesoporous carbon and trace ionic liquids (ILs) as an ORR catalyst exhibits comparable catalytic activity and better stability than Pt/C catalyst in alkaline solution [223]. Additionally, Wong et al. [224] demonstrated that 3D nitrogen-doped graphene prepared by pyrolysis of graphene oxide with polypyrrole displayed excellent catalytic activity for ORR and OER and high stability compared with the commercial Pt/C catalyst. 3D B,N co-doped graphene foams were prepared by a modified chemical vapor deposition (CVD) method as highly efficient ORR catalysts, which exhibited much better than their undoped counterparts [225]. In another paper, an erasable-promoter-assisted hydrothermal method coupled with pyrolysis was developed to prepare N-CNT aerogels, which exhibited remarkable ORR activity in alkaline medium with a four-electron transfer pathway [226] (Fig. 20). As can be seen from the above discussions, heteroatom doping of 3D carbon nanomaterials has been verified as a simple and effective approach to enhance the electrocatalytic activity for ORR. Furthermore, 3D nanocarbon has also been considered as an alternative support to enhance electrocatalytic performance. Sun et al. [153] reported a spinel $ZnCo_2O_4$/N-doped carbon nanotubes ($ZnCo_2O_4$/NCNT) composite which showed highly efficient catalytic activity via a four-electron
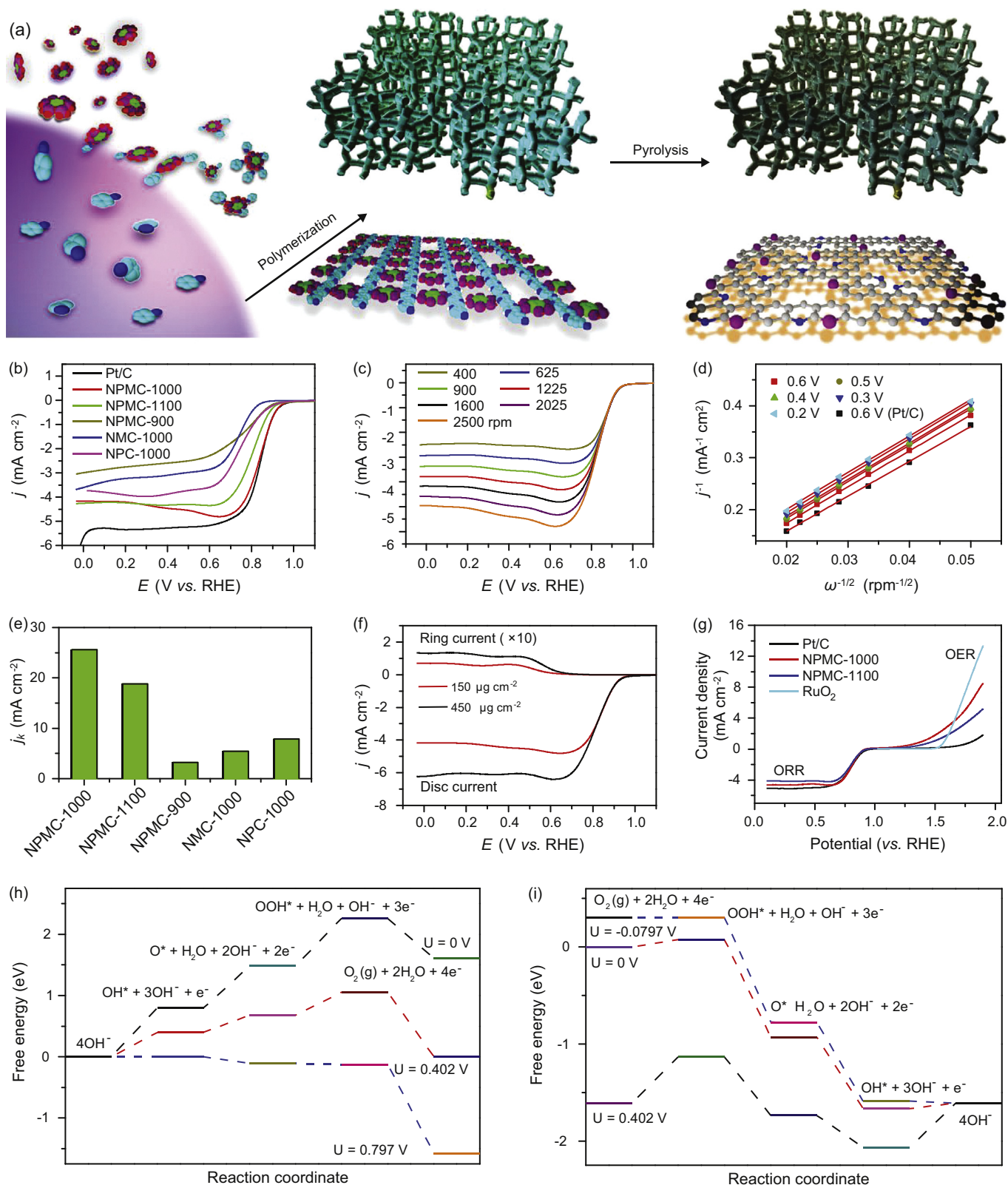
Fig. 17. (a) Schematic illustration of the preparation process for the N and P co-doped porous carbon (NPMC) foams. (b) Linear scan voltammogram (LSV) curves for NPMC-900, NPMC-1000, NPMC-1100, NMC-1000, NPC-1000 and commercial Pt/C catalyst at an RDE (1600 rpm) in O₂-saturated 0.1 M KOH solution. (c) LSV curves of NPMC-1000 in oxygen-saturated 0.1 M KOH at various rotating speeds. (d) K−L plots for NPMC-1000 and Pt/C at various potentials. (e) Kinetic current of various samples for O_2 reduction at 0.65 V. (f) RRDE measurements (1600 rpm) of ORR at an NPMC-1000 electrode with different catalyst loadings. (g) LSV curves of NPMC-1000, NPMC-1100, RuO_2 and commercial Pt/C catalyst on an RDE (1600 rpm) in 0.1 M KOH, showing the electrocatalytic activities towards both ORR and OER. (h) and the ORR pathway. (i) on N,P co-doped graphene in alkaline media [218].
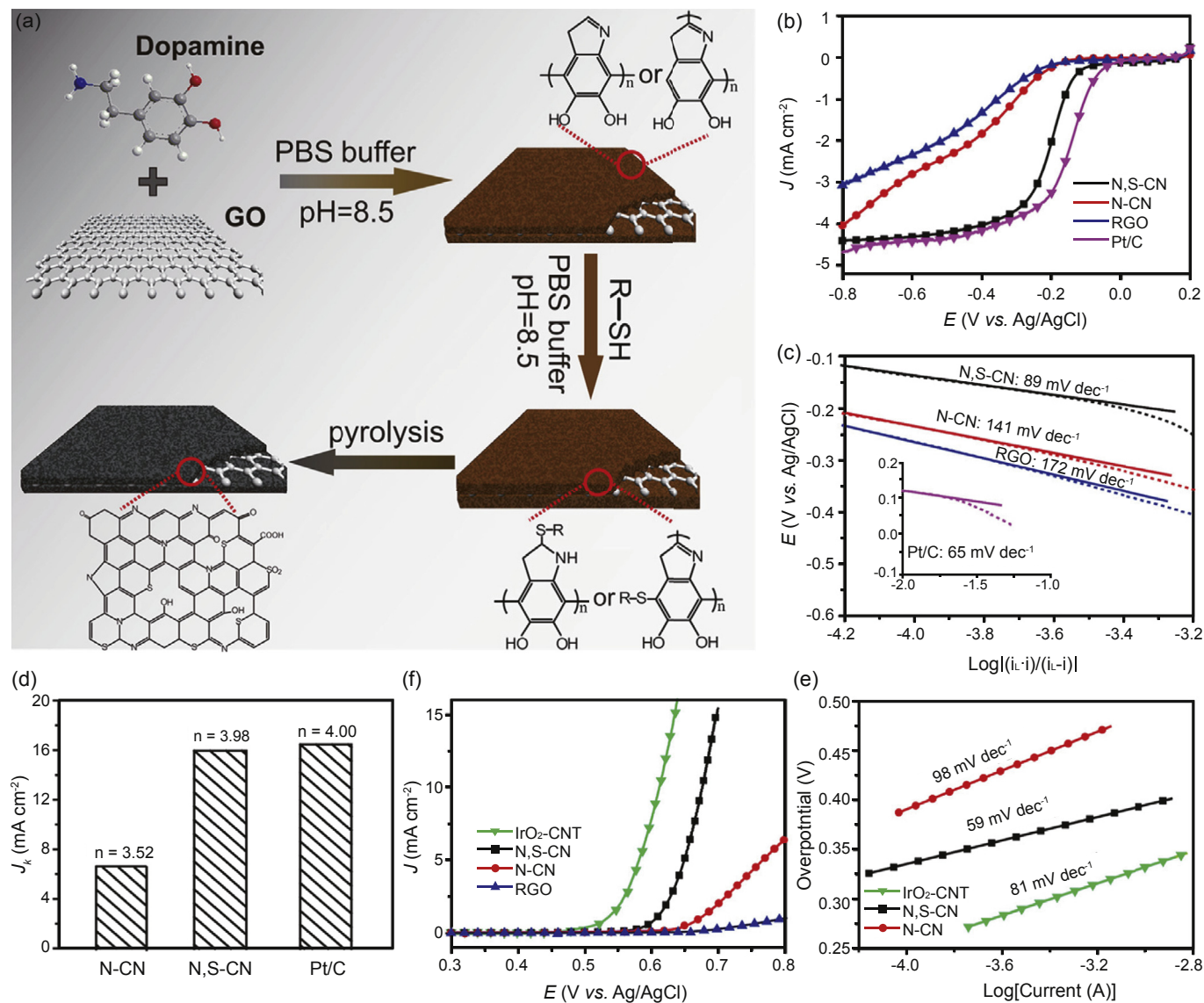
Fig. 18. (a) Fabrication of GDS derived carbon nanosheets (N,S-CNs), where R-SH refers to 2-mercaptoethanol. (b) ORR LSVs at a sweep rate of 5 mV s^{-1}. (c) ORR Tafel slope obtained from the LSVs at 1600 rpm, (Inset: Tafel slope of Pt/C). (d) Kinetic limiting current density (J_k) and electron transfer number (n) of N–CN, N, S–CN and Pt/C. (e) OER LSVs at a sweep rate of 5 mV s^{-1}. (f) OER Tafel plots [219].

pathway in alkaline solution, and superior durability over commercial Pt/C catalyst. Wang et al. [227] reported that platinum nanoparticle decorated three-dimensional (3D) graphene assembled on fluorine-doped tin oxide (FTO) electrodes (Pt/3D-G/FTO) exhibited improved electrocatalytic activity. A novel 3D nanoarchitecture comprising in-situ-formed N-doped CoNi alloy-encapsulated carbon nanotubes (CoNi-NCNTs) grown on N-doped porous carbon nanosheets (NPCNs) was designed [228]. The hybrid showed efficient catalytic activity, high selectivity, and superior durability compared with the commercial Pt/C catalyst, which was even better than those of most previous reported carbon-based electrocatalysts. The positive catalytic properties can be attributed to the unique morphology and defect structures, high porosity, conductive networks, and strongly interacting CoNi-NCNT and NPCN in the hybrid [228]. Yang and co-workers fabricated a hybrid of CoFe$_2$O$_4$

nanoparticles supported on nitrogen/sulfur dual-doped three-dimensional reduced graphene oxide networks (CFO/NS-rGO) possessing a pronounced ORR activity, superior OER activity in comparison with the state-of-the-art RuO$_2$/C catalyst and high durability [229]. The 3D carbon-based nanomaterials show comparable even outperforming electrocatalytic activity with four-electron transfer pathways and stability in comparison to the state-of-the-art precious metal-based catalysts. Recently, exhaustive reviews on three-dimensional graphene-based nanomaterials [230] and advanced carbon nanomaterials [231] as electrocatalysts with high efficiency for ORR were given.

In more recent studies, designing nanocomposites by combining two carbon materials with unique structures has become a promising means for oxygen reduction. For example, Yu et al. [232] reported a type of nitrogen-doped graphene/carbon nanotube nanocomposite synthesized by a hydrothermal process
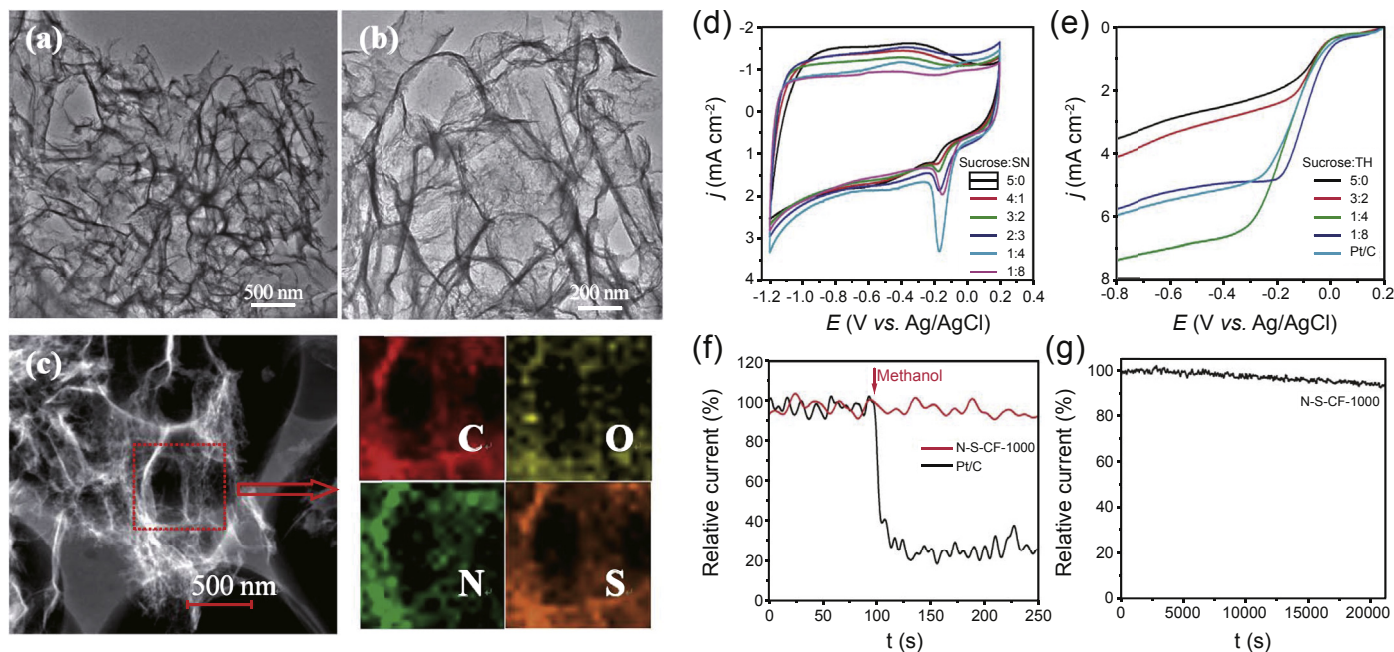
Fig. 19. (a and b) Typical TEM, (c) STEM elemental mapping images for S−N−CF-1000, (d) CVs for various catalysts obtained under different mass ratios of sucrose to thiourea, (e) LSV curves for various catalysts and a Pt/C catalyst at a rotation rate of 1600 rpm. Chronoamperometric responses of S−N−CF-1000 and Pt/C catalyst, (f) with 3 M methanol added at around 90 s, and (g) at 0.40 V in an O_2-saturated 0.1 M KOH solution [221].

which displayed an approximate four-electron pathway for ORR. Chen's group [233] reported a catalyst consisting of multilayer highly porous graphene encapsulating CNTs synthesized by ammonia treatment and controlling the temperature of mixture of iron, PANI and carbon nanotubes. The nanocomposite shows improved catalytic activity towards ORR (Fig. 21). Choi et al. [234] subsequently utilized the electrostatic layer-by-layer self-assembling approach (Fig. 22A) to prepare a graphene-CNT self-assembly (GCA) as a metal-free ORR electrocatalyst. The resultant N-doped GCA with a large surface area was demonstrated to facilitate the transfer of electrons through CNTs and reactants (e.g., oxygen and protons) through the interspace of graphene layers, and hence superior ORR performance (0.91 V onset potential and 2.13 mA mg^{-1} at 0.75 V) to that of catalysts derived from only graphene (0.86 V, 0.34 mA mg^{-1}) or NCNTs (0.80 V, 0.02 mA mg^{-1}) in acidic media. In addition, the N-doped GCA showed much higher durability than that of only graphene (NGr), NCNT, or commercial Pt/C catalysts in severe operation conditions, with low production of peroxide in ORR (Fig. 22B). In another paper, a unique graphene-carbon nanotubes composite doped with both nitrogen and sulfur (GC-NLS) was prepared and it provided ORR onset potential increases of 50 and 70 mV in comparison to those of co-doped graphene and nanotubes, respectively. The excellent electrochemical catalytic activity and stability can be due to the incorporation of nitrogen and sulfur and synergistic enhancements provided by the nanocomposite ingredients [235] (Fig. 23).

3.2.3.4. Carbon quantum dots. The carbon nanomaterials often display different morphologies, such as one-dimensional (1D) carbon nanowires/nanotubes, two-dimensional (2D) graphene nanosheets and three-dimensional (3D) graphene

and carbon nanospheres, and so on. In particular, the ORR requires high-quality graphene-based catalysts with specified surface chemical structures, which are critical to electro-catalyze the sluggish reaction [236]. Recently, graphene quantum dots (GQDs) have emerged as a new class of zero-dimension (0D) carbon nanomaterials with a size below 10 nm and a single atomic layer of nano-sized graphite, which display unusual chemical and physical properties due to their strong quantum confinement and edge effects [237,238]. However, the development and application of GQDs are still in its infancy, especially in electrocatalysis. There are a lot of oxygen-rich functional groups on the surface of GQDs. Thus, the electroneutrality of GQDs is broken, producing abundant positively charged active sites in favor of O_2 surface adsorption. Additionally, the active sites on the edge of GQDs are also greatly advantageous in promoting ORR. For example, the surface-like multidimensional architecture of GQDs with O- and N-rich functional groups was prepared and possesses superior electrocatalytic activity toward ORR [239]. Valentin et al. [240] reported single and multiply doped graphene quantum dots prepared via an electrochemical method favored a four-electron pathway of oxygen to water. Interestingly, the presence of oxygen groups influences not only the activity but also the selectivity of the electron transfer paths for ORR (Fig. 24). N-doped GQDs with the feature of oxygen-rich functional groups exhibiting efficient electrocatalytic ability for ORR were reported [238]. In addition, Li et al. [241] demonstrated that nitrogen-functionalized GQDs showed a highly size-dependent electrocatalytic activity. This size dependence may be due to the higher HOMO levels in larger GQDs which as a result can be more easily oxidized. Due to their small dimension, GQDs can be easily interfaced to other
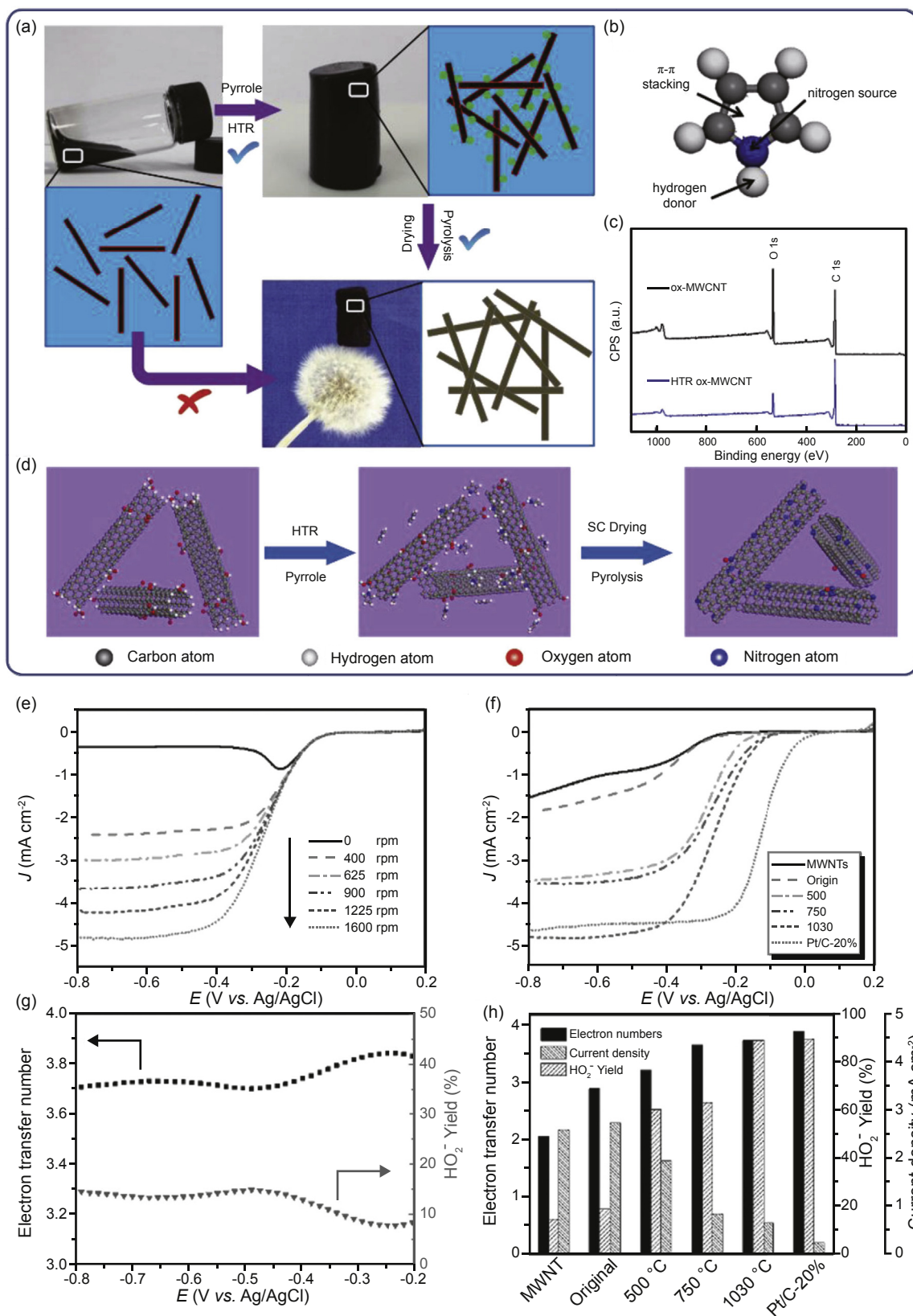
Fig. 20. (a) Synthetic strategy of N-CNT aerogels from ox-MWNTs. (b) Roles of pyrrole in the preparation of N-CNT aerogels. (c) XPS spectra of ox-MWNTs before (black) and after (blue) hydrothermal reaction (HTR). (d) Model schematic diagram of the synthesis of N-CNT aerogels. ORR performance of N-CNT aerogels. (e) The linear sweep voltammetry (LSV) curves of N-CNT-1030 at various rotation speeds. (f) LSV curves of pristine MWNTs, N-CNT-0, N-CNT-500, N-CNT-750, N-CNT-1030, and Pt/C catalyst at 1600 rpm. (g) The potential-dependent transfer electron number and HO_2^- yield of N-CNT-1030 derived from RRDE measurement at 1600 rpm. (h) The comparison of electron transfer number, HO_2^- yield, and catalysis current density (1600 rpm, 0.4 V *vs.* Ag/AgCl) of various catalysts [226].
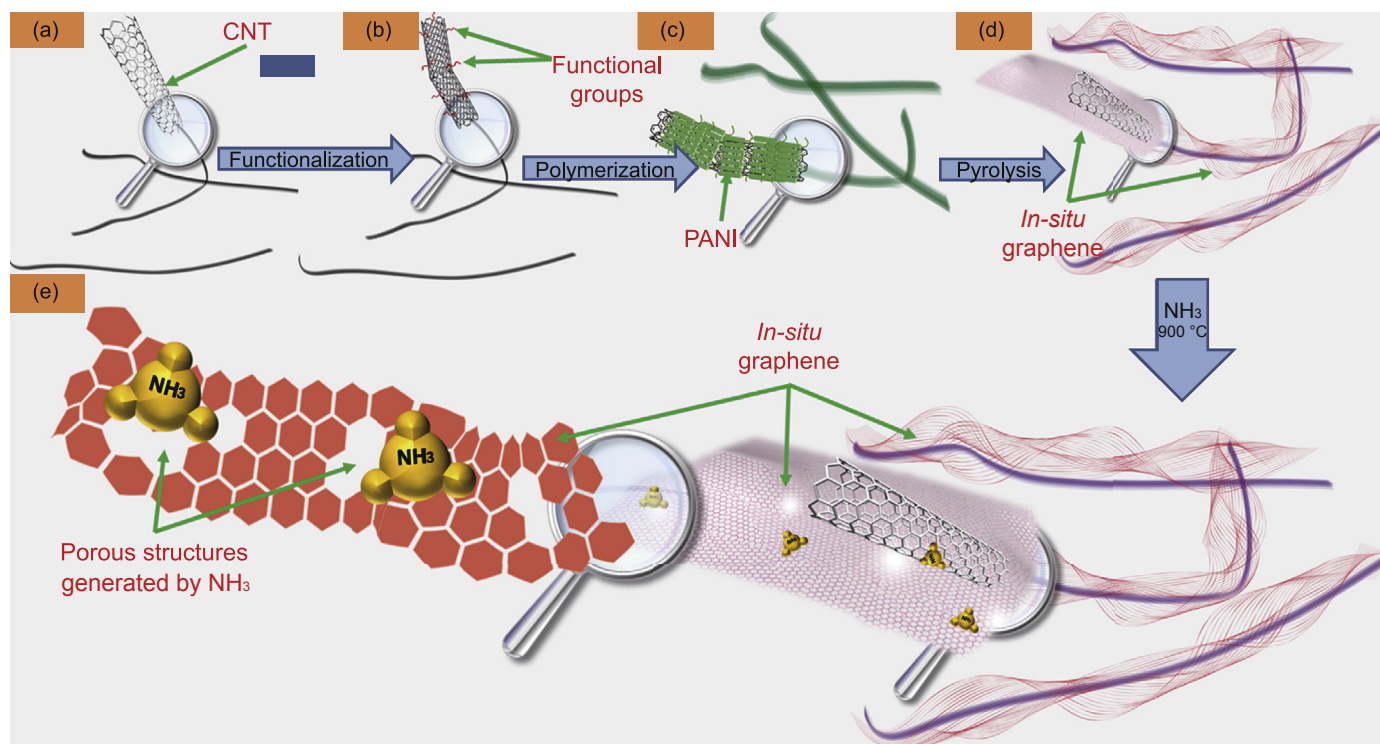
Fig. 21. Schematic of the catalyst synthesis procedure, (a) starting with CNT, (b) after functionalization to FCNT, (c) polymerized FeCl$_3$-PANI-FCNT composite, (d) pyrolyzed FeP–C_Ar, and (e) NH$_3$-treated Fe–P–C_Ar-NH900 [233].

nanomaterials in order to build more complex systems. For example, Chen et al. [242] demonstrated that graphene quantum dots-supported Pt nanoparticles showed drastically enhanced ORR catalytic activity, in comparison to commercial Pt/C catalysts. Qu et al. [243] proposed that a novel metal-free catalyst composed of GQDs and multi-walled carbon nanotubes (MWCNTs) exhibited a significant synergistic effect on enhanced catalytic activity for ORR. The increased amount of introduced GQDs has a positive effect on the peak current density and reduction peak position due to the semiconducting nature of GQDs [243]. Graphene quantum dots rich in carbonyl and carboxylic groups grown on sulfur doped graphitic carbon nitride (s-g-C$_3$N$_4$) nanosheets were synthesized by a hydrothermal method and exhibited remarkably better catalytic activity for ORR [244] (Fig. 25). Furthermore, Li's group [245] demonstrated a facile strategy to synthesize a novel three-dimensional (3D) graphene aerogel-supported and graphene quantum dots-modified γ-MnOOH nanotubes electrocatalyst. The GQDs structural defects can facilitate the adsorption of oxygen and charge transfer. GQDs play a role as the highly efficient surface "sensitizer".

In the majority of the above-mentioned studies on various carbon-based materials for metal–air batteries, the electrocatalytic ORR processes follow four-electron pathway. Many of these catalysts show similar onset potential and better or similar electrochemical performance compared to commercial Pt/C catalysts. These results indicate that such nanocarbon-based catalysts may be promising for future applications and have the potential to replace their expensive Pt counterparts.

4. Electrolytes

Selecting a proper electrolyte system is another key to achieving better performance in metal–air batteries. The various metal–air batteries have different requirements for electrolyte properties. Recently, Qu et al. [246] and Majlan et al. [23] have given two good general reviews on the electrolytes of metal–air batteries. They have summarized the aqueous electrolytes, and non-aqueous electrolytes including aprotic electrolytes, solid-state electrolytes, and room temperature ionic liquids (RTILs) in detail. Thus, the repetitious details will not be discussed in this section. We will focus on the specific issues in Al–air batteries, mostly related to the reactions between electrodes and electrolyte, i.e: the high dissolution of aluminum, the precipitation of insoluble carbonate, hydrogen evolution and the electrolyte evaporation or ambient moisture uptake.

4.1. Aqueous electrolytes

Aqueous electrolytes can be classified according to their pH values as alkaline electrolytes (7 < pH ≤ 13), neutral salt electrolytes (pH = 7), and acidic electrolytes (2 ≤ pH < 7). The low solubility of oxygen in aqueous electrolytes is the primary obstruction of oxygen reduction and the battery performance [247,248]. The most commonly used electrolytes for Al–air batteries are alkaline solutions, such as potassium hydroxide (KOH) and sodium hydroxide (NaOH) solutions, with KOH solutions being preferred owing to its better ionic conductivity, lower viscosity, higher oxygen diffusion
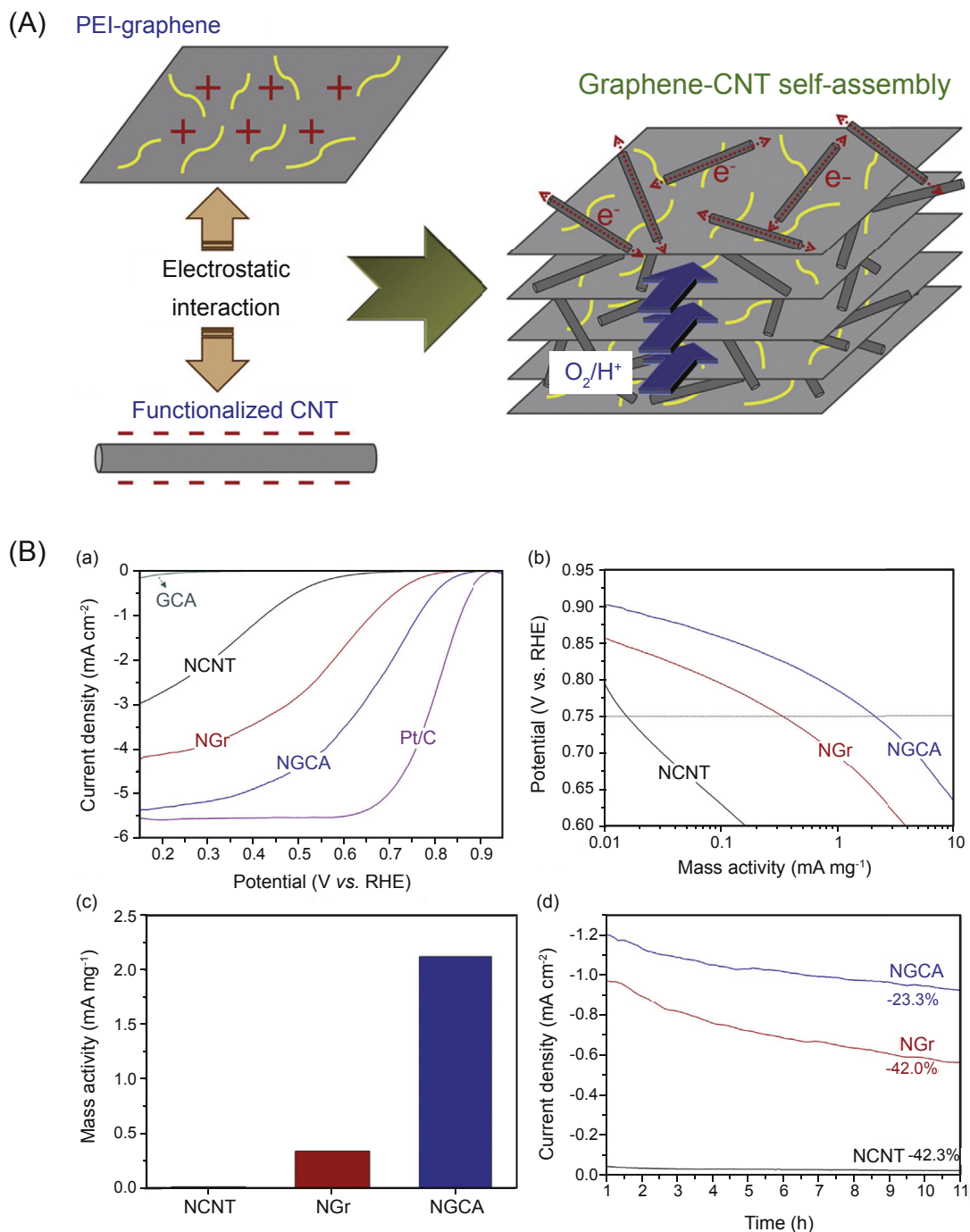
Fig. 22. (A) Strategy for enhancing the applicability of graphene as an electrode material. (B) (a) LSV curves in O_2-saturated 1 M $HClO_4$ solutions with 2000 rpm of electrode rotation speed, (b) Tafel plots based on unit mass of the carbons, (c) mass activities (mA mg^{-1}) calculated at 0.75 V (*vs*. RHE), and (d) current-time chronoamperometric responses obtained at 0.6 V (*vs*. RHE) for 10 h [234].

coefficients and faster reaction kinetics [277]. The major shortcoming of alkaline aqueous electrolytes is the precipitation of their respective carbonates.

Since the early 1970s, the effectiveness of neutral salt solution electrolytes for Al−air batteries has been intensively studied. Many researchers have proven that the potential values for pure Al electrodes are in the range of 0.65 V−1.1 V when it is put in sodium chloride (NaCl) solutions [25,43,249]. It is demonstrated that the redox potential values of Al

electrodes are dependent on the concentration of NaCl solutions and operating temperatures [43,249]. Binary and ternary alloys of Al are also advantageous for improving the performance of Al−air batteries with neutral salt electrolytes [250−254]. The studies on neutral salt electrolytes have been summarized by Qu's group in the recent review [246].

The acidic electrolytes, such as sulfuric acid and hydrochloride acid have been proposed for some types of metal−air batteries, with the primary purpose of suppressing anodic
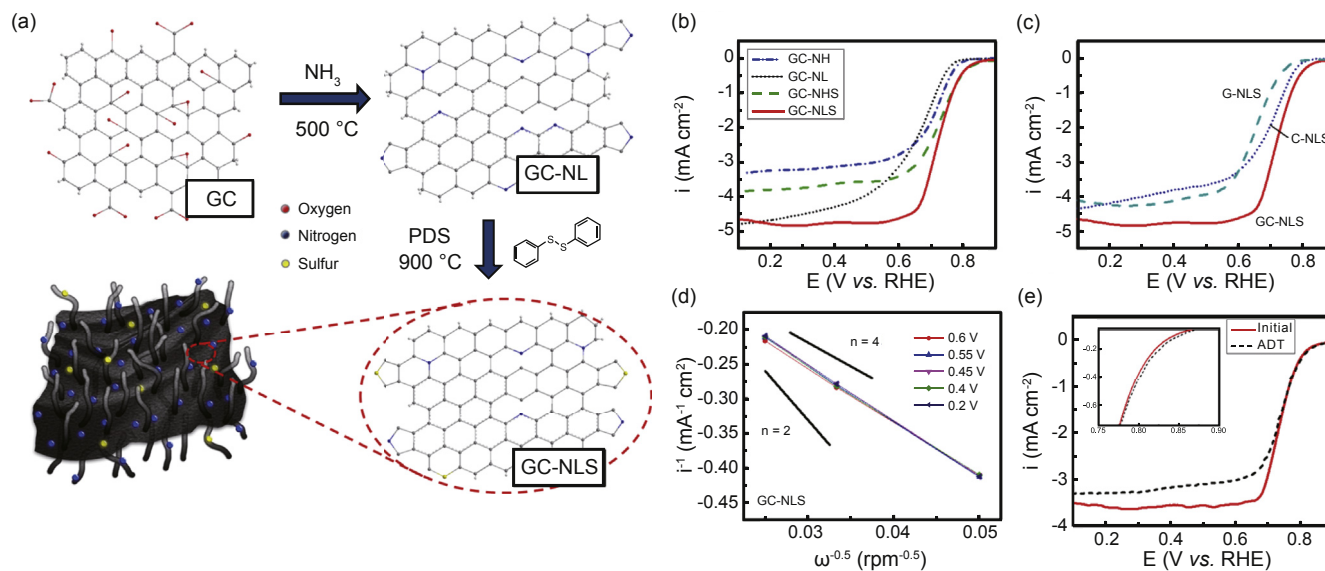
Fig. 23. (a) Schematic of the sequential doping process for preparing GC-NLS nanocomposites. (b) ORR activity of GC-NH, GC-NL, GC-NHS, and GC-NLS in a 0.1 M KOH electrolyte with a 1600 rpm electrode rotation and 10 mV s^{-1} scan rate. (c) Evidence of the beneficial synergistic effect of GC-NLS in comparison to G-NLS and C-NLS. (d) Koutecky−Levich plots for GCNLS at different electrode potentials. Calculated lines for n = 2 and n = 4 are shown for comparison. (e) ORR activity (900 rpm) before and after ADT consisting of 5000 cycles between 0.6 and 1.0 V *vs*. RHE under nitrogen saturation [235].

dendrite formation and carbonate formation in the cathode [275,276]. However, the Al anode is not stable in most acidic electrolytes, leading to considerable corrosion problems. Therefore, it is undesirable to apply acidic electrolytes in Al−air batteries.

4.2. Non-aqueous electrolytes

The non-aqueous electrolytes for Al−air batteries have gained increasing attention due to the partial solutions of the critical problems that exist in aqueous systems such as: electrode corrosion, dendrite formation, electrolyte drying and air electrode leakage. They can be classified into two main categories: ionic liquid electrolytes (ILs), and polymer electrolytes (PEs), and are extensively discussed in some recent reviews [23,246,255]. The focus of this section is on the highly studied PEs-based Al−air battery systems. The primary advantages of polymer conductor electrolyte systems in Al−air batteries are the ability to avoid leakage, enhanced electrochemical stability at high voltage and improved thermal stability. Reference [23] presents a summary of the polymer and solid-state electrolytes used in Al−air battery applications. Notably, applying an alkaline gel-polymer electrolyte (GPE) has opened up new research opportunities in Al−air batteries. Corbo et al. [256] used alkaline hydrogels prepared by xanthan and κ-carrageenan as electrolytes in Al−air primary batteries. Electrochemical measurements of the hydrogels exhibit appreciable Al-ion conductivities, following the order of performance as xanthan with 1 M KOH liquid electrolyte < xanthan + 8 M KOH GPE < κ-carrageenan + 8 M KOH GPE. In addition, Peng and co-workers [257] reported a new family of all-solid-state fiber-shaped Al−air batteries with a specific capacity of 35 mAh g^{-1} and an

energy density of 11768 Wh kg^{-1} (Fig. 26). The modified hydrogel electrolyte decreases the corrosion of the Al spring and increases stability and safety, with the added benefit of flex and stretchability. Zuo et al. [258] used the polyacrylic acid (PAA)-based alkaline GPE instead of aqueous electrolytes to prevent leakage in Al−air batteries. However, few studies have been performed regarding the use of polymer electrolytes in Al−air batteries, and there is a clear need for further research in this area.

4.3. Corrosion inhibitors

The application of Al and Al alloy anodes in Al−air batteries requires the electrodes to have minimal passivation so that dissolution can occur with ease. However, this depassivation leads to the spontaneous degradation of aluminum. In addition, the self-corrosion reaction of aluminum with release of hydrogen causes fuel loss in alkaline media. Thus, adding inhibitors to the electrolytes becomes one of the most effective methods to relieve these problems. The primary inhibition mechanism of corrosion inhibitors is utilizing the adsorption of inhibitor molecules on the aluminum surface to effectively lower the corrosion reaction. Many investigators have studied inhibitors for the corrosion of Al and Al alloys in different mediums in recent years [259−264].

Very recently, Eagan et al. [255] and Mokhtar et al. [23] gave extensive reviews on inhibitors of Al−air batteries. To avoid overlapping the above reviews, section 4.3 will focus on reviewing the recent progresses on inhibitors briefly. The most studied ion additives in neutral salt condition are In^{3+}, Sn^{3+} and Zn^{2+} ions [42,265−267]. In alkaline condition, zinc oxide (ZnO) and sodium stannate (Na$_2$SnO$_3$) are the widely used chemical inhibitors [268−271]. It is demonstrated that ZnO is
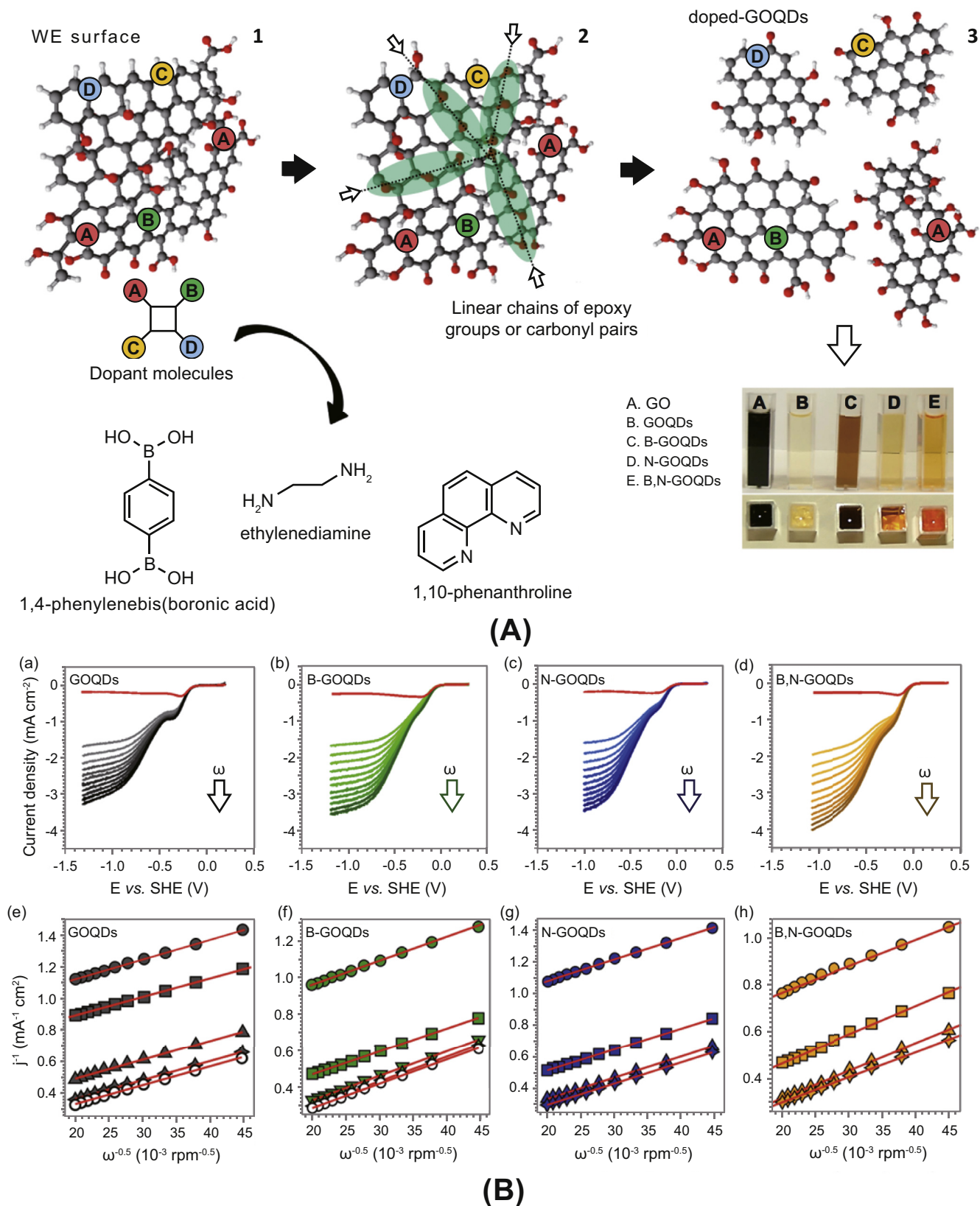
Fig. 24. (A) Pictorial model of the doping mechanism occurring during the synthesis of doped GOQDs, reporting the molecular structures of the dopant molecules used in this work (1,4-phenylenebis(boronic acid), ethylenediamine, and 1,10-phenanthroline). (B) RDE linear sweeps for pure GOQDs (a) and B- (b), N- (c), and B,N-GOQDs (d) acquired in O_2-saturated 0.1 M KOH solution, for different WE rotation rates ranging from 500 to 2500 rpm (the red lines are the polarization curves acquired without rotation) and (e−h) corresponding Koutecky−Levich plots for pure GOQDs (e) and B- (f), N- (g), and B,N-GOQDs (h), for different potentials derived from the RDE measurements (dots, −0.303 V; squares, −0.503 V; triangles, −0.703 V; stars, −0.903 V; circles, −1.103 V) [240].
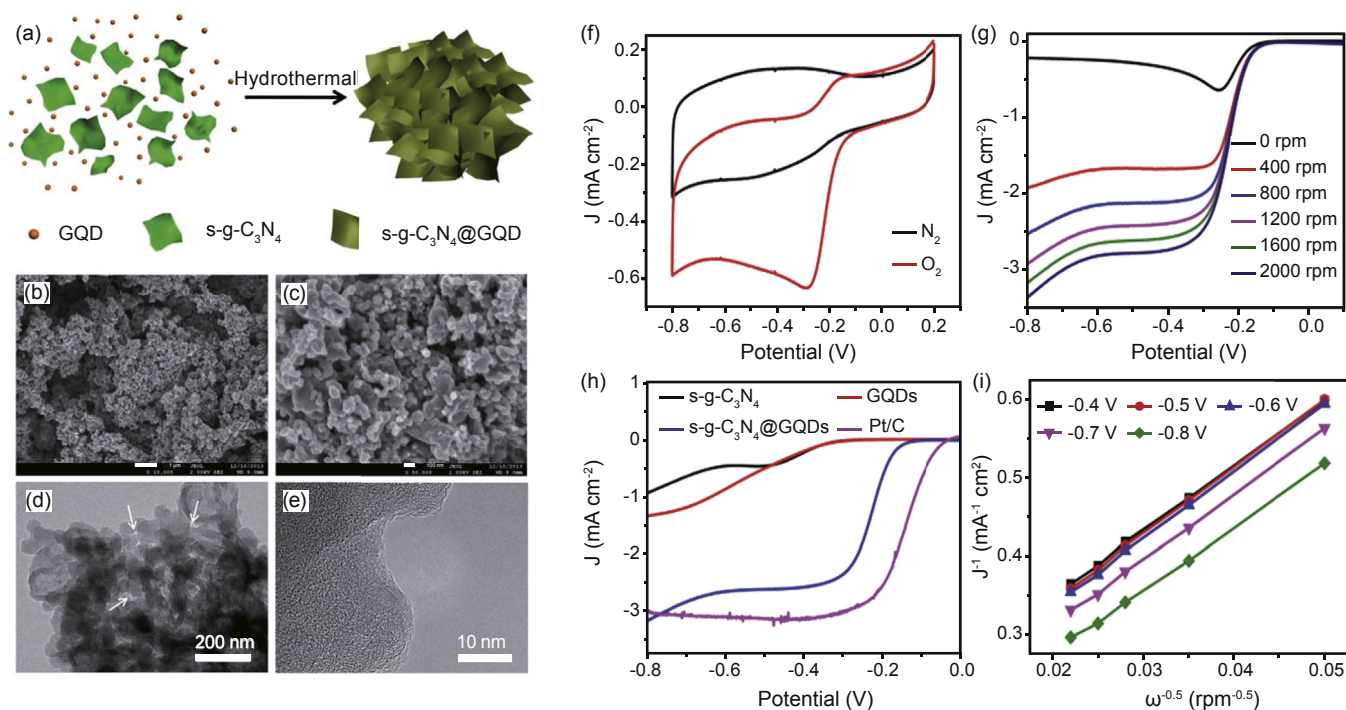
Fig. 25. (a) The fabrication process of s-g-C$_3$N$_4$@GQDs. (b and c) The SEM images of s-g-C$_3$N$_4$@GQDs. (d) The TEM image of as-prepared s-g-C$_3$N$_4$@GQDs, and (e) the corresponding high resolution TEM image of (d). Scale bars: (b) 1 mm, (c) 100 nm, (d) 200 nm, and (e) 10 nm. (f) CV curves of s-g-C$_3$N$_4$@GQDs in an O$_2$- or N$_2$-saturated 0.1 M KOH solution at a scan rate of 10 mV s^{-1}. (g) The linear sweep voltammogram (LSV) curves of the s-g-C$_3$N$_4$@GQDs in O$_2$-saturated 0.1 M KOH solution at different rotating speeds. The scan rate is 10 mV s^{-1} (h) LSV of various electrodes on a RDE (1600 rpm) in O$_2$-saturated 0.1 M KOH solution at a scan rate of 10 mV s^{-1}. (i) K−L plots derived from LSV curves at different potentials from 0.4 V to 0.8 V [244].

advantageous to prevent Al corrosion and enhance the performance of Al anode, and Na$_2$SnO$_3$ can shift the potential values more strongly negative. However, some of the other reported inorganic additives, such as chromates, vanadates, borates and hexafluoride silicates, did not show significant inhibitor effect [21]. In addition, organic additives have been also developed in recent years [255,272,273]. Xhanari et al. [263] have made a summary on the organic corrosion inhibitors for Al and its alloys in chloride and alkaline solution. Various aromatic carboxylic acids were demonstrated by different authors as effective inhibitors of aluminum corrosion in alkaline solution, some of them achieving efficiencies greater than 90%. The inhibitory effects were attributed to the surface adsorption via C ¼ O and C ¼ S groups, which can be observed with other metals in acidic conditions [268]. Mahmoud et al. [269] studied the effect of imidazole derivatives on the inhibition of aluminum corrosion in 0.5 M HCl. The results show all imidazole derivatives have high inhibition efficiency because they can absorb on the aluminum surface through the nitrogen atoms as well as electrons in the imidazole ring. The corrosion inhibition of poly ethylene glycol (PEG) toward the aluminum surface in 1.0 M HCl has also been investigated [270]. The study indicates that the PEG acts as a good inhibitor and the inhibition efficiency is attributed to the anodic and cathodic inhibition (mixed type). In addition, Sun and co-workers [262] studied the performance of Al−air batteries in 4 M NaOH containing ZnO or ZnO/cetyl trimethyl ammonium bromide (CTAB) hybrid inhibitors. It was found that CTAB can greatly improve the deposition of Zn so that a uniform and compact Zn layer covers on the aluminum surface. Furthermore, Lin et al. [264] investigated the synergistic effects of carboxymethyl cellulose (CMC) and zinc oxide (ZnO) in alkaline electrolyte for the AA5052 aluminum alloy anode in Al−air battery. The carboxyl groups adsorb on the surface of aluminum make the protective film steady. Overall, various inhibitors have shown strong effect against Al corrosion and can be expected to be used in practical Al−air batteries to prolong their operational lifetime.

5. Conclusions and outlook

The Al−air battery has proven to be very attractive as an efficient and sustainable technology for energy storage and conversion with the capability to power large electronic devices and vehicles. This review has summarized recent developments of Al anode, air cathode, and electrolytes in Al−air batteries.

For the anode, either aluminum alloying with particular elements or the addition of inhibitors to the electrolyte can contribute to reducing the self-corrosion of Al in Al−air battery and enhance the electrochemical oxidation rate. Guidance for a suitable alloying element include: (i) a low melting temperature to form a solid solution alloy with aluminum, (ii) solubility with aluminum, (iii) a higher nobility than
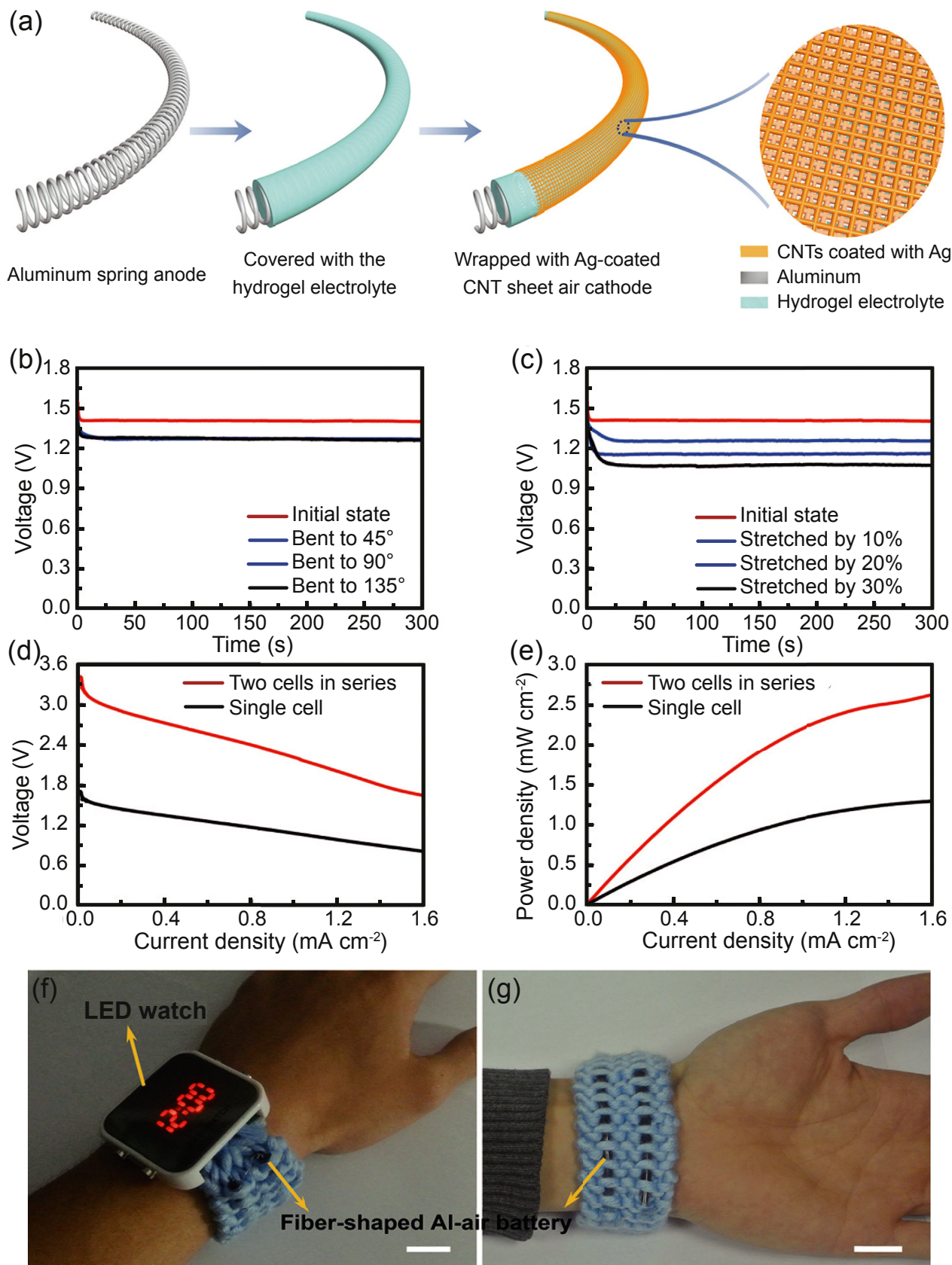
Fig. 26. (a) Fabrication of the fiber-shaped Al−air battery. (b,c) Discharge curves of fiber-shaped Al−air batteries at different bending angles or stretching ratios at a discharge current of 1 mA. (d,e) Polarization and power-density curves of a single fiber shaped Al−air battery and two batteries in tandem (scan rate: 2 mV s^{-1}). (f,g) Photographs of a commercial LED watch powered by two fiber-shaped Al−air batteries woven into a fabric and connected in series [257].

aluminum in the electrochemical series, (iv) solubility in the electrolyte and (v) a high hydrogen overpotential. In addition, a three-dimensional aluminum electrode is favorable towards increasing the active surface area. Various forms of aluminum with high surface area including foams, meshes and honeycombs, which can be also expected to be used in high current density Al−air batteries. On the air cathode side, the ORR processes are the rate-determining steps in the Al−air battery due to the sluggish reaction kinetic in comparison to the reactions at the anode. The main research direction is to explore highly efficient and durable electrocatalytic materials for facilitating ORR. To date, Pt-based catalysts have been regarded as the most efficient and commonly used catalysts for ORR. Considering the high cost of Pt, it is essential to reduce Pt loading in the catalyst layer, for example by alloying Pt with other metal elements. This review refined the parameters of Pt and Pt alloy nanoparticles (such as shape, size, and composition) which can be used to control their microstructure and properties and thereby enhance the catalytic activity for ORR. In particular, the core-shell structured Pt-alloy nanoparticles have been intensively studied. In the preparation of core-shell structured catalysts, Pt (or Pt alloy) is deposited on other MPt or non-Pt metal nanoparticle cores, followed by a dealloying process (or replacement reaction) to form the Pt or Pt-alloy shell. Core-shell structured Pt-alloy nanocatalysts have been proven capable of greatly enhancing not only the ORR activity but also the catalyst durability due to the electronic and strain effects that arise on the nanostructured surface, which can be adjusted by the selection of various materials and different synthesis routes. This review also provided a detailed discussion about the recent development of non-precious metal based catalysts, including transition metal oxides, spinel oxides, perovskite oxides, metal−carbon−nitrogen, and carbon-based materials. In particular, the nanocarbon-based materials show comparable electrocatalytic performances with the commercial Pt/C catalyst. There are some significant approaches to develop non-precious metal catalytic materials: (1) Exploring the effects of physicochemical properties (e.g., valence state, composition, structure, defects, morphology, size, surface area, conductivity, etc.) on the intrinsic catalytic activity; (2) Designing novel electrocatalysts with innovative structures and increasing the density of active sites; (3) Optimizing synthetic strategies and conditions (e.g., precursor, temperature, reaction time, atmosphere, procedures) to achieve better activity and stability. However, several challenges still need to be addressed and overcome in future work: (1) Understanding of the relationship between microstructure, active sites and ORR activity, with theoretical calculations using the DFT method and other modeling techniques being urgently required; (2) There is an urgent need to develop facile and effective approaches for the preparation of controllable structures and morphologies to meet the needs of ORR catalytic activity and stability; (3) All of the preparations of catalysts are laboratory level, therefore, we need simple methods to synthesize large quantities of catalysts for practical applications.

Finally, for the electrolyte, the nonaqueous systems can prevent electrode corrosion, hydrogen evolution, and electrolyte drying compared with aqueous electrolytes. In particular, polymer electrolytes are extremely attractive for application in Al−air batteries due to their flexibility, lightweight, and superior electrochemical and thermal stability. Thus, solid-state Al−air batteries using polymer electrolytes may be one of the future research directions. They can address the problems of stability and volatility of electrolytes, and even suppress the growth of dendrites. But the relative low ionic conductivity of polymer electrolytes at room temperature is also a challenge to be overcome. Furthermore, the addition of corrosion inhibitors to electrolytes can ease the self-corrosion of aluminum anodes thus improve the practical efficiency of Al−air batteries. Choosing effective corrosion inhibitors with suitable concentration is a key investigation direction for the future advancement of Al−air technology.

In addition, some advanced characterization techniques such as synchrotron radiation [278−280], in particular, in-situ approaches [281−283], can be applied to reveal various reaction mechanisms. Further, computational studies [284−286] should be used to analyze and predict failure features and to develop new electrode materials.

Conflict of interest

There is no conflict of interest.

Acknowledgements

References

[1] B.G. Pollet, I. Staffell, J.L. Shang, Electrochimica Acta 84 (2012) 235−249.
[2] S.F. Tie, C.W. Tan, Renew. Sustain. Energy Rev. 20 (2013) 82−102.
[3] B. Dunn, H. Kamath, J.M. Tarascon, Science 334 (2011) 928−935.
[4] Q. Li, N.J. Bjerrum, J. Power Sources 110 (2002) 1−10.
[5] P.G. Bruce, S.A. Freunberger, L.J. Hardwick, J.M. Tarascon, Nat. Mater. 11 (2011) 19−29.
[6] K.F. Blueton, A.F. Sammells, J. Power Sources 4 (1979) 263−279.
[7] J.-S. Lee, S. Tai Kim, R. Cao, N.-S. Choi, M. Liu, K.T. Lee, J. Cho, Adv. Energy Mater. 1 (2011) 34−50.
[8] A. Kraytsberg, Y. Ein-Eli, Nano Energy 2 (2013) 468−480.
[9] M.A. Rahman, X. Wang, C. Wen, J. Electrochem. Soc. 160 (2013) A1759−A1771.
[10] M. Kar, T.J. Simons, M. Forsyth, D.R. MacFarlane, Phys. Chem. Chem. Phys. 16 (2014) 18658−18674.
[11] Z.L. Wang, D. Xu, J.J. Xu, X.B. Zhang, Chem. Soc. Rev. 43 (2014) 7746−7786.
[12] G. Girishkumar, B. McCloskey, A.C. Luntz, S. Swanson, W. Wilcke, J. Phys. Chem. Lett. 1 (2010) 2193−2203.
[13] J.S. Lee, G.S. Park, H.I. Lee, S.T. Kim, R. Cao, M. Liu, J. Cho, Nano Lett. 11 (2011) 5362−5366.

[14] Armand Michel, J.-M. Tarascon, Nature 451 (2008) 652–657.
[15] A. Kraytsberg, Y. Ein-Eli, J. Power Sources 196 (2011) 886–893.
[16] Y.-C. Lu, H.A. Gasteiger, M.C. Parent, V. Chiloyan, Y. Shao-Horn, Electrochem. Solid-State Lett. 13 (2010) A69–A72.
[17] T. Zhang, N. Imanishi, Y. Shimonishi, A. Hirano, Y. Takeda, O. Yamamoto, N. Sammes, Chem. Commun. 46 (2010) 1661–1663.
[18] W. Xu, K. Xu, V.V. Viswanathan, S.A. Towne, J.S. Hardy, J. Xiao, Z. Nie, D. Hu, D. Wang, J.-G. Zhang, J. Power Sources 196 (2011) 9631–9639.
[19] L.J. Hardwick, P.G. Bruce, Curr. Opin. Solid State Mater. Sci. 16 (2012) 178–185.
[20] R. Hamlen, T. Atwater, D. Linden, T. Reddy, McGraw-Hill, New York, USA, (2002) 38.31–38.53.
[21] S. Yang, H. Knickle, J. Power Sources 112 (2002) 162–173.
[22] R. Mori, RSC Adv. 7 (2017) 6389–6395.
[23] M. Mokhtar, M.Z.M. Talib, E.H. Majlan, S.M. Tasirin, W.M.F.W. Ramli, W.R.W. Daud, J. Sahari, J. Industrial Eng. Chem. 32 (2015) 1–20.
[24] H. Schwarz, Encycl. Energy 1 (2004) 81–95.
[25] M. Nestoridi, D. Pletcher, R.J.K. Wood, S. Wang, R.L. Jones, K.R. Stokes, I. Wilcock, J. Power Sources 178 (2008) 445–455.
[26] N. Tanaka, Int. Energy Agency, Tech. Rep. (2011).
[27] S. Zaromb, J. Electrochem, Soc. 109 (1962) 1125–1130.
[28] L. Bockstie, D. Trevethan, S. Zaromb, J. Electrochem. Soc. 110 (1963) 267–271.
[29] E.I. Shkolnikov, A.Z. Zhuk, M.S. Vlaskin, Renew. Sustain. Energy Rev. 15 (2011) 4611–4623.
[30] X. Zhang, S.H. Yang, H. Knickle, J. Power Sources 128 (2004) 331–342.
[31] J. Zhang, M. Klasky, B.C. Letellier, J. Nucl. Mater. 384 (2009) 175–189.
[32] A.A. Mohamad, Corros. Sci. 50 (2008) 3475–3479.
[33] J. Bernard, M. Chatenet, F. Dalard, Electrochimica Acta 52 (2006) 86–93.
[34] M.L. Doche, J.J. Rameau, R. Durand, F. Cattin, Corros. Sci. 41 (1999) 805–826.
[35] L. Fan, H. Lu, J. Power Sources 284 (2015) 409–415.
[36] M. Pino, D. Herranz, J. Chacón, E. Fatás, P. Ocón, J. Power Sources 326 (2016) 296–302.
[37] Y.-J. Cho, I.-J. Park, H.-J. Lee, J.-G. Kim, J. Power Sources 277 (2015) 370–378.
[38] L. Fan, H. Lu, J. Leng, Z. Sun, C. Chen, J. Power Sources 299 (2015) 66–69.
[39] S.B. Saidman, J.B. Bessone, Electrochimica Acta 42 (1997) 413–420.
[40] A.R. Despić, D.M. Dražić, M.M. Purenović, N. Ciković, J. Appl. Electrochem. 6 (1976) 527–542.
[41] H.A. El Shayeb, F.M. Abd El Wahab, S. Zein El Abedin, Corros. Sci. 43 (2001) 655–669.
[42] H.A.E. Shayeb, F.M.A.E. Wahab, S.Z.E. Abedin, J. Appl. Electrochem. 29 (1999) 473–480.
[43] S.Z.E. Abedin, F. Endres, J. Appl. Electrochem. 34 (2004) 1071–1080.
[44] I. Smoljko, S. Gudić, N. Kuzmanić, M. Kliškić, J. Appl. Electrochem. 42 (2012) 969–977.
[45] S. Gudić, I. Smoljko, M. Kliškić, Mater. Chem. Phys. 121 (2010) 561–566.
[46] W. Wilhelmsen, T. Arnesen, Ø. Hasvold, N.J. Størkersen, Electrochimica Acta 36 (1991) 79–85.
[47] M. Pino, J. Chacón, E. Fatás, P. Ocón, J. Power Sources 299 (2015) 195–201.
[48] Z. Sun, H. Lu, J. Electrochem. Soc. 162 (2015) A1617–A1623.
[49] Z. Sun, H. Lu, L. Fan, Q. Hong, J. Leng, C. Chen, J. Electrochem. Soc. 162 (2015) A2116–A2122.
[50] M. Jingling, W. Jiuba, Z. Hongxi, L. Quanan, J. Power Sources 293 (2015) 592–598.
[51] S. Khireche, D. Boughrara, A. Kadri, L. Hamadou, N. Benbrahim, Corros. Sci. 87 (2014) 504–516.
[52] J. Ma, J. Wen, F. Ren, G. Wang, Y. Xiong, J. Electrochem. Soc. 163 (2016) A1759–A1764.
[53] K. Harting, U. Kunz, T. Turek, Z. für Phys. Chem. 226 (2012) 151–166.
[54] K. Liu, Z. Peng, H. Wang, Y. Ren, D. Liu, J. Li, Y. Tang, N. Zhang, J. Electrochem. Soc. 164 (2017) F475–F483.
[55] X. Wang, P.J. Sebastian, M.A. Smit, H. Yang, S.A. Gamboa, J. Power Sources 124 (2003) 278–284.
[56] T. Takeguchi, T. Yamanaka, H. Takahashi, H. Watanabe, T. Kuroki, H. Nakanishi, Y. Orikasa, Y. Uchimoto, H. Takano, N. Ohguri, M. Matsuda, T. Murota, K. Uosaki, W. Ueda, J. Am. Chem. Soc. 135 (2013) 11125–11130.
[57] I. Roche, E. Chaînet, M. Chatenet, J. Vondrak, J. Phys. Chem. C 111 (2007) 1434–1443.
[58] B. Cui, H. Lin, J.-B. Li, X. Li, J. Yang, J. Tao, Adv. Funct. Mater. 18 (2008) 1440–1447.
[59] N.-L. Wu, W.-R. Liu, S.-J. Su, Electrochimica Acta 48 (2003) 1567–1571.
[60] G.W. Heise, in, Google Patents, 1933.
[61] F. Bidault, D.J.L. Brett, P.H. Middleton, N.P. Brandon, J. Power Sources 187 (2009) 39–48.
[62] F. Li, Z. Chen, Graphene Chem. Theor. Perspect. (2013) 347–369.
[63] G. Wu, P. Zelenay, Acc. Chem. Res. 46 (2013) 1878–1889.
[64] F. Cheng, J. Chen, Chem. Soc. Rev. 41 (2012) 2172–2192.
[65] K. Kinoshita, Electrochemical Oxygen Technology, John Wiley & Sons, 1992.
[66] J.S. Spendelow, A. Wieckowski, Phys. Chem. Chem. Phys. 9 (2007) 2654–2675.
[67] P.A. Christensen, A. Hamnett, D. Linares-Moya, Phys. Chem. Chem. Phys. 13 (2011) 5206–5214.
[68] W. Vielstich, H. Yokokawa, H.A. Gasteiger, Handbook of Fuel Cells: Fundamentals Technology and Applications, John Wiley & Sons, 2009.
[69] L. Jörissen, J. Power Sources 155 (2006) 23–32.
[70] Y. Feng, N. Alonso-Vante, Phys. Status Solidi (b) 245 (2008) 1792–1806.
[71] B. Wang, J. Power Sources 152 (2005) 1–15.
[72] L. Zhang, J. Zhang, D.P. Wilkinson, H. Wang, J. Power Sources 156 (2006) 171–182.
[73] N. Leonard, V. Nallathambi, S.C. Barton, J. Electrochem. Soc. 160 (2013) F788–F792.
[74] H. Hu, J.H. Xin, H. Hu, X. Wang, Y. Kong, Appl. Catal. A Gen. 492 (2015) 1–9.
[75] X. Ge, A. Sumboja, D. Wuu, T. An, B. Li, F.W.T. Goh, T.S.A. Hor, Y. Zong, Z. Liu, ACS Catal. 5 (2015) 4643–4667.
[76] J.X. Wang, H. Inada, L. Wu, Y. Zhu, Y. Choi, P. Liu, W.P. Zhou, R. Adzic, J. Am. Chem. Soc. 131 (2009) 17298–17302.
[77] M. Shao, Q. Chang, J.P. Dodelet, R. Chenitz, Chem. Rev. 116 (2016) 3594–3657.
[78] N.M. Markovic, H.A. Gasteiger, P.N. Ross, J. Phys. Chem. 99 (1995) 3411–3415.
[79] N.M. Marković, H.A. Gasteiger, P.N. Ross, J. Phys. Chem. 100 (1996) 6715–6721.
[80] N. Tian, Z.Y. Zhou, S.G. Sun, Y. Ding, Z.L. Wang, Science 316 (2007) 732–735.
[81] X. Zhong, Y. Feng, I. Lieberwirth, W. Knoll, Chem. Mater 18 (2006) 2468–2471.
[82] Z.Y. Zhou, N. Tian, Z.Z. Huang, D.J. Chen, S.G. Sun, Faraday Discuss. 140 (2009) 81–92.
[83] C. Wang, H. Daimon, T. Onodera, T. Koda, S. Sun, Angew. Chem. Int. Ed. Engl. 47 (2008) 3588–3591.
[84] Y.J. Wang, N. Zhao, B. Fang, H. Li, X.T. Bi, H. Wang, Chem. Rev. 115 (2015) 3433–3467.
[85] V.R. Stamenkovic, B.S. Mun, M. Arenz, K.J. Mayrhofer, C.A. Lucas, G. Wang, P.N. Ross, N.M. Markovic, Nat. Mater. 6 (2007) 241–247.
[86] Y. Xia, Y. Xiong, B. Lim, S.E. Skrabalak, Angew. Chem. Int. Ed. Engl. 48 (2009) 60–103.
[87] J. Wu, A. Gross, H. Yang, Nano Lett. 11 (2011) 798–802.
[88] J. Wu, L. Qi, H. You, A. Gross, J. Li, H. Yang, J. Am. Chem. Soc. 134 (2012) 11880–11883.
[89] J. Greeley, I.E. Stephens, A.S. Bondarenko, T.P. Johansson, H.A. Hansen, T.F. Jaramillo, J. Rossmeisl, I. Chorkendorff, J.K. Norskov, Nat. Chem. 1 (2009) 552–556.

[90] V. Mazumder, M. Chi, K.L. More, S. Sun, J. Am, Chem. Soc. 132 (2010) 7848−7849.

[91] S.J. Hwang, S.J. Yoo, J. Shin, Y.H. Cho, J.H. Jang, E. Cho, Y.E. Sung, S.W. Nam, T.H. Lim, S.C. Lee, S.K. Kim, Sci. Rep. 3 (2013) 1309.

[92] K.A. Kuttiyiel, K. Sasaki, Y. Choi, D. Su, P. Liu, R.R. Adzic, Nano Lett. 12 (2012) 6266−6271.

[93] J. Zhao, W. Chen, Y. Zheng, X. Li, J. Power Sources 162 (2006) 168−172.

[94] S.J. Bae, S.J. Yoo, Y. Lim, S. Kim, Y. Lim, J. Choi, K.S. Nahm, S.J. Hwang, T.-H. Lim, S.-K. Kim, P. Kim, J. Mater. Chem. 22 (2012) 8820−8825.

[95] Y. Zhang, C. Ma, Y. Zhu, R. Si, Y. Cai, J.X. Wang, R.R. Adzic, Catal. Today 202 (2013) 50−54.

[96] S. Ghosh, P. Kar, N. Bhandary, S. Basu, S. Sardar, T. Maiyalagan, D. Majumdar, S.K. Bhattacharya, A. Bhaumik, P. Lemmens, S.K. Pal, Catal. Sci. Technol. 6 (2016) 1417−1429.

[97] Y. Tang, H. Qiao, H. Wang, P. Tao, J. Mater. Chem. A 1 (2013) 12512−12518.

[98] D. Wang, X. Chen, D.G. Evans, W. Yang, Nanoscale 5 (2013) 5312−5315.

[99] W. Yin, Y. Shen, F. Zou, X. Hu, B. Chi, Y. Huang, ACS Appl. Mater. Interfaces 7 (2015) 4947−4954.

[100] Y. Xue, H. Miao, S. Sun, Q. Wang, S. Li, Z. Liu, J. Power Sources 342 (2017) 192−201.

[101] B. Hua, Y.-Q. Zhang, N. Yan, M. Li, Y.-F. Sun, J. Chen, J. Li, J.-L. Luo, Adv. Funct. Mater. 26 (2016) 4106−4112.

[102] O. Crowther, M. Salomon, Membranes 2 (2012) 216−227.

[103] H.R. Byon, J. Suntivich, Y. Shao-Horn, Chem. Mater. 23 (2011) 3421−3428.

[104] J.E. Post, Proc. Natl. Acad. Sci. 96 (1999) 3447−3454.

[105] F.H.B. Lima, M.L. Calegaro, E.A. Ticianelli, Electrochimica Acta 52 (2007) 3732−3738.

[106] F. Cheng, J. Shen, W. Ji, Z. Tao, J. Chen, ACS Appl. Mater. Interfaces 1 (2009) 460−466.

[107] F. Cheng, Y. Su, J. Liang, Z. Tao, J. Chen, Chem. Mater. 22 (2010) 898−905.

[108] A. Morozan, B. Jousselme, S. Palacin, Energy Environ. Sci. 4 (2011) 1238−1254.

[109] L. Mao, Electrochimica Acta 48 (2003) 1015−1021.

[110] M.S. El-Deab, T. Ohsaka, Angew. Chem. Int. Ed. Engl. 45 (2006) 5963−5966.

[111] M.M. Najafpour, T. Ehrenberg, M. Wiechen, P. Kurz, Angew. Chem. Int. Ed. Engl. 49 (2010) 2233−2237.

[112] Y. Umena, K. Kawakami, J.R. Shen, N. Kamiya, Nature 473 (2011) 55−60.

[113] I. Zaharieva, M.M. Najafpour, M. Wiechen, M. Haumann, P. Kurz, H. Dau, Energy Environ. Sci. 4 (2011) 2400−2408.

[114] L. Mao, T. Sotomura, K. Nakatsu, N. Koshiba, D. Zhang, T. Ohsaka, J. Electrochem. Soc. 149 (2002) A504−A507.

[115] L. Jin, L. Xu, C. Morein, C.-h. Chen, M. Lai, S. Dharmarathna, A. Dobley, S.L. Suib, Adv. Funct. Mater. 20 (2010) 3373−3382.

[116] J. Li, N. Wang, Y. Zhao, Y. Ding, L. Guan, Electrochem. Commun. 13 (2011) 698−700.

[117] Y. Cao, Z. Wei, J. He, J. Zang, Q. Zhang, M. Zheng, Q. Dong, Energy Environ. Sci. 5 (2012) 9765−9768.

[118] K. Song, J. Jung, Y.U. Heo, Y.C. Lee, K. Cho, Y.M. Kang, Phys. Chem. Chem. Phys. 15 (2013) 20075−20079.

[119] J. Xiao, L. Wan, X. Wang, Q. Kuang, S. Dong, F. Xiao, S. Wang, J. Mater. Chem. A 2 (2014) 3794−3800.

[120] X. Zhou, X. Shen, Z. Xia, Z. Zhang, J. Li, Y. Ma, Y. Qu, ACS Appl. Mater. Interfaces 7 (2015) 20322−20331.

[121] D.U. Lee, J. Scott, H.W. Park, S. Abureden, J.-Y. Choi, Z. Chen, Electrochem. Commun. 43 (2014) 109−112.

[122] J. Landon, E. Demeter, N. İnoğlu, C. Keturakis, I.E. Wachs, R. Vasić, A.I. Frenkel, J.R. Kitchin, ACS Catal. 2 (2012) 1793−1801.

[123] Y. Ye, L. Kuai, B. Geng, J. Mater. Chem. 22 (2012) 19132−19138.

[124] J. Ciston, R. Si, J.A. Rodriguez, J.C. Hanson, A. Martinez-Arias, M. Fernandez-Garcia, Y. Zhu, J. Phys. Chem. C 115 (2011) 13851−13859.

[125] K. Liu, Y. Song, S. Chen, Nanoscale 7 (2015) 1224−1232.

[126] X. Li, Z. Li, X. Yang, L. Jia, Y.Q. Fu, B. Chi, J. Pu, J. Li, J. Mater. Chem. A 5 (2017) 3320−3329.

[127] J.X. Feng, S.H. Ye, H. Xu, Y.X. Tong, G.R. Li, Adv. Mater 28 (2016) 4698−4703.

[128] Y. Cui, Z. Wen, Y. Liu, Energy Environ. Sci. 4 (2011) 4727−4734.

[129] Y. Li, B. Tan, Y. Wu, Nano Lett. 8 (2008) 265−270.

[130] P. Liu, Q. Hao, X. Xia, L. Lu, W. Lei, X. Wang, J. Phys. Chem. C 119 (2015) 8537−8546.

[131] J. Xiao, Q. Kuang, S. Yang, F. Xiao, S. Wang, L. Guo, Sci. Rep. 3 (2013) 2300.

[132] T. Odedairo, X. Yan, J. Ma, Y. Jiao, X. Yao, A. Du, Z. Zhu, ACS Appl. Mater. Interfaces 7 (2015) 21373−21380.

[133] Z. Zhang, Y. Chen, J. Bao, Z. Xie, J. Wei, Z. Zhou, Part. Part. Syst. Charact. 32 (2015) 680−685.

[134] A. Aijaz, J. Masa, C. Rosler, W. Xia, P. Weide, A.J. Botz, R.A. Fischer, W. Schuhmann, M. Muhler, Angew. Chem. Int. Ed. Engl. 55 (2016) 4087−4091.

[135] F. Cheng, J. Shen, B. Peng, Y. Pan, Z. Tao, J. Chen, Nat. Chem. 3 (2011) 79−84.

[136] P. Trogadas, T.F. Fuller, P. Strasser, Carbon 75 (2014) 5−42.

[137] L. Dai, Y. Xue, L. Qu, H. Choi, J. Baek, Chem. Rev. 115 (2015) 4823−4892.

[138] T.Y. Ma, S. Dai, M. Jaroniec, S.Z. Qiao, J. Am. Chem. Soc. 136 (2014) 13925−13931.

[139] G. Zhang, C. Li, J. Liu, L. Zhou, R. Liu, X. Han, H. Huang, H. Hu, Y. Liu, Z. Kang, J. Mater. Chem. A 2 (2014) 8184−8189.

[140] Q. Wang, H. Yuan, H. Feng, J. Li, C. Zhao, J. Liu, D. Qian, J. Jiang, Y. Liu, RSC Adv. 4 (2014) 18286−18293.

[141] S.G. Mohamed, Y.Q. Tsai, C.J. Chen, Y.T. Tsai, T.F. Hung, W.S. Chang, R.S. Liu, ACS Appl. Mater. Interfaces 7 (2015) 12038−12046.

[142] X. Ge, Y. Liu, F.W. Goh, T.S. Hor, Y. Zong, P. Xiao, Z. Zhang, S.H. Lim, B. Li, X. Wang, Z. Liu, ACS Appl. Mater. Interfaces 6 (2014) 12684−12691.

[143] D.U. Lee, B.J. Kim, Z. Chen, J. Mater. Chem. A 1 (2013) 4754−4762.

[144] H. Zhang, H. Li, H. Wang, K. He, S. Wang, Y. Tang, J. Chen, J. Power Sources 280 (2015) 640−648.

[145] G. Zhang, B.Y. Xia, X. Wang, X.W. David Lou, Adv. Mater 26 (2014) 2408−2412.

[146] R. Ning, J. Tian, A.M. Asiri, A.H. Qusti, A.O. Al-Youbi, X. Sun, Langmuir ACS J. Surfaces Colloids 29 (2013) 13146−13151.

[147] W. Bian, Z. Yang, P. Strasser, R. Yang, J. Power Sources 250 (2014) 196−203.

[148] A. Kargar, S. Yavuz, T.K. Kim, C.H. Liu, C. Kuru, C.S. Rustomji, S. Jin, P.R. Bandaru, ACS Appl. Mater. Interfaces 7 (2015) 17851−17856.

[149] W.R.P. Barros, Q. Wei, G. Zhang, S. Sun, M.R.V. Lanza, A.C. Tavares, Electrochimica Acta 162 (2015) 263−270.

[150] Y. Su, H. Jiang, Y. Zhu, X. Yang, J. Shen, W. Zou, J. Chen, C. Li, J. Mater. Chem. A 2 (2014) 7281−7287.

[151] A.D. Chowdhury, N. Agnihotri, P. Sen, A. De, Electrochimica Acta 118 (2014) 81−87.

[152] X. Zhai, W. Yang, M. Li, G. Lv, J. Liu, X. Zhang, Carbon 65 (2013) 277−286.

[153] Z. Pu, Q. Liu, C. Tang, A.M. Asiri, A.H. Qusti, A.O. Al-Youbi, X. Sun, J. Power Sources 257 (2014) 170−173.

[154] Y. Liu, Y. Wang, X. Xu, P. Sun, T. Chen, RSC Adv. 4 (2014) 4727−4731.

[155] C.-H. Wang, C.-W. Yang, Y.-C. Lin, S.-T. Chang, S.L.Y. Chang, J. Power Sources 277 (2015) 147−154.

[156] Z.-Y. Wu, P. Chen, Q.-S. Wu, L.-F. Yang, Z. Pan, Q. Wang, Nano Energy 8 (2014) 118−125.

[157] J. Xiao, C. Chen, J. Xi, Y. Xu, F. Xiao, S. Wang, S. Yang, Nanoscale 7 (2015) 7056−7064.

[158] S. Bag, K. Roy, C.S. Gopinath, C.R. Raj, ACS Appl. Mater. Interfaces 6 (2014) 2692–2699.

[159] S. Gao, K. Geng, Nano Energy 6 (2014) 44–50.

[160] R. Chen, J. Yan, Y. Liu, J. Li, J. Phys. Chem. C 119 (2015) 8032–8037.

[161] Z.S. Wu, S. Yang, Y. Sun, K. Parvez, X. Feng, K. Mullen, J. Am. Chem. Soc. 134 (2012) 9082–9085.

[162] W. Huang, H. Zhong, D. Li, P. Tang, Y. Feng, Electrochimica Acta 173 (2015) 575–580.

[163] J. Chen, N. Zhou, H. Wang, Z. Peng, H. Li, Y. Tang, K. Liu, Chem. Commun. 51 (2015) 10123–10126.

[164] Y. Liang, H. Wang, J. Zhou, Y. Li, J. Wang, T. Regier, H. Dai, J. Am. Chem. Soc. 134 (2012) 3517–3523.

[165] T.Y. Ma, Y. Zheng, S. Dai, M. Jaroniec, S.Z. Qiao, J. Mater, Chem. A 2 (2014) 8676–8682.

[166] Y. Liu, J. Li, W. Li, Y. Li, Q. Chen, F. Zhan, J. Power Sources 299 (2015) 492–500.

[167] Y. Matsumoto, H. Yoneyama, H. Tamura, Bull. Chem. Soc. Jpn. 51 (1978) 1927–1930.

[168] J. Suntivich, H.A. Gasteiger, N. Yabuuchi, H. Nakanishi, J.B. Goodenough, Y. Shao-Horn, Nat. Chem. 3 (2011) 546–550.

[169] J. Sunarso, A.A.J. Torriero, W. Zhou, P.C. Howlett, M. Forsyth, J. Phys. Chem. C 116 (2012) 5827–5834.

[170] M. Yuasa, M. Nishida, T. Kida, N. Yamazoe, K. Shimanoe, J. Electrochem. Soc. 158 (2011) A605–A610.

[171] Y. Zhu, W. Zhou, Z. Shao, Small 13 (2017) 1603793–1603818.

[172] G. Wu, C.M. Johnston, N.H. Mack, K. Artyushkova, M. Ferrandon, M. Nelson, J.S. Lezama-Pacheco, S.D. Conradson, K.L. More, D.J. Myers, P. Zelenay, J. Mater. Chem. 21 (2011) 11392–11405.

[173] M.-Q. Wang, W.-H. Yang, H.-H. Wang, C. Chen, Z.-Y. Zhou, S.-G. Sun, ACS Catalysis 4 (2014) 3928–3936.

[174] L. Lin, Q. Zhu, A.W. Xu, J. Am. Chem. Soc. 136 (2014) 11027–11033.

[175] E.B. Easton, R. Yang, A. Bonakdarpour, J.R. Dahn, Electrochem. Solid-State Lett. 10 (2007) B6–B10.

[176] R. Yang, K. Stevens, J.R. Dahn, J. Electrochem. Soc. 155 (2008) B79–B91.

[177] E.B. Easton, A. Bonakdarpour, R. Yang, D.A. Stevens, J.R. Dahn, J Electrochem. Soc. 155 (2008) B547–B557.

[178] G. Wu, N.H. Mack, W. Gao, S. Ma, R. Zhong, J. Han, J.K. Baldwin, P. Zelenay, Acs Nano 6 (2012) 9764–9776.

[179] P. Matter, L. Zhang, U. Ozkan, J. Catal. 239 (2006) 83–96.

[180] G. Wu, M. Nelson, S. Ma, H. Meng, G. Cui, P.K. Shen, Carbon 49 (2011) 3972–3982.

[181] M. Terrones, A.R. Botello-Méndez, J. Campos-Delgado, F. López-Urías, Y.I. Vega-Cantú, F.J. Rodríguez-Macías, A.L. Elías, E. Muñoz-Sandoval, A.G. Cano-Márquez, J.-C. Charlier, Nano Today 5 (2010) 351–372.

[182] Y. Zhang, J. Ge, L. Wang, D. Wang, F. Ding, X. Tao, W. Chen, Sci. Rep. 3 (2013) 2771.

[183] A. Zitolo, V. Goellner, V. Armel, M.T. Sougrati, T. Mineva, L. Stievano, E. Fonda, F. Jaouen, Nat. Mater. 14 (2015) 937–942.

[184] K. Wan, Z.-p. Yu, X.-h. Li, M.-y. Liu, G. Yang, J.-h. Piao, Z.-x. Liang, ACS Catal. 5 (2015) 4325–4332.

[185] W. Niu, L. Li, X. Liu, N. Wang, J. Liu, W. Zhou, Z. Tang, S. Chen, J. Am. Chem. Soc. 137 (2015) 5555–5562.

[186] J. Huang, N. Zhu, T. Yang, T. Zhang, P. Wu, Z. Dang, Biosens. Bio-electron. 72 (2015) 332–339.

[187] D. Yin, G. Huang, F. Zhang, Y. Qin, Z. Na, Y. Wu, L. Wang, Chemistry 22 (2016) 1467–1474.

[188] Y. Hou, H. Yuan, Z. Wen, S. Cui, X. Guo, Z. He, J. Chen, J. Power Sources 307 (2016) 561–568.

[189] M. Sun, H. Liu, Y. Liu, J. Qu, J. Li, Nanoscale 7 (2015) 1250–1269.

[190] Y. Lv, Y. Fang, Z. Wu, X. Qian, Y. Song, R. Che, A.M. Asiri, Y. Xia, B. Tu, D. Zhao, Small 11 (2015) 1003–1010.

[191] J. Hu, L. Wang, L. Shi, H. Huang, Electrochimica Acta 161 (2015) 115–123.

[192] Y. Hou, Z. Wen, S. Cui, S. Ci, S. Mao, J. Chen, Adv. Funct. Mater. 25 (2015) 872–882.

[193] P. Ganesan, M. Prabu, J. Sanetuntikul, S. Shanmugam, ACS Catalysis 5 (2015) 3625–3637.

[194] S. Dou, L. Tao, J. Huo, S. Wang, L. Dai, Energy Environ. Sci. 9 (2016) 1320–1326.

[195] G. Gnana kumar, M. Christy, H. Jang, K.S. Nahm, J. Power Sources 288 (2015) 451–460.

[196] P.M. Ajayan, O. Stephan, C. Colliex, D. Trauth, Science-AAAS-Weekly Pap. Ed. 265 (1994) 1212–1214.

[197] M. Moniruzzaman, K.I. Winey, Macromolecules 39 (2006) 5194–5205.

[198] J. Planeix, N. Coustel, B. Coq, V. Brotons, P. Kumbhar, R. Dutartre, P. Geneste, P. Bernier, P. Ajayan, J. Am. Chem. Soc. 116 (1994) 7935–7936.

[199] P. Serp, Appl. Catal. A General 253 (2003) 337–358.

[200] D. Vairavapandian, P. Vichchulada, M.D. Lay, Anal. Chim. Acta 626 (2008) 119–129.

[201] D.Y. Wang, M. Gong, H.L. Chou, C.J. Pan, H.A. Chen, Y. Wu, M.C. Lin, M. Guan, J. Yang, C.W. Chen, Y.L. Wang, B.J. Hwang, C.C. Chen, H. Dai, J. Am. Chem. Soc. 137 (2015) 1587–1592.

[202] X. Lu, H.M. Chan, C.L. Sun, C.M. Tseng, C. Zhao, J. Mater. Chem. A 3 (2015) 13371–13376.

[203] A. Zhao, J. Masa, W. Xia, A. Maljusch, M.G. Willinger, G. Clavel, K. Xie, R. Schlogl, W. Schuhmann, M. Muhler, J. Am. Chem. Soc. 136 (2014) 7551–7554.

[204] R.A. Sidik, A.B. Anderson, N.P. Subramanian, S.P. Kumaraguru, B.N. Popov, J. Phys. Chem. B 110 (2006) 1787–1793.

[205] S. Maldonado, K.J. Stevenson, J. Phys. Chem. B 109 (2005) 4707–4716.

[206] J. Wei, Y. Hu, Y. Liang, B. Kong, J. Zhang, J. Song, Q. Bao, G.P. Simon, S.P. Jiang, H. Wang, Adv. Funct. Mater. 25 (2015) 5768–5777.

[207] Y. Liu, J. Li, W. Li, Y. Li, F. Zhan, H. Tang, Q. Chen, Int. J. Hydrogen Energy 41 (2016) 10354–10365.

[208] X. Zhao, H. Zhao, T. Zhang, X. Yan, Y. Yuan, H. Zhang, H. Zhao, D. Zhang, G. Zhu, X. Yao, J. Mater. Chem. A 2 (2014) 11666–11671.

[209] P. Zhang, F. Sun, Z. Xiang, Z. Shen, J. Yun, D. Cao, Energy Environ. Sci. 7 (2014) 442–450.

[210] B. Zhang, Z. Wen, S. Ci, S. Mao, J. Chen, Z. He, ACS Appl. Mater. Interfaces 6 (2014) 7464–7470.

[211] J. Ma, A. Habrioux, Y. Luo, G.R. Sanchez, L. Calvillo, G. Granozzi, P.B. Balbuena, N.A. Vante, J. Mater. Chem. A 3 (2015) 11891–11904.

[212] K. Gong, F. Du, Z. Xia, M. Durstock, L. Dai, Science 323 (2009) 760–764.

[213] T. Ikeda, M. Boero, S.F. Huang, K. Terakura, M. Oshima, J. Ozaki, J. Phys. Chem. C 112 (2008) 14706–14709.

[214] M. Kaukonen, R. Kujala, E. Kauppinen, J. Phys. Chem. C 116 (2012) 632–636.

[215] J.P. Paraknowitsch, A. Thomas, Energy & Environ. Sci. 6 (2013) 2839–2855.

[216] Y. Gong, H. Fei, X. Zou, W. Zhou, S. Yang, G. Ye, Z. Liu, Z. Peng, J. Lou, R. Vajtai, B.I. Yakobson, J.M. Tour, P.M. Ajayan, Chem. Mater. 27 (2015) 1181–1186.

[217] B. Chen, R. Li, G. Ma, X. Gou, Y. Zhu, Y. Xia, Nanoscale 7 (2015) 20674–20684.

[218] J. Zhang, Z. Zhao, Z. Xia, L. Dai, Nat. Nanotechnol. 10 (2015) 444–452.

[219] K. Qu, Y. Zheng, S. Dai, S.Z. Qiao, Nano Energy 19 (2016) 373–381.

[220] L. Wang, Z. Sofer, A. Ambrosi, P. Šimek, M. Pumera, Electrochem. Commun. 46 (2014) 148–151.

[221] Z. Liu, H. Nie, Z. Yang, J. Zhang, Z. Jin, Y. Lu, Z. Xiao, S. Huang, Nanoscale 5 (2013) 3283–3288.

[222] H. Jiang, Y. Zhu, Q. Feng, Y. Su, X. Yang, C. Li, Chemistry–A Eur. J. 20 (2014) 3106–3112.

[223] W. Yang, X. Yue, X. Liu, J. Zhai, J. Jia, Nanoscale 7 (2015) 11956–11961.

[224] Z. Lin, G.H. Waller, Y. Liu, M. Liu, C.-p. Wong, Nano Energy 2 (2013) 241–248.

[225] Y. Xue, D. Yu, L. Dai, R. Wang, D. Li, A. Roy, F. Lu, H. Chen, Y. Liu, J. Qu, Phys. Chem. Chem. Phys. 15 (2013) 12220–12226.

[226] R. Du, N. Zhang, J. Zhu, Y. Wang, C. Xu, Y. Hu, N. Mao, H. Xu, W. Duan, L. Zhuang, L. Qu, Y. Hou, J. Zhang, Small 11 (2015) 3903–3908.

[227] S. Yang, Y. Huang, W. Zhu, B. Deng, H. Wang, Z. Zhang, P. Bao, G. Wang, Int. J. Hydrogen Energ 39 (2014) 15063–15071.

[228] Y. Hou, S. Cui, Z. Wen, X. Guo, X. Feng, J. Chen, Small 11 (2015) 5940−5948.

[229] W. Yan, X. Cao, J. Tian, C. Jin, K. Ke, R. Yang, Carbon 99 (2016) 195−202.

[230] X. Ji, X. Zhang, X. Zhang, J. Nanomater. 2015 (2015) 1−9.

[231] M. Zhou, H.L. Wang, S. Guo, Chem. Soc. Rev. 45 (2016) 1273−1307.

[232] P. Chen, T.Y. Xiao, Y.H. Qian, S.S. Li, S.H. Yu, Adv. Mater. 25 (2013) 3192−3196.

[233] P. Zamani, D.C. Higgins, F.M. Hassan, X. Fu, J.-Y. Choi, M.A. Hoque, G. Jiang, Z. Chen, Nano Energy 26 (2016) 267−275.

[234] C.H. Choi, M.W. Chung, H.C. Kwon, J.H. Chung, S.I. Woo, Appl. Catal. B Environ. 144 (2014) 760−766.

[235] D.C. Higgins, M.A. Hoque, F. Hassan, J.-Y. Choi, B. Kim, Z. Chen, ACS Catalysis 4 (2014) 2734−2740.

[236] D.-W. Wang, D. Su, Energy Environ. Sci. 7 (2014) 576−591.

[237] J. Shen, Y. Zhu, X. Yang, C. Li, Chem. Commun. 48 (2012) 3686−3699.

[238] Y. Li, Y. Zhao, H. Cheng, Y. Hu, G. Shi, L. Dai, L. Qu, J. Am. Chem. Soc. 134 (2012) 15−18.

[239] Y. Liu, P. Wu, ACS Appl. Mater. Interfaces 5 (2013) 3362−3369.

[240] M. Favaro, L. Ferrighi, G. Fazio, L. Colazzo, C. Di Valentin, C. Durante, F. Sedona, A. Gennaro, S. Agnoli, G. Granozzi, ACS Catalysis 5 (2015) 129−144.

[241] Q. Li, S. Zhang, L. Dai, L.S. Li, J. Am. Chem. Soc. 134 (2012) 18932−18935.

[242] Y. Song, S. Chen, ACS Appl. Mater. interfaces 6 (2014) 14050−14060.

[243] X. Zhou, Z. Tian, J. Li, H. Ruan, Y. Ma, Z. Yang, Y. Qu, Nanoscale 6 (2014) 2603−2607.

[244] C. Xu, Q. Han, Y. Zhao, L. Wang, Y. Li, L. Qu, J. Mater. Chem. A 3 (2015) 1841−1846.

[245] Y. Liu, W. Li, J. Li, H. Shen, Y. Li, Y. Guo, RSC Advances 6 (2016) 43116−43126.

[246] M. Xu, D.G. Ivey, Z. Xie, W. Qu, J. Power Sources 283 (2015) 358−371.

[247] J. Read, K. Mutolo, M. Ervin, W. Behl, J. Wolfenstine, A. Driedger, D. Foster, J. Electrochem. Soc. 150 (2003) A1351−A1356.

[248] C.O. Laoire, S. Mukerjee, K.M. Abraham, J. Phys. Chem. C 114 (2010) 9178−9186.

[249] S. Gudić, J. Radošević, I. Smoljko, M. Kliškić, Electrochimica Acta 50 (2005) 5624−5632.

[250] J. Ma, J. Wen, Q. Li, Q. Zhang, Int. J. Hydrogen Energy 38 (2013) 14896−14902.

[251] J. Ma, J. Wen, Q. Li, Q. Zhang, J. Power Sources 226 (2013) 156−161.

[252] B. Han, G. Liang, Rare Met. 25 (2006) 360−363.

[253] M. Nestoridi, D. Pletcher, J.A. Wharton, R.J.K. Wood, J. Power Sources 193 (2009) 895−898.

[254] L. Wang, W. Wang, G. Yang, D. Liu, J. Xuan, H. Wang, M.K.H. Leung, F. Liu, Int. J. Hydrogen Energy 38 (2013) 14801−14809.

[255] D.R. Egan, C. Ponce de León, R.J.K. Wood, R.L. Jones, K.R. Stokes, F.C. Walsh, J. Power Sources 236 (2013) 293−310.

[256] T.M. Di Palma, F. Migliardini, D. Caputo, P. Corbo, Carbohydr. Polym. 157 (2017) 122−127.

[257] Y. Xu, Y. Zhao, J. Ren, Y. Zhang, H. Peng, Angew. Chem. Int. Ed. Engl. 55 (2016) 7979−7982.

[258] Z. Zhang, C. Zuo, Z. Liu, Y. Yu, Y. Zuo, Y. Song, J. Power Sources 251 (2014) 470−475.

[259] A.R. Madram, F. Shokri, M.R. Sovizi, H. Kalhor, Port. Electrochim. Acta 34 (2016) 395−405.

[260] P.S.D. Brito, C.A.C. Sequeira, J. Fuel Cell Sci. Technol. 11 (2013) 011008.

[261] Z. Sun, H. Lu, Q. Hong, L. Fan, C. Chen, J. Leng, ECS Electrochem. Lett. 4 (2015) A133−A136.

[262] M. Abdallah, H.E. Megahed, M.A. Radwan, E. Abdfattah, J. Am. Sci. 8 (2012) 49−55.

[263] K. Xhanari, M. Finšgar, Arabian J. Chem. (2016), http://dx.doi.org/10.1016/j.arabjc.2016.08.009.

[264] J. Liu, D. Wang, D. Zhang, L. Gao, T. Lin, J. Power Sources 335 (2016) 1−11.

[265] Y. Tang, L. Lu, H.W. Roesky, L. Wang, B. Huang, J. Power Sources 138 (2004) 313−318.

[266] R.M. Cigala, C. De Stefano, A. Giacalone, A. Gianguzza, S. Sammartano, J. Chem. Eng. Data 56 (2011) 1108−1115.

[267] Z. Liu, S.Z. El Abedin, F. Endres, Phys. Chem. Chem. Phys. 17 (2015) 15945−15952.

[268] X.Y. Wang, J.M. Wang, Q.L. Wang, H.B. Shao, J.Q. Zhang, Mater. Corros. 62 (2011) 1149−1152.

[269] A.D. Martin, J.H. Zhu, ECS Electrochem. Lett. 1 (2012) A13−A16.

[270] M. Rashvand avei, M. Jafarian, H. Moghanni Bavil Olyaei, F. Gobal, S.M. Hosseini, M.G. Mahjani, Mater. Chem. Phys. 143 (2013) 133−142.

[271] G. Quartarone, M. Battilana, L. Bonaldo, T. Tortato, Corros. Sci. 50 (2008) 3467−3474.

[272] M.N. El-Haddad, A.S. Fouda, J. Mol. Liq. 209 (2015) 480−486.

[273] M.K. Awad, M.S. Metwally, S.A. Soliman, A.A. El-Zomrawy, M.A. Bedair, J. Industrial Eng. Chem. 20 (2014) 796−808.

[274] R. Revel, T. Audichon, S. Gonzalez, J. Power Sources 272 (2014) 415−421.

[275] L. Li, A. Manthiram, Adv. Energy Mater. 6 (2016) 1502054.

[276] S.T. Senthilkumar, S.O. Park, J. Kim, S.M. Hwang, S.K. Kwak, Y. Kim, J. Mater, Chem. A (2017), http://dx.doi.org/10.1039/C7TA03298F.

[277] D.M.F. Santos, C.A.C. Sequeira, J.L. Figueiredo, Quím. Nova 36 (2013) 1176−1193.

[278] Y. Chen, S. Ji, Y. Wang, J. Dong, W. Chen, Z. Li, R. Shen, L. Zheng, Z. Zhuang, D. Wang, Y. Li, Angew. Chem. Int. Ed. Engl. 129 (2017) 7041−7045.

[279] K. Iwase, T. Yoshioka, S. Nakanishi, K. Hashimoto, K. Kamiya, Angew. Chem. Int. Ed. Engl. 54 (2015) 11068−11072.

[280] Z.L. Wang, X.F. Hao, Z. Jiang, X.P. Sun, D. Xu, J. Wang, H.X. Zhong, F.L. Meng, X.B. Zhang, J. Am. Chem. Soc. 137 (2015) 15070−15073.

[281] N. Becknell, Y. Kang, C. Chen, J. Resasco, N. Kornienko, J. Guo, N.M. Markovic, G.A. Somorjai, V.R. Stamenkovic, P. Yang, J. Am. Chem. Soc. 137 (2015) 15817−15824.

[282] Y. Gorlin, B. Lassalle-Kaiser, J.D. Benck, S. Gul, S.M. Webb, V.K. Yachandra, J. Yano, T.F. Jaramillo, J. Am. Chem. Soc. 135 (2013) 8525−8534.

[283] T. Kaito, H. Tanaka, H. Mitsumoto, S. Sugawara, K. Shinohara, H. Ariga, H. Uehara, S. Takakusagi, K. Asakura, J. Phys. Chem. C 120 (2016) 11519−11527.

[284] M.D. Bhatt, G. Lee, J.S. Lee, Energy Fuels 31 (2017) 1874−1881.

[285] M.D. Bhatt, G. Lee, J.S. Lee, Electrochimica Acta 228 (2017) 619−627.

[286] G. Wu, J. Wang, W. Ding, Y. Nie, L. Li, X. Qi, S. Chen, Z. Wei, Angew. Chem. Int. Ed. 55 (2016) 1340−1344.

[287] F. Xie, L. Zhang, D. Su, M. Jaroniec, S.Z. Qiao, Adv. Mater. 29 (2017), 1700989.

[288] L. Xia, S. Wang, G. Liu, L. Ding, D. Li, H. Wang, S. Qiao, Small 12 (2016) 853−859.

[289] J. Li, Z. Zhou, K. Liu, F. Li, Z. Peng, Y. Tang, H. Wang, J. Power Sources 343 (2017) 30−38.

[290] K. Liu, Z. Zhou, H. Wang, X. Huang, J. Xu, Y. Tang, J. Li, H. Chu, J. Chen, RSC Adv. 6 (2016) 55552−55559.

[291] X. Tong, S. Chen, C. Guo, X. Xia, X.Y. Guo, ACS Appl. Mater. Interfaces 8 (2016) 28274−28282.

[292] X. Zhao, Y. Fu, J. Wang, Y. Xu, J.-H. Tian, R. Yang, Electrochimica Acta 201 (2016) 172−178.

[293] X. He, F. Yin, S. Yuan, N. Liu, X. Huang, ChemElectroChem 3 (2016) 1107−1115.

[294] W. Wang, J. Geng, L. Kuai, M. Li, B. Geng, Chemistry 22 (2016) 9909−9913.

[295] S. Cao, N. Han, J. Han, Y. Hu, L. Fan, C. Zhou, R. Guo, ACS Appl. Mater. Interfaces 8 (2016) 6040−6050.